NUMERICAL AND EXPERIMENTAL INVESTIGATION OF SWIRL-STABILIZED FLAMES USING NATURAL GAS-HYDROGEN-AIR MIXTURES

A THESIS SUBMITTED TO
THE GRADUATE SCHOOL OF NATURAL AND APPLIED SCIENCES
OF
MIDDLE EAST TECHNICAL UNIVERSITY

BY

EMRE BÖNCÜ

IN PARTIAL FULFILLMENT OF THE REQUIREMENTS
FOR
THE DEGREE OF MASTER OF SCIENCE
IN
MECHANICAL ENGINEERING

AUGUST 2023

Approval of the thesis:

NUMERICAL AND EXPERIMENTAL INVESTIGATION OF SWIRL-STABILIZED FLAMES USING NATURAL GAS-HYDROGEN-AIR MIXTURES

submitted by **EMRE BÖNCÜ** in partial fulfillment of the requirements for the degree of **Master of Science** i**n Mechanical Engineering, Middle East Technical University** by,

Prof. Dr. Halil Kalıpçılar
Dean, Graduate School of **Natural and Applied Sciences** _____

Prof. Dr. M.A. Sahir Arıkan
Head of the Department, **Mechanical Engineering** _____

Prof. Dr. Ahmet Yozgatlıgil
Supervisor, **Mechanical Engineering, METU** _____

Prof. Dr. İskender Gökalp
Co-Supervisor, **TÜBİTAK Marmara Research Center** _____

Examining Committee Members:

Assoc. Prof. Dr. Feyza Kazanç Özerinç
Mechanical Eng., METU _____

Prof. Dr. Ahmet Yozgatlıgil
Mechanical Eng., METU _____

Assoc. Prof. Dr. Hüsnü Dal
Mechanical Eng., METU _____

Asst. Prof. Dr. Özgür Uğraş Baran
Mechanical Eng., METU _____

Prof. Dr. Metin Muradoğlu
Mechanical Eng., Koç University _____

Date: 08.08.2023

I hereby declare that all information in this document has been obtained and presented in accordance with academic rules and ethical conduct. I also declare that, as required by these rules and conduct, I have fully cited and referenced all material and results that are not original to this work.

Name Last name : Emre Böncü

Signature :

ABSTRACT

NUMERICAL AND EXPERIMENTAL INVESTIGATION OF SWIRL-STABILIZED FLAMES USING NATURAL GAS-HYDROGEN-AIR MIXTURES

Böncü, Emre
Master of Science, Mechanical Engineering
Supervisor: Prof. Dr. Ahmet Yozgatlıgil
Co-Supervisor: Prof. Dr. İskender Gökalp

August 2023, 122 pages

Across the world, the interest in hydrogen as a sustainable fuel and an energy carrier is on the rise. This is because hydrogen does not emit CO_2 when converted into energy. Since global regulations on carbon and other harmful gas emissions are becoming more and more strict as time goes on, the necessity of combustor designs capable of burning hydrogen is becoming more relevant. Since other harmful emissions like NO_x are subject to regulations as well, hydrogen burner designs that minimize such emissions too are also becoming equally necessary. In this thesis, an investigation was conducted using natural gas and hydrogen mixtures as fuel with a partially premixed swirl-stabilized burner using a combination of experimental and numerical methods. Throughout the study, fuel mixture composition variations were explored. Experiments involved gradually adding hydrogen to the fuel mixture initially consisting solely of natural gas. Chemiluminescence imaging was employed to analyze the impact of hydrogen addition on the global flame structure and stability. The total volumetric fuel flow rate remained constant throughout the experiments. Investigations continued until a certain volumetric hydrogen ratio in the fuel

(H2VOL%) was reached, causing the transition of the flame stabilization mode. The changes in the dimensions of the lifted flame and the stabilization mode were also examined using numerical simulations. Simulations employed StarCCM+ 22.06 software, incorporating the Large Eddy Simulation (LES) turbulence model, Flamelet Generated Manifold (FGM) combustion model, and the Thickened Flame Model (TFM) for turbulence-chemistry interactions. Both experimental and numerical results show that increasing the H2VOL% causes the flame to lower towards the burner and get more compact. Additionally, the stabilization mode change was observed in both experimental and numerical results.

Keywords: Partially premixed turbulent flames, Hydrogen, Swirl-stabilized flames, CFD, Chemiluminescence imaging

ÖZET

DOĞAL GAZ-HİDROJEN-HAVA KARIŞIMLARI KULLANAN GİRDAPLI ALEVLERİN NUMERİK VE DENEYSEL OLARAK İNCELENMESİ

Böncü, Emre
Yüksek Lisans, Makina Mühendisliği
Tez Yöneticisi: Prof. Dr. Ahmet Yozgatlıgil
Ortak Tez Yöneticisi: Prof. Dr. İskender Gökalp

Ağustos 2023, 122 sayfa

Günümüzde tüm dünyada sürdürülebilir bir enerji kaynağı olarak hidrojen kullanımı konusundaki araştırmalar her geçen gün artmaktadır. Bunun sebebi, hidrojenin enerjiye çevrildiğinde CO_2 salmamasıdır. Dünya çapında karbon ve diğer zararlı gaz emisyonları ile ilgili düzenlemeler giderek daha da katılaştığından hidrojen yakabilen yakıcı tasarımına ihtiyaç da önem kazanmaktadır. NO_x gibi zararlı emisyonlar da bu katı düzenlemelere tabi tutulduğundan zararlı emisyonları en düşük seviyeye indiren hidrojen yakıcı tasarımlar aynı şekilde önemlidir. Bu tezde, doğal gaz ve hidrojen karışımları, kısmi ön karışımlı girdaplı yakıcılarda yakıt olarak kullanılmıştır. Oluşan alevler deneysel ve nümerik metotlar kullanılarak araştırılmıştır. Araştırma sırasında farklı oranlarda gaz karışımları incelenmiştir. Deneyler, başlangıçta tamamı doğal gazdan oluşan yakıta gitgide artan oranlarda hidrojen ekleme yöntemiyle gerçekleştirilmiştir. Hidrojen eklemenin alev yapısı ve kararlılığına etkisini incelemek için kemilüminesans görüntüleme yöntemi kullanılmıştır. Deneyler boyunca toplam debi sabit bırakılmıştır. Deneyler sırasında hidrojen oranı, alev kararlılığı kaldırılmış alevden boruya yapışan alev haline gelene dek artırılmıştır. Kaldırılmış alevin boyutları ve kararlılığındaki değişim de nümerik

simülasyonlar kullanılarak incelenmiştir. Simülasyonlarda büyük burgaç benzetimi kullanılmıştır. Hem deneysel hem de sayısal sonuçlar, yakıt içindeki hidrojen hacimsel oranının artmasının, alevin yanıcıya doğru alçalmasına ve küçülmesine neden olduğunu göstermektedir. Ayrıca kararlılık modu değişikliği hem deneysel hem de sayısal sonuçlarda gözlemlenmiştir.

Anahtar Kelimeler: Kısmi ön karışımlı türbülanslı alev, Hidrojen, Girdaplı alev, HAD, Kemilüminesans görüntüleme

To my beloved wife

ACKNOWLEDGMENTS

I express my deepest gratitude to my mentor Prof. Dr. İskender Gökalp, for always being there, for his guidance, helpfulness. I learned so much from him and I am forever thankful that I had the chance to do my master's with him. I look forward to working with him in the future. I also express my gratitude to my thesis supervisor Prof. Dr. Ahmet Yozgatlıgil for his support.

I wish to express my sincere thanks to all the members of my jury for their valuable comments and time.

I thank my fellow researchers Dilay Güleryüz and Berk Kıymaz for their contributions to the swirl burner studies both numerically and experimentally. I thank Dilay Güleryüz for always being available and very helpful with her excellent laboratory skills. I thank Berk Kıymaz for our valuable discussions, his compassion, and his advice on everything from research to life.

I thank Dr. Mehmet Karaca for his valuable insights on all things numerical and for caring about his students' well-being both in and out of school. I thank Christophe Allouis for always being there, for the countless things I learned from him on design and experimental procedures, and for our conversations on life. I thank Dr. Barış Yılmaz for his guidance and valuable input in our research.

I thank TRMOTOR for allowing me to use the high-powered computer system of the company. I thank Dr. Özhan Öksüz for being an excellent director and supporting my academic studies. I thank Erinç Erdoğan for always supporting and teaching me in both my professional and academic studies. I consider myself very lucky to have such a supportive and understanding team leader. I thank my coworkers Doğu Hazar Kenar for his tremendous help in both my professional and academic life, Serkan Berkay Körpe for his most valuable insights on numerical analysis and economics,

Çağdaş Cem Ergin and Emir Furkan Köz for always being helpful. I thank my former coworker Merthan Kılıç for his help in swirler research.

This thesis was made possible by the financial support of two TÜBİTAK BİDEB Uluslararası Lider Araştırmacılar projects (project 118C287, PI Dr. İskender Gökalp and project 118C233, PI Dr. Christophe Allouis). I express my heartfelt thanks to TÜBİTAK for providing the financial support to design, build, and operate the swirl burner experimental facility and for my master's study grant.

I would like to thank TÜBİTAK ULAKBİM, High Performance and Grid Computing Center (TRUBA) since the early numerical calculations were performed using their resources.

I sincerely thank TÜBİTAK-SAGE for hosting me to conduct my experiments using their laboratory, techniques, and expertise: sincere thanks to Semra Gümrük, Ozan Can Kocaman, Dr. Bora Yazıcı, and Dr. Bülent Sümer for their technical availability and their kindness.

I thank Oğuz Kaya and his team from the Pro-sis Mühendislik company and Fatih Coşkun and his team at Yediç Mühendislik for their valuable input in design and manufacturing of experimental burner.

I thank ODTÜ-BAP, its Director Doç. Dr. Hüsnü Dal, Mehtap Dişbudak and Şaban Dişbudak for their administrative help.

I express my sincere thanks to the Department of Mechanical Engineering at METU for both my bachelors and my master's education. I thank Turan Kalender for taking good care of administrative businesses and acquiring the materials we needed for our experiments.

I thank the rest of our laboratory team, Dr. Rasiha Nefise Mutlu, Dr. Esra Eroğlu and Dr. Jayaraman Kandasamy for the friendly work environment and the research we conducted together.

I give my most heartfelt thanks to my mother for always being there for me, supporting me through all my education both financially and emotionally. I thank my brother for always supporting me and for growing up to be someone I admire. I thank my father for his guidance, which led me to study engineering, his support and his never-ending belief in me. I thank Umut Doğa Ünlü and Arda Nazif Anıl for being the best friends one can ask for.

Last but not least, I would like to thank my wife for being my best friend through high school and college, for brightening my life by being a part of it, for supporting me through all of my master's studies and for being so loving and understanding.

TABLE OF CONTENTS

LIST OF TABLES

TABLES

LIST OF FIGURES

FIGURES

LIST OF ABBREVIATIONS

BLF	Boundary Layer Flashback
CHRR	Chemistry Heat Release Rate
CHT	Conjugate Heat Transfer
CIVB	Combustion Induced Vortex Breakdown
CFD	Computational Fluid Dynamics
CRZ	Central Recirculation Zone
EDM	Electro-Discharge Machining
EBU	Eddy-Breakup Model
EGR	Exhaust Gas Recirculation
FGM	Flamelet Generated Manifold
FRC	Finite Rate Chemistry
H2VOL%	Volumetric Hydrogen Percent in the Fuel
HIT	Homogenous and Isotropic Turbulence
HPC	High Powered Computer
ISL	Inner Shear Zone
KHI	Kelvin-Helmholtz Instability
LDV	Laser Doppler Velocimetry
LHV	Lower Heating Value
LIBS	Laser Induced Breakdown Spectroscopy
LIF	Laser Induced Fluorescence
LII	Laser Induced Incandescence
LPP	Lean Premixed Pre-Vaporized
MFR	Mass Flow Rate
MF	Mass Fraction
MS	Mie Scattering
NG	Natural Gas
ORZ	Outer Recirculation Zone

OSL	Outer Shear Layer
PIV	Particle Image Velocimetry
PLIF	Planar Laser Induced Fluorescence
PVC	Precessing Vortex Core
PV	Progress Variable
RANS	Reynolds Averaged Navier-Stokes
RMS	Root Mean Square
RS	Rayleigh Scattering
SLM	Selective Laser Melting
SLPM	Standard Liter Per Minute
TDLAS	Tunable Diode Laser Absorption Spectroscopy
TFM	Thickened Flame Model
TFS	Turbulent Flame Speed
WALE	Wall Adapting Large Eddy

LIST OF SYMBOLS

$\boldsymbol{w}$	Local flame front velocity
$\boldsymbol{v}$	Velocity vector
S_d	Flame propagation speed
$\boldsymbol{n}$	Flame front normal vector
κ	Flame Stretch
A	Flamelet Area
t	Time
Y	Mass fraction
$\emptyset$	Equivalence ratio
$\boldsymbol{x}, x_i, x_j, x_k$	Position vector
R_h	Hub radius
R	Tip radius
α	Straight blade swirler angle
α_0	Helical blade swirler hub angle
φ	Blockage Ratio
S'	Geometric swirl number
r	Radial distance from the hub
$\boldsymbol{u}, u_i, u_j, u_k$	Velocity vector
$\overline{\boldsymbol{u}}$	Mean velocity vector
$\boldsymbol{u}'$	Fluctuating velocity vector
u_{rms}	Root-mean-square velocity
η	Kolmogorov length scale
τ_η	Kolmogorov time scale
v_η	Kolmogorov velocity scale
ν	Kinematic viscosity
ε	Turbulent kinetic energy dissipation rate

D	Diffusivity
g	Critical velocity gradient
d_q	Quenching distance
S_L	Laminar burning velocity
Da	Damköhler number
K	Chemical reaction rate constant
A	Pre-exponential factor
e	Euler's number
R	Universal gas constant
E_A	Activation energy
T	Temperature
Q	Rate of progress of chemical reaction
ν_k'	Stoichiometric coefficient
W	Molar weight
ρ	Density
τ_{ij}	Viscous stress tensor
g_i	Gravity vector
p	Pressure
μ	Dynamic viscosity
δ_{ij}	Kronecker delta
Υ	Progress variable
Z	Mixture Fraction
h	Total enthalpy
$\dot{\omega}$	Production term
Φ	Scalar
c_p	Constant pressure specific heat
λ	Conductivity
Sc_t	Turbulent Schmidt number
Δ	Filter size

E	Efficiency function
F	Flame thickening factor
Ω	Rection zone sensor
N	Number of points in the flame front
δ_L	Laminar flame thickness
β	Progress variable reaction rate reaction zone sensor model constant
ɑ	TFS model constant
c_v	MF variance algebraic model constant
S_t^{Δ}	Flame speed at the turbulent length scale of the grid size
R_{ij}	Unresolved Reynolds stress tensor
μ_{sgs}	SGS viscosity
k	SGS kinetic energy
S_{ij}	Strain tensor
C_I	Yoshizawa's formula constant
C_m	WALE model constant
OP	WALE model operator
V	Numerical cell volume
u	X-velocity
v	Y-velocity
w	Z-velocity

CHAPTER 1

INTRODUCTION

1.1 Background

Even though renewable energy sources are becoming a more significant part of energy production as time progresses, combustion will still be a substantial source of energy for humanity, for the foreseeable future [1]. As the global importance of greenhouse gases and other harmful gas emissions is more understood, efforts are increasing to develop more environmentally friendly and sustainable combustion technologies. In this regard, many areas are open for innovation by designing new burners operated with environmentally friendly fuels and emitting less toxic and greenhouse gases.

One of the most important among these environmentally friendly fuels is hydrogen. Hydrogen is promising for making the combustion process more sustainable and environmentally friendly since hydrogen combustion produces no greenhouse gases. Additionally, hydrogen can be produced through the water electrolysis process, which makes hydrogen suitable for the much-needed necessity of storing excess electricity from renewable energy sources [2].

However, the technology is not yet mature enough to convert industrial or household burners to 100% hydrogen fuel. This makes hydrogen-enriched natural gas a potential candidate for the next generation of fuels (and energy carriers) before the transition to 100% hydrogen becomes possible. Many studies have already been conducted to understand the effect of hydrogen on the combustion characteristics of natural gas, confirming this fuel's potential [3–8].

The addition of hydrogen to natural gas significantly changes the combustion characteristics of the classical natural gas burners. This justifies the development of experimental and numerical investigations to better design burners that work with natural gas-hydrogen mixtures or pure hydrogen fuel. Additionally, many of the industrial burners in service currently use swirl-stabilized burners. These include industrial process burners and gas turbine combustors. With stricter regulations of the NOx emissions of aero engines, lean premixed/pre-vaporized (LPP) burners have also been at the cutting edge of burner design [9]. With this advancement, gaseous swirl-stabilized flames also become relevant for the aero engine combustion domain.

1.2 Motivation

This thesis investigates the combustion characteristics of swirl-stabilized natural gas (NG)-hydrogen-air turbulent flames regarding mainly their global dimensions, and stability characteristics. In this effort, both experimental and numerical methods have been used. A partially premixed burner has been designed and manufactured for this objective. The global objective is to burn hydrogen – NG – air mixtures with maximum safety (zeroing flash back risks) and minimum NOx emissions (zeroing hot spots in the flame). To attain this objective, the burner is designed as a non-premixed one, involving premixing strategies just at the exit of the burner. These strategies involve swirling the co-axial air flow and radial fuel injection in the swirled air. To achieve rapid premixing, the burner was constructed with fuel injection ports lying just upstream of the burner exit, ensuring that a quasi-full premixing is rapidly achieved. The resulting flow and flame configurations are also modelled and numerically computed for different mixture compositions using state-of-the-art models for turbulent flows, mixing and combustion. The thesis contributes to the combustion knowledge and literature by presenting experimental results for the effect of hydrogen in swirl stabilized turbulent flames and by presenting a numerical setup that is able to model the key characteristics of such flames.

1.3 Thesis Structure

The thesis analyzes the characteristics of swirl-stabilized partially premixed NG-hydrogen-air flames using experimental and numerical methods.

- Following this introductory chapter, Chapter 2 presents the literature survey concerning partially premixed swirl-stabilized turbulent flames. The relevant topics include the swirl-stabilized flame phenomenon and the numerical and experimental methods commonly used for this turbulent reacting flow configuration.
- Chapter 3 presents the experimental setup and methodology used in the experimental analysis. It includes the design and operation of the experimental burner and all the complementary parts used in the experiments. The chapter also presents the measuring and post-processing methods, and the gas flow conditions for each case investigated in the experiments.
- Chapter 4 details the numerical setup for simulating the swirl-stabilized partially premixed reacting flows. These details include the turbulence and combustion models, the numerical mesh, and the software used in the simulations. The chapter also includes the description of the post-processing methods used to obtain numerical results.
- Chapter 5 describes the experimental and numerical results for the investigated flow and flame configurations for several fuel mixture cases. The comparison of the numerical and experimental data is also presented here.
- Chapter 6 summarizes and concludes the thesis work and results while also suggesting plans for future work.

CHAPTER 2

LITERATURE REVIEW

2.1 Laminar and Turbulent Flames

A flame is a surface where chemical reactions in the combustion process occur. These reaction surfaces can differ in behavior, structure, and appearance according to their flow field. Specifically, flames are separated into two different types, turbulent and laminar. Laminar flames occur in a laminar flow. Laminar flames are smooth surfaces and present steady flame surface shapes. Laminar flames occur when viscous forces are larger than the inertial forces in the flow and the lack of mixing between layers of the fluid flow characterizes laminar flows.

On the other hand, turbulent flows are characterized by the random motions present in the flow, which cause mixing between the layers of the fluid flow. Turbulent flames are wrinkled by the flow structures called vortices or eddies present inside turbulent flows. This makes their appearance rough or corrugated compared to laminar flames. The surface shape of turbulent flames fluctuates with time, creating a brush where the instantaneous flames (called often flamelets) fluctuate inside. The wrinkled nature of turbulent flames can fit more flame surface within a given volume, causing the increase of the average burning rate and hence the flame propagation speed.

Laminar and turbulent flames can be premixed or non-premixed depending on the way the fuel and the oxidant are mixed. In non-premixed flames, the fuel and oxidant streams only mix by laminar or turbulent diffusion at the flame front. In premixed flames, they are mixed at molecular level before entering the burner or the combustion chamber. In this thesis, we are interested in premixed (or partially

premixed) turbulent flames. So, the following sections of this literature review mainly concern premixed flames.

The flame propagation speed is one of the main attributes of premixed flames. It can be defined for laminar and turbulent flames. For laminar flames, it is defined as the flame propagation velocity of a laminar planar flame into a quiescent fuel-oxidizer mixture. This quantity depends on the reactive mixture nature, equivalence ratio, pressure, and the unburned mixture temperature. A flame propagation speed can also be defined for turbulent flames. The turbulent flame speed of the same mixture is higher than its laminar counterpart since turbulence enhances the burning rate by wrinkling the flame front and enhancing the heat and mass diffusion.

The flame propagation speed, with respect to the flow speed adjacent to the flame, is an essential parameter in characterizing the flame. This corresponds to the local flame front surface velocity $\boldsymbol{w}$. The definition of the local flame velocity is given in Eq. 2.1.

$$\boldsymbol{w} = \boldsymbol{v} + S_d \boldsymbol{n} \tag{2.1}$$

Where $\boldsymbol{v}$ is the flow velocity vector, S_d is either the laminar or turbulent flame propagation speed and $\boldsymbol{n}$ is the flame front normal vector [9].

Another vital phenomenon for both laminar and turbulent flames is flame stretch. It is often used to characterize the effect of the flow field gradients on the flame front. The flame stretch definition is given in Eq. 2.2 [10].

$$\kappa = \frac{1}{A}\frac{dA}{dt} \tag{2.2}$$

where A is the instantaneous flame surface area. The definition of the flame stretch is therefore related to the rate of growth of the flame area divided by its area. It has

been shown in the literature that stretch values larger than some limit may cause the flame to extinguish [11].

2.1.1 Premixed Flames

A premixed flame occurs when the oxidizer and reactants are mixed at the molecular level before chemical reactions start. The laminar premixed flame configuration is essential for combustion science since this is the most elementary case for combustion research. Often this configuration is the only configuration for which a detailed comparison between numerical and experimental analysis results can be made. Furthermore, the premixed laminar flame configuration can be viewed as the building block of turbulent flames; indeed some approaches simplify turbulent flame modeling by describing it as a collection of instantaneous laminar flames called flamelets [12].

To parametrize the effect of the fuel-to-air ratio in premixed flames, a parameter called "equivalence ratio" is used. This parameter is defined as the fuel mass to the oxidizer mass ratio divided by the stoichiometric fuel-to-oxidizer mass ratio [12]. The stoichiometric fuel-to-oxidizer ratio refers to the ratio where there are just enough oxidizer molecules to oxidize all fuel molecules in the mixture. This parameter is defined in Eq. 2.3.

$$\emptyset(\boldsymbol{x}) = \frac{\frac{Y_{fuel}}{Y_{oxidizer}}}{\left(\frac{Y_{fuel}}{Y_{oxidizer}}\right)_{stoichiometric}} \qquad 2.3$$

This quantity is uniform in the unburned mixture for fully premixed flames. However, for partially premixed flames, depending on the injection location, injector geometry, fuel type, and fuel flow rate, this quantity can vary both spatially and

temporally. This can cause the flame to reach its lean or rich flammability limits. When this happens, in some positions, flames can extinguish and lead to incomplete combustion. This can increase the unburned hydrocarbon and CO emissions. When the equivalence ratio is non-uniform within the combustion volume, a "local equivalence ratio" describes the reactive mixture which determines the flame stability limits between blow-off (flame detached from the burner) and flashback.

2.1.2 Non-premixed Flames

A diffusion flame occurs when oxidizer and fuel flows meet in the flame zone. In diffusion flames, the fuel and oxidizer diffuse into each other with turbulent or molecular diffusion. In other words, they are not mixed before combustion. Thus, in a diffusion flame mixing and combustion occur quasi-simultaneously. This results in a flame structure that is more complex and heterogeneous than a premixed flame. Since the gases are not mixed before combustion, the local equivalence ratio parameter is not relevant for diffusion flames, but a global one can be used instead. In diffusion flames, the flame stabilizes on surfaces where mixing between the fuel and the oxidizer results in near-stoichiometric conditions. This results in higher flame temperatures, which in turn trigger higher emissions of harmful gases such as NOx.

2.1.3 Effect of the Volumetric Hydrogen Ratio in the Fuel

Hydrogen addition to fuels such as natural gas has several effects. These effects are primarily due to the physical and combustion characteristics of hydrogen. Hydrogen has a much higher flame speed than other fuels, such as natural gas. For example, hydrogen-air mixtures at room conditions with an equivalence ratio of 1 have a laminar flame speed of around $2\frac{m}{s}$. For reference, a natural gas flame in the same conditions has a flame speed of around $35\frac{cm}{s}$ [13]. Thus, the flame speed increases when hydrogen is added to a fuel mixture. Also, hydrogen has a much higher

molecular diffusion coefficient into other species than methane for example [14]. However, this is more relevant for laminar flames since turbulent diffusion is much more intense than molecular diffusion in turbulent flames [15]. This effect, coupled with higher flame speeds, results in a higher risk of flashback for both laminar and turbulent flames [16].

2.2 Swirling Flows

2.2.1 Characterization of Swirling Flows

Swirling flows are commonly used in many industrial applications, such as turbomachines, cyclone separators, combustion chambers, etc. Their main feature is the rotating motion of the fluid added onto the bulk fluid motion. Hence, the primary method of characterizing a swirling flow is comparing the momentum of the rotating fluid movement to the momentum of the axial movement of the flow. Different correlations for predicting the resulting swirl numbers for different swirler designs using their geometrical parameters have been presented in the literature [12]. These include the correlations for axial straight-blade swirlers and axial helical-blade swirlers. These correlations are presented in Eqs. 2.4 and 2.5.

$$S' = \frac{2}{3} * \left[\frac{1 - \left(\frac{R_h}{R}\right)^3}{1 - \left(\frac{R_h}{R}\right)^2} \right] tan\alpha \qquad 2.4$$

$$S' = \frac{1}{1-\varphi}\left(\frac{1}{2}\right)\frac{1 - \left(\frac{R_h}{R}\right)^4}{1 - \left(\frac{R_h}{R}\right)^2} tan\alpha_0 \qquad 2.5$$

Where S' denotes the geometric Swirl number, φ denotes the blockage ratio of the swirler blades, R_h denotes the hub radius, R denotes the tip radius and α_0 denotes

the angle of the blades at hub radius. Straight and helical blade axial swirlers are illustrated in Figure 2.1.

Since the straight blade swirlers have only one blade angle from the hub to the tip, in Eq. 2.4 the blade angle is denoted α. The relevant swirler dimensions are illustrated in Figure 2.2. Dimensions α_0, R_h, and R are illustrated in the helical swirler figure and dimensions α, R_h, and R are illustrated in the straight blade swirler figure. The correlation between the blade angle α_0 and the radius for helical swirlers is given in Eq. 2.6. For most of the industrial applications of swirling flows, the swirl number varies between 0.2 and 2 [17].

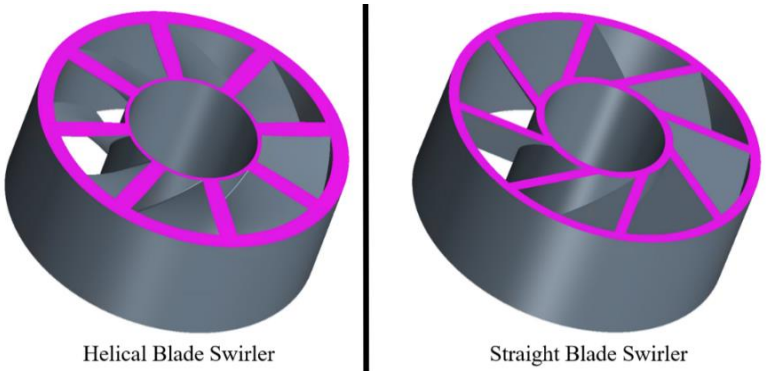

Figure 2.1. Straight and helical blade axial swirlers

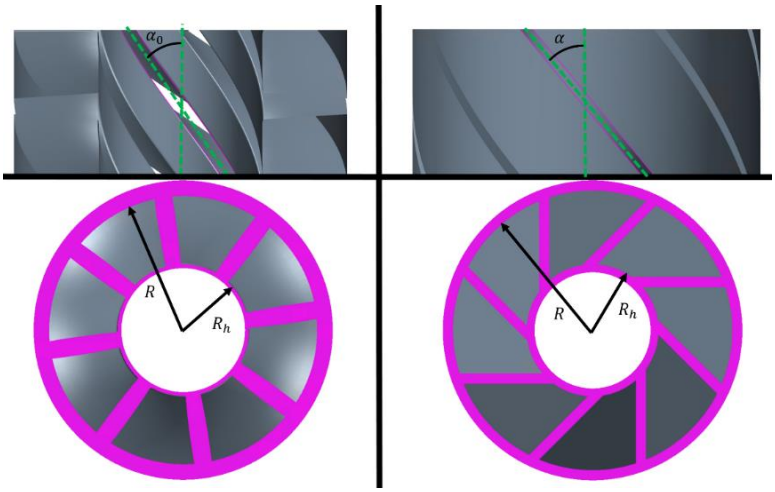

Figure 2.2. Blade dimensions illustrated

However, one parameter is not sufficient to characterize all swirling flows. Even though the swirl number is efficient for indicating the level and strength of the swirling movement in the flow, it does not give a complete idea about the distribution of the swirl along the radial direction [18].

2.2.2 Flow Swirling Methods

As described in the previous section, many industrial devices utilize swirling flows in their designs. However, there are many ways to impose a swirling motion on an axial flow. These include the following methods:

- Using vanes to impose a rotational motion.
- Using inlet ports positioned eccentrically in a tangential or helical direction to the axis of the main flow motion.
- Using components that rotate such as impellers, disks, or blades.
- Using external forces such as acoustic waves or magnetic fields.

Choosing which of these methods to use requires consideration of various factors such as the desired swirl intensity, pressure drop, flow rate, geometry of the overall design, and cost. For example, while eccentric inlets are used for cyclone separators, vanes are used for most gas turbine applications.

By using vanes for imparting a swirl on a fluid flow, the swirl intensity can be controlled more effectively. Furthermore, using a curved blade axial swirler, the pressure drop can also be kept at a relatively low value. For these reasons, in aero engines and gas turbines, axial swirlers are generally used. This, however, increases the complexity and the manufacturing cost of the swirler compared to other simpler methods, such as eccentric inlets. Swirler blades can be curved in any way along the radial direction. However, the blades that follow the correlation shown in Eq. 2.6, are a particular type of axial curved blades called helical blades. In this thesis work, an axial, helically curved blade was used.

$$\tan(\alpha) = \frac{r}{R} tan(\alpha_0)$$

2.6

2.2.3 Turbulence and Mixing in Swirling Flows

Turbulence is fundamental in many engineering applications, including gas turbine combustors. Every combustion chamber designed for a gas turbine works in a turbulent flow regime. For some applications, such as the outer aerodynamics of an aircraft, turbulence may be an adverse phenomenon because it increases drag forces. For gas turbine combustors, however, turbulence is almost always helpful. It enhances the mixing and wrinkles the flame. Both help to increase the combustion efficiency of the stabilized flame in the combustion chamber.

Turbulence is not an easy phenomenon to precisely define and analyze. It is characterized by spatial and temporal fluctuations of all flow parameters. Even though this means that the fluid flow appears irregular and unpredictable, turbulence is not entirely random. Elevated rates of dissipation and diffusivity also characterize it. Turbulent flows are often described by decomposing the flow parameters into its mean and fluctuating parts using time, spatial, or ensemble averaging. The method of describing turbulent flows in terms of their mean and fluctuating parts is called Reynolds decomposition. Reynolds decomposition is defined in Eq. 2.7.

$$\boldsymbol{u}(\boldsymbol{x}, t) = \bar{\boldsymbol{u}}(\boldsymbol{x}, t) + \boldsymbol{u}'(\boldsymbol{x}, t)$$

2.7

where $\bar{u}(\boldsymbol{x}, t)$ is the mean flow velocity in a particular position in space and time and $u'(\boldsymbol{x}, t)$ is its fluctuating part. A flow where the mean flow velocity does not change with respect to time is called stationary. No information about turbulence can be gathered from the mean flow velocities. Thus, to characterize the magnitude of the velocity fluctuations, the root mean square (RMS) velocity is used. The RMS velocity is defined as shown in Eq. 2.8.

$$u_{rms} = \sqrt{\overline{u'^2}}$$

2.8

Turbulence is further characterized by its time, length, and velocity scales. It is known that in turbulent flows, a wide range of fluid structures called eddies exist simultaneously. These eddies are constituted by an ensemble of fluid molecules having similar characteristic scales and are responsible for the transport properties associated with turbulence. The range of eddy sizes present in the turbulent flow field is determined by the extraction mechanisms of turbulent energy from the mean flow and by their further interactions where dissipative viscous forces play an important role.

The Kolmogorov hypothesis [19] describes the general characteristics of turbulence and defines several length, velocity, and time scales. They are called Kolmogorov length, velocity, and time scales, and they define reasonable lower limits for the observable turbulent scales in the flow. For example, they describe the size for the smallest possible scales for the fluctuations in the flow. These scales are described in Eqs. 2.9 to 2.11.

$$\eta = \left(\frac{\tilde{\nu}^3}{\tilde{\varepsilon}}\right)^{\frac{1}{4}}$$

2.9

$$\tau_\eta = \left(\frac{\tilde{\nu}}{\tilde{\varepsilon}}\right)^{\frac{1}{2}}$$

2.10

$$v_\eta = (\tilde{\nu}\tilde{\varepsilon})^{\frac{1}{4}}$$

2.11

η is the Kolmogorov length scale, τ_η is the Kolmogorov time scale and υ_η is the Kolmogorov velocity scale. Kolmogorov scales establish lower limits for turbulent fluctuations. On the other hand, the integral scale is defined as associated with the largest fluctuations in the turbulent flow. The value of the integral scale can be influenced by many aspects of the flow, such as the geometry of the flow volume or fluid properties.

According to the Kolmogorov theory, the energy transfer rate from large eddies at the integral scale is equal to energy dissipation rate at small-scale Kolmogorov eddies. In addition, another scale, named the Taylor microscale, is also used in turbulence studies. The Taylor microscale is defined as the scale at which the fluid's viscosity starts to significantly affect the turbulence dynamics [20]. In Figure 2.3 these scales are illustrated in a turbulence energy power density spectrum versus frequency plot (we may recall here that when the eddy frequency increases its the wavelength decreases).

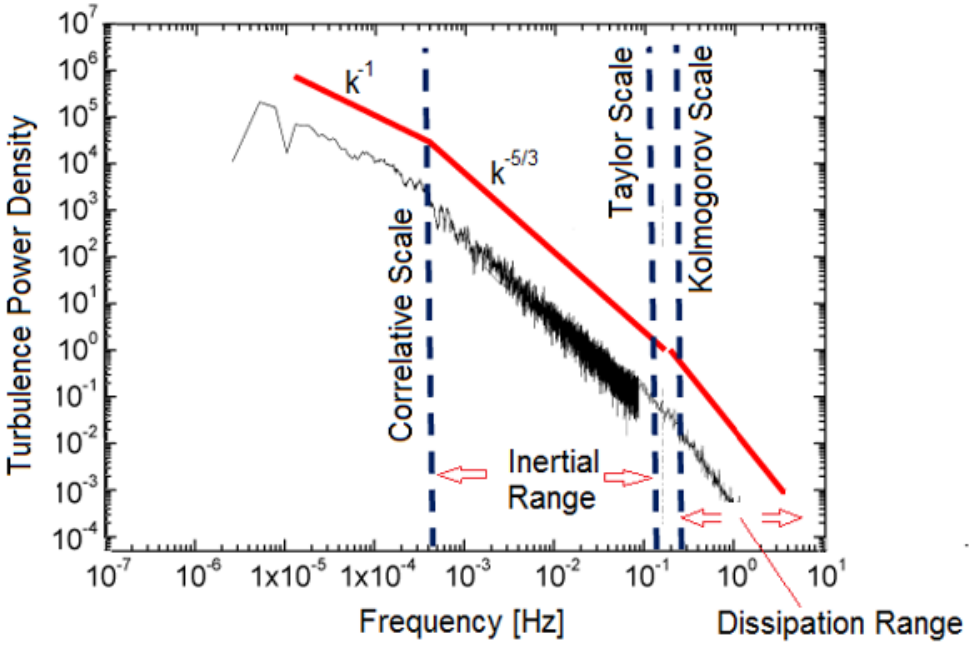

Figure 2.3. Turbulence power density vs eddy frequency plot [20]

Finally, isotropy and homogeneity are important concepts for the characterization of turbulence. Isotropic turbulence refers to the type of turbulence in which all turbulence properties in the flow are the same for all three spatial directions. This implies that the probability density functions of the velocities at any location in the flow do not change for different space directions. The advantage of isotropic turbulence when it comes to studying turbulence is that a minimal number of correlations are needed to describe its structure and dynamics. Even though no turbulent flow in real life is truly isotropic, local isotropy is often assumed to characterize and analyze turbulence. Homogenous turbulence refers to turbulent flows where turbulent properties do not vary spatially. Homogeneous and isotropic turbulence (HIT) is usually used for modelling turbulence. In simplest terms, HIT is a form of turbulence that displays the same characteristics at every position and in every direction.

An essential characteristic of turbulence in high curvature flows such as swirled flows is its anisotropy. Compared to other types of flows, swirled flows and other high-curvature flows create more anisotropic turbulence characteristics [21]. Most Reynolds-averaged Navier-Stokes (RANS) turbulence models assume isotropy, such as the k-omega and k-epsilon models. This makes it difficult for most RANS models to predict swirled flow fields accurately.

2.2.4 Flow Instabilities and Secondary Flows

The primary flow feature in a swirling flow is the superimposed rotational and axial motions. However, other secondary flow features of swirling flows are also crucial in flame stabilization. One of the most important is the upstream axial motion in the central recirculation zone (CRZ). The main features of a swirling flow are illustrated in Figure 2.4. These features are CRZ (central recirculation zone), swirling jet, outer recirculation zone (ORZ), internal shear layer (ISL), and outer shear layer (OSL) [9]. In a swirl stabilized flame, the axial upstream flow in the CRZ picks up hot burnt gases from downstream and carries them upstream. This ignites the fresh fuel-

oxidizer mixture in the annular swirling jet, stabilizing the flame. ORZ is a larger toroidal vortex between the swirling jets and the free stream or chamber walls. The effect of ORZ on the flow and flame stabilization is shown to be important in the literature [22]. ISL and OSL are developed in the flow due to large velocity gradients between ORZ, CRZ, and the swirling jets. These shear layers then create suitable flow conditions for a flame to stabilize. In these shear layers, Kelvin-Helmholtz instabilities (KHI) are also present [23]. KHI is an instability that occurs when there is a velocity difference between two fluid streams with different densities. It causes small perturbations that grow and form vortices [24]. This instability enhances mixing between the burnt gases brought upstream by the CRZ and the fresh mixture brought by the swirling jets.

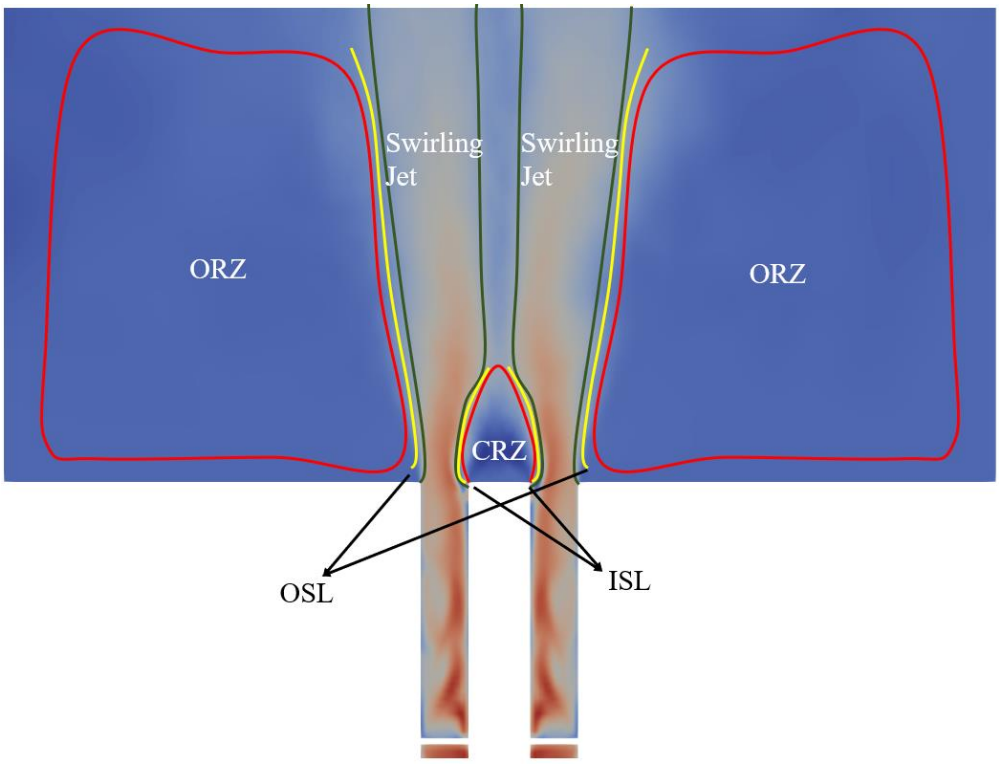

Figure 2.4. Main features of a swirling flow illustrated with the velocity magnitude contours

The CRZ is formed through a process known as vortex breakdown. A sufficiently strong swirl must be given to the flow for vortex breakdown to occur. Swirl numbers

lower than a certain threshold will not result in a vortex breakdown; consequently, no CRZ will be formed. This lower limit for the swirl number is not universal and can have different values for different geometries or flow conditions [9]. However, swirl numbers lower than 0.4 generally do not result in vortex breakdown and CRZ [25]. In addition to the vortex breakdown, the central cylinder (called the centerbody) in the duct center also contributes to the upstream axial flow in the CRZ by creating a wake flow. In low swirl number flows, or low centerbody diameters, the wake region created by the centerbody, and the reverse flow region created by vortex breakdown can separate and appear as different regions in the mean flow contours [23]. However, for larger swirl numbers such as the one used in the study for this thesis, the vortex breakdown bubble and wake region are merged and result in a single CRZ.

Another essential secondary feature of swirled flows is the precessing vortex core (PVC). PVC is a coherent flow structure shaped like a helix. It occurs in flows involving vortex breakdown [26]. PVC is a common feature in swirl-stabilized flames. It affects the swirl-stabilized flame's structure, emissions, and stability [27]. PVC occurs in the ISL zone where the flow is susceptible to hydrodynamic instabilities [28]. The PVC has a frequency by which it propagates down the CRZ. It also has an azimuthal mode which determines the number of its helical arms [29]. Several methods, such as pressure probes, optical diagnostics, or numerical simulations, can detect the PVC.

2.3 Swirl-Stabilized Flames

2.3.1 Combustion Modes

There are several modes by which swirl-stabilized combustion can be operated. Two of them are relevant for this thesis. These are premixed and partially premixed modes. These two modes are discussed in the following two sections.

2.3.1.1 Partially Premixed Mode

In the partially premixed mode, the fuel and oxidizer are mixed along the duct where the swirled jet flows. Typically, the fuel injection location lies downstream of the swirling blades. How close this point is to the burner exit and the flame determines how close the flame is to a fully premixed or a non-premixed one. A partially premixed swirl burner setup is illustrated in Figure 2.5.

The topic of partially premixed burners is becoming more relevant in recent years due to their low emission characteristics regarding harmful gases such as NOx and their resistance to flame flashback. Since partially premixed burners do not have fully premixed gas mixtures up to their exit sections, they cannot experience full flashback. However, they can still experience shifts in flame stabilization characteristics, such as lifted flames becoming attached to the burner surfaces. This, in turn, can make the operation of the burner harmful to the components by heating them to undesired values but cannot result in catastrophic failures such as explosions, which can happen in fully premixed burners experiencing flashback. Considering the elevated risk of flashback caused by hydrogen addition, in this thesis work a partially premixed burner was used.

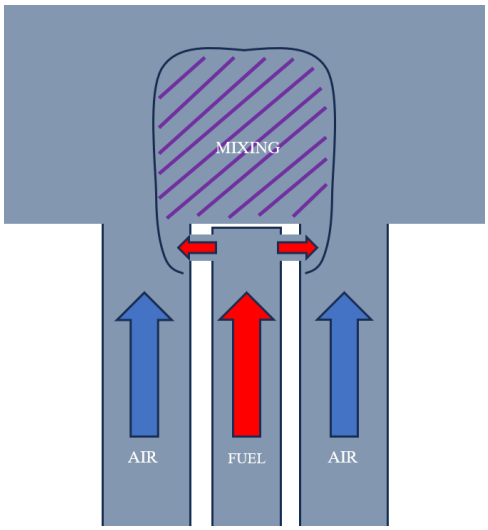

Figure 2.5. Illustration of a partially premixed burner

2.3.1.2 Fully Premixed Mode

As mentioned in the previous section, swirl-stabilized burners can also be operated under fully premixed mode. This means that before the annular flow is swirled by blades, the fuel and oxidizer are premixed, for example, with an in-line static mixer. A swirl burner configuration that uses this mode is illustrated in Figure 2.6.

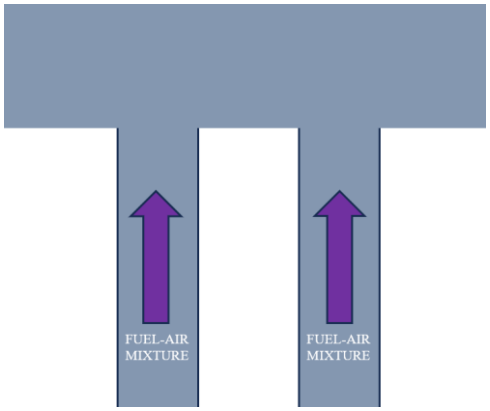

Figure 2.6. Illustration of a fully premixed burner

There are several advantages to using fully premixed swirl burners. The most important is that in fully premixed flames, harmful gas emissions such as NOx are lower than partially premixed ones. The difference in emission values would change depending on how early the fuel is injected in the partially premixed burner and how effective is the partial premixing. One significant disadvantage of the fully premixed burner mode is the tendency to flashback. Furthermore, since this thesis uses fuel mixtures containing hydrogen, flashback risk is considerably elevated. More details about the flashback phenomenon are given in later sections.

2.3.2 Combustion Instability

Several instability modes are relevant for swirl-stabilized combustion. These instabilities determine the flammability and operability limits of swirl-stabilized burners. These instabilities are flashback and blow-off. In the following sections, these instabilities are detailed.

2.3.2.1 Blow-off

Blow-off occurs in burners when the aerodynamic strain imposed on the flame partially extinguishes it and separates it from the stabilization zone [30]. For all kinds of burners, blow-off will result in loss of power, instability, and unburned fuel emissions. The ratio between aerodynamic strain rate and the chemical heat release rate mainly governs the blow-off phenomenon. The aerodynamic strain rate in swirl-stabilized burners mostly depends on the turbulence characteristics and the bulk velocity of the swirling jet. On the other hand, the chemical heat release rate depends on the type of fuel used, the equivalence ratio, pressure, and unburned gas temperature [31]. Considering this, in any swirl burner design, the air flow rate and swirl number must be chosen carefully to account for the type of fuel used, expected equivalence ratio field, pressure, and unburned gas temperature.

2.3.2.2 Flashback

For swirl burners, there are four relevant flashback mechanisms. These are combustion-induced vortex breakdown (CIVB), boundary layer flashback (BLF), flashback due to combustion instabilities, and flame spread in the high-speed primary flow [32]. These flashback modes are detailed below.

- Combustion-Induced Vortex Breakdown

  This phenomenon is mainly observed in swirl burners with a small diameter centerbody or no centerbody. The design of swirlers without a centerbody always requires more detailed tailoring of the swirled flow [33], since the wake region from the centerbody does not exist, and the only phenomenon aiding in stabilizing the flame is the vortex breakdown. Furthermore, the formation of the vortex breakdown strongly depends on parameters such as geometry, flow conditions, etc. In swirl numbers exceeding a critical point, the recirculation zone arising from vortex breakdown can extend to regions inside the burner duct.

Studies show that even for well-designed swirl number burners, the existence of combustion can lead to this phenomenon [33].

- Boundary Layer Flashback

The boundary layer flashback phenomenon is essential for both turbulent and laminar burner designs. Boundary layer flashback depends on a balance between the flame's quenching distance and the fuel-air mixture's velocity profile close to burner walls [34]. When the flame can penetrate near enough to the wall without losing enough heat to slow down, it can propagate upstream the burner and cause a flashback. Recent studies have shown that adding hydrogen affects this balance in a direction that makes the flame more susceptible to flashback [16]. This fact is relevant for this thesis since hydrogen and natural gas mixtures are used in the experiments. To analyze the flame flashback dynamics, a parameter called the critical velocity gradient is proposed by Lewis and von Elbe, which is given in Eq. 2.12

$$g = \left.\frac{\partial u_{axial}}{\partial r}\right|_{R_{inner}} = \frac{S_L}{d_q} \tag{2.12}$$

Where g denotes the critical velocity gradient, r denotes the radial distance from the center of the tube, R_{inner} denotes the inner radius of the tube, S_L denotes the laminar burning velocity of the flame, u_{axial} denotes the velocity along the pipe axis and d_q denotes the quenching distance of the flame where the flame loses enough heat to make it unable to propagate upstream.

- Flashback due to Combustion Instabilities

Swirl-stabilized combustion systems, especially in aero engines, are almost always subject to high acoustic disturbances. In some situations, these disturbances can couple with the heat release rate fluctuations of the flame [35]. These so-called thermoacoustic instabilities can then cause upstream flame propagation in both free stream and the boundary layer regions[36].

- Flame Spread in the High-Speed Primary Flow

This flashback mode is the most straightforward among others and can be summarized as follows. The flame propagation velocity exceeds the flow velocity in the turbulent primary jet and propagates upstream through it. Even though the definition is simple, analysis of this phenomenon is challenging. This is due to the difficulty of predicting the turbulent propagation velocity of the flame. Studies have been published that try to correlate turbulent flame propagation speeds to the characteristics of the turbulent flow and laminar flame propagation speeds [37–39].

2.3.3 Flammability and Stability Limits

The flammability and stability limits of a swirl-stabilized burner can be determined using experimental or numerical methods. In the literature, studies mostly use experimental methods to determine the flammability and stability limits of different types of swirl burners [40–42]. Often these studies present their results in a flammability or stability map. These maps consist of a plot where one axis is the equivalence ratio or the fuel flow rate, and the other is the air flowrate, pressure, or other parameters. The difference between flammability and stability maps is that flammability maps illustrate the range where the burner can be ignited without any stable flame present initially, and stability maps represent the range where the burner can sustain a flame when there is already a flame stabilized on it. The stable or flammable regions in both maps are bordered by flashback and lean blowoff.

2.4 Swirl Stabilized Flame Research

There are many studies focused on the swirl stabilized flame phenomenon. These studies include burners working with liquid or gaseous fuels, partially premixed, fully premixed, and diffusion burners and burners with different types of oxidizers and fuels. However, particularly relevant studies for this thesis are partially premixed

and fully premixed swirl-stabilized flame studies. A significant part of these studies is conducted at the CNRS-ICARE institute in Orléans, France. Moreover, the burner design used for this thesis was inspired by the experimental setup at the ICARE institute. Relevant studies are summarized in this section.

2.4.1 Effect of Oxygen Enrichment on Swirl-Stabilized Flames

In their study published in 2019 named “Experimental investigation of CH4-air-O2 turbulent swirling flames by Stereo-PIV” [43], Boushaki et al. experimentally investigated the dynamic characteristics of partially premixed turbulent swirling flames using the stereo-PIV technique. Atmospheric and oxygen enriched air was used in the experiments with the volumetric oxygen ratio ranging from 21% to 30%. The authors have determined that oxygen enrichment in this range moves the flame closer to the burner exit, which means it lowers the lift-off height. The authors also noted that the oxygen enrichment between 21% and 30% causes the flame volume to increase. Authors attribute this effect to the fact that with higher oxygen content in air, the flue gas expansion rate increases. Additionally in their 2013 paper [40] Merlo et al. have determined that higher oxygen enrichment rates resulted in higher flame temperatures and lower lift-off heights.

Additionally, Jerzak et al. studied premixed swirl stabilized flames using a radial swirl burner experimental setup. Their study was titled “Experimental study of impact of swirl number as well as oxygen and carbon dioxide content in natural gas combustion air on flame flashback and blow-off” [44] and was published in 2015. In their study the researchers analyzed the stability regime of the swirl stabilized flame under different conditions. One of the conclusions of the study was that oxygen enrichment resulted in a higher risk of flashback. However, researchers also noted that oxygen enrichment resulted in better flame blow-off limits.

2.4.2 Effect of Exhaust Gas Recirculation and Water Dilution on Swirl-Stabilized Flames

Exhaust gas recirculation (EGR) and water dilution are important areas of study regarding the reduction of pollutant emissions such as NO_x. In their study published in 2018 named "Effects of exhaust gas on CH_4-air-O_2 turbulent swirling flames" [45], Zaidaoui et. al. experimentally studied the effects of exhaust gas recirculation and water dilution on swirl stabilized flames among other parameters. Researchers used flame the chemiluminescence technique to determine the lift-off height of the swirl stabilized flame. They determined that increasing EGR from 0% to 20% volumetric ratio increases the flame lift-off height. Additionally, they determined that water dilution also resulted in increased flame lift-off height. Researchers also noted that EGR results in a less stable flame compared to water dilution and compared to the flame without EGR or water dilution. Researchers also noted that both water dilution and EGR result in decreased NO_x emissions.

Similarly, Vandel et al. in their 2020 paper entitled "Study of the influence of water vapor and carbon dioxide dilution on flame structure of swirled methane/oxygen-enriched air flames" [46] analyzed a premixed swirl-stabilized flame experimentally. The researchers determined that water dilution of the mixture results in a higher flame length and lift-off values. They further concluded that CO_2 dilution has similar effects to water dilution with increasing of the flame height being larger than with water dilution.

In their study Jerzak et al. [44] also determined that CO_2 dilution on premixed swirl-stabilized flames results in an improvement of the flame flashback limits but a worsening of the flame blow-off limits. Researchers attribute this effect to the decreasing laminar flame speed resulting from CO_2 dilution.

2.4.3 Effect of Swirl Number on Swirl-Stabilized Flames

The effect of swirl number on swirl-stabilized flames is an essential factor for all swirl burner applications. In their study named “Numerical computations of premixed propane flame in a swirl-stabilized burner: Effects of hydrogen enrichment, swirl number and equivalence ratio on flame characteristics” [47], Mansouri et. al. has determined that higher swirl numbers result in a shorter flame. Authors also noted that higher swirl numbers result in lower CO emissions.

Additionally in their 2013 research paper named “Experimental study of oxygen enrichment effects on turbulent non-premixed swirling flames” [40], Merlo et al. analyzed partially premixed swirl-stabilized flames experimentally. In their study the authors worked with 0.8 and 1.4 geometric swirl number blades. They determined that 0.8 swirl number results in a higher lift-off height.

Huang et al. numerically analyzed a lean premixed swirl-stabilized flame in their 2005 study entitled “Effect of swirl on combustion dynamics in a lean-premixed swirl-stabilized combustor” [48]. They used the LES model in their study. They found that higher swirl numbers result in smaller flame lift-off heights. The researchers attribute this effect to the fact that with higher swirl numbers, the CRZ moves upstream. They also remarked that with the CRZ moving upstream and the flame getting closer to the burner, flashback risk is increased.

2.4.4 Effect of Global Equivalence Ratio on Swirl-Stabilized Flames

The global equivalence ratio is an important parameter for partially premixed burners. Since the local equivalence ratio is non-uniform, a global parameter is defined using the fuel and oxidizer flow rates. In their 2016 study named “Study of pollutant emissions and dynamics of non-premixed turbulent oxygen enriched flames from a swirl burner” [49], Boushaki et. al. experimentally analyzed a swirl stabilized flame with different global equivalence ratios. In their study, the authors determined that the global equivalence ratios ranging from 0.8 to 1 lead to a higher

flame lift-off height. The authors also noted that the NO_x emissions of the flame decreased with the global equivalence ratio ranging from 0.8 to 1. This effect is interesting since the flame temperatures go up when the equivalence ratio is closer to 1. The authors noted that this decrease might be due to increased CO_2 recirculation for the unity global equivalence ratio flame.

As can be observed from this summary of the research activities that inspired this thesis and the burner configuration, the previous research did not concentrate on the hydrogen addition effects on partially premixed swirl stabilized turbulent natural gas flames. The main contribution of the present thesis is therefore to analyze, experimentally and computationally, the hydrogen addition effects on swirl stabilized natural gas flames, together with the first development in Türkiye of the used experimental facility.

2.5 Experimental Methods for Analyzing Swirl-Stabilized Flames

This section presents experimental methods for analyzing swirl-stabilized flames and burners. Extra details are given for the methods used in this thesis work.

2.5.1 Laser-Based Diagnostic Methods

- Planar Laser Induced Fluorescence (PLIF)

  PLIF uses a laser sheet directed at the flame to excite specific molecules in the flame region. These molecules include OH, CH, O radicals, and formaldehyde. These species are called fluorescent species. A camera situated towards the flame region then collects the light emitted by the excited molecules. PLIF is used to create 2-D sections of the flame front. In these 2-D sections, PLIF can provide data on the concentration of fluorescent species [50, 51]. The concentration data for some fluorescent species like OH and CH are then used to locate the flame front since these species are primarily present around the flame front [52]. The

same method can be used with a one-dimensional laser ray to analyze species concentrations on a one-dimensional line. This method is called laser-induced fluorescence (LIF).

- Laser Induced Incandescence (LII)

This method determines the soot concentration and distribution in and downstream of flames. Typically, a laser sheet is used to heat the soot particles, which causes them to emit incandescent light. Incandescent light is the visible light emitted by a hot object. A camera then captures this light with filters calibrated to the relevant frequency [53]. For combustion chambers using swirl burners, LII can show where the soot particles are created and how to prevent their formation. This is often a crucial aspect of gas turbine or aero-engine combustion chambers since the soot particles play a significant role in heating the combustion chamber walls through radiation.

- Rayleigh scattering (RS)

Rayleigh scattering uses a laser beam or a laser sheet to determine the temperature and density of the gases in the flame zone. After the flame zone gases are illuminated with a laser, a camera picks up the emitted light from the flame zone. This then reveals the temperature and density field within the flame region [54]. Rayleigh scattering is an optical phenomenon that occurs when light or other electromagnetic radiation interacts with particles significantly smaller than the radiation's wavelength. These particles can be atoms, molecules, or microscopic density fluctuations in a medium. It is named after Lord Rayleigh, the British physicist who studied and contributed to its understanding in the late 19th and early 20th centuries.

- Laser Induced Breakdown Spectroscopy (LIBS)

LIBS method utilizes a high-intensity laser, focused on the flame region to create plasma. The light emitted from this plasma is then spectrally analyzed to determine the elemental composition of the flame. LIBS is used to obtain a more

comprehensive picture of the chemical composition of the flame regarding the types of species [55].

- Tunable Diode Laser Absorption Spectroscopy (TDLAS)

TDLAS method works based on the phenomenon of light absorption of species present in the flame region. In TDLAS, lasers tuned to specific frequencies probe the absorption frequencies of targeted species in the flame region. Using the TDLAS method, concentration data on species such as methane, carbon dioxide, or water vapor can be collected [56].

- Particle Image Velocimetry (PIV)

Velocity field measurement methods such as PIV are commonly used in analyzing a swirl burner. The PIV method uses flow seeding and a laser sheet to illuminate the seed particles to collect data on the velocity field. The laser illuminates the flow field seeded with particles in two pulses very close to each other. The flow field is pictured by a high-speed camera during these two pulses. The velocity vector field is then determined using the two pictures [57]. In swirl-stabilized burners, PIV is used to characterize important information such as the strength of swirling motion, size of the CRZ, or vortex structures in the flame zone. However, when a flame is present, most seeding particles used in PIV analyses are burned when encountering the flame. This makes it very hard to analyze reacting flows using the PIV method.

- Laser Doppler Velocimetry (LDV)

The LDV method uses two lasers beams to determine the flow velocity in a single point of the flow region. In the LDV method, based on the Doppler effect, two laser beams intersect on the point of interest. The flow is seeded, and when the seed particles go through this intersection volume, they reflect the laser light in a wave pattern while they go through the bands of low and high-intensity light regions. A high-speed camera then picks up this reflection signal and, according to the frequency of the signal, can determine the speed of the particle traveling

through the intersection volume [58]. As the seeding particles are sufficiently small to be entrained by the flow streamlines without a relative velocity, the measured seeding particles velocities are assumed to represent the instantaneous gas flow velocities.

- Laser Induced Mie Scattering (MS)

Mie scattering is the simplest laser-based method for determining the velocity field in a flow field. It is based on the light scattering by elastic collisions between the laser photons and small particles seeded in the flow. In the MS method, the flow is seeded, and then the flow region is illuminated by a laser sheet. A high-speed camera captures the resulting image, and this is used to qualify the flow field [52]. Mie scattering can also analyze the droplet field and characteristics in liquid injection swirl burners [53]. It can be used to determine the size, concentration, and velocity of droplets or the cone angle of the liquid fuel injector. Finally, since the seed particles will also burn when they encounter the flame in MS, it can be used to track the flame front position in the planar section of the laser sheet as the interface between regions where the light is scattered or not.

2.5.2 Flame Chemiluminescence Imaging

Flame chemiluminescence imaging is a line-of-sight optical experimental technique that uses certain frequencies of light emitted by certain species in the flame region. These species include OH*, CH*, C2* and CO2*. The asterisk (*) character at the end of the species symbol means the species are excited [59]. Chemiluminescence imaging uses a high-speed camera, an image intensifier, and a filter corresponding to a specific species. The filter only lets through the light from the species of interest. The image intensifier intensifies the image so that the light intensity goes up to a value that is sensible by the camera. Finally, the camera collects the intensified image. Chemiluminescence imaging can provide information on flame structure,

position, heat release rate, ignition, and extinction. It is commonly used in combustion control devices. In the literature, CH* and OH* are most commonly used for locating the flame front since several studies have shown that signals from these species are the closest to representing the flame front [60–62]. In this thesis, OH* line-of-sight results have been used to determine the flame position and dimensions. Filters with different frequency values are used to differentiate the signals from different types of radicals. Chemiluminescence imaging can be used in both line-of-sight and 3-D imaging modes. While line-of-sight 2-D imaging mode can be achieved with only one camera system, for 3-D imaging mode, several different camera systems must work simultaneously. The captured images from different cameras are then used in the tomographic reconstruction of the flame [63]. This increases the cost and complexity of the system, especially considering that a central processing unit must synchronize all the camera systems.

Using chemiluminescence imaging in swirl-stabilized combustion research has some advantages and disadvantages. The main advantage is the relatively simple and cheap system compared to laser-based systems that determine flame position. It does not require any external light source such as a laser light source. Some disadvantages to the system are as follows. Its most common use case only provides a 2-D line-of-sight image. Even when used in its 3-D form, it still determines the 3-D flame shape by integrating several 2-D line-of-sight images. This means it is less accurate than systems like PLIF when collecting data inside the flame. However, 2-D line-of-sight images can still provide valuable information about inside of a flame when the data is processed using methods like inverse Abell transform. It is also often sensitive to background noise since it uses an image intensifier. Finally, to obtain any quantitative results from chemiluminescence images, a calibration process is needed.

2.5.3 Other Optical Methods

- Schlieren Imaging

Schlieren imaging is a method where density gradients in a flow are visualized. A knife edge, a mirror, a light source, and a camera are used. Since in combustion systems, gases going through the flame front change their density significantly, this method can be used to analyze flames. Schlieren imaging is mainly used in spherical bomb experiments to determine the laminar flame speeds [64], by locating the spherically expanding flame front.

- Shadowgraphy

The Shadowgraphy method uses a light source and a camera to capture differences in fluid's refractive index in a flow. It is commonly used when analyzing the spray cone characteristics [65].

2.6 Numerical Modelling of Turbulent Flames

Numerical modeling of turbulent flames is often performed using computational fluid dynamics (CFD) solvers. To model turbulent combustion, these solvers solve the Navier-Stokes equations (continuity and momentum) coupled with a combustion model. This combustion model can be as simple as assuming infinitely fast chemistry with a global reaction mechanism or can be as complex as solving a chemical kinetics mechanism with hundreds of chemical reactions and dozens of species using Arrhenius equations. Even though there are many models to solve the non-reactive side of the governing equations, since the topic of the thesis is combustion, only the relevant combustion models are added to this literature survey. The governing equations being solved are detailed in the numerical setup section.

2.6.1.1 Combustion Modelling

There are two main approaches for modeling combustion. One is the assumption that turbulent mixing processes have a much larger time scale than the chemical reactions of the combustion process. This approach is called the fast-chemistry assumption. The other main approach is where chemistry processes are not assumed to be much faster than turbulent mixing processes. In this approach, the effect of turbulent vortices on the chemical processes is modeled [66]. To characterize the relationship between the turbulent mixing process time scales and the chemical reactions time scales, the Damköhler number (Da) is often used [67]. It is defined as the reaction rate divided by the convective mass transport rate. A Damköhler number significantly larger than 1 (Da >> 1) indicates fast chemistry. Da close to or smaller than 1 indicates on the other hand that turbulent mixing processes have comparable time scales to those of the chemical processes.

- Finite-Rate Chemistry (FRC) Model

  The FRC model calculates the reaction rates using a chemical kinetics mechanism. When FRC is used, all the chemical reactions described in the chemical kinetics mechanism are modeled by solving the corresponding Arrhenius equations. As mentioned, this model is frequently used for flames where Da is close to or smaller than 1. The Arrhenius equation used for calculating the reaction rate is given in Eq. 2.13.

$$\mathrm{K} = \mathrm{A}e^{-\frac{E_A}{RT}} \tag{2.13}$$

  Where K denotes the reaction rate constant, A denotes the pre-exponential factor, e is the Euler's number, R is the universal gas constant, E_A denotes the activation energy, and T is the temperature in Kelvin. Using the calculated reaction rate constant, the rate of progress of the reaction can be calculated using Eq. 2.14 [12].

$$Q = \text{К}\Pi_{k=1}^{N} \left(\frac{\rho Y_k}{W_k}\right)^{\nu_k'}$$

2.14

Where N is the number of reactants.

- Eddy Break-Up (EBU) Model

EBU is a common turbulence-chemistry interaction model used in many combustion chamber simulations. The primary assumption in standard EBU is that the chemistry effect on the reaction rate is negligible in turbulent combustion. It assumes that the mixing rate of reactants and products mostly governs the reaction rate. The standard EBU model also assumes that the mixing of products and fresh fuel-oxidizer mixture is a function of the stretching process created by turbulent eddies. Thus, the model's reaction rate is correlated to the turbulence kinetic energy dissipation rate ε. Since the effect of chemistry is not considered in the standard EBU model, no detailed description of the chemical process, such as chemical mechanisms, is needed for the model to work. Only the stoichiometric coefficients and the heat of reaction for the involved reactions are needed [68]. In addition to the standard EBU model, there is the hybrid EBU model. In the hybrid EBU combustion model, reaction rate calculation is based on the Arrhenius approach and Eddy Break-up combustion models. This model calculates reaction rates by considering both chemical kinetics and turbulent mixing. Among these reaction rates, the lower one is selected as the reaction rate.

- Flamelet Generated Manifold (FGM) Models

FGM is a tabulated chemistry model that assumes a set of 1-D flamelets can describe a multi-dimensional flame. The model's primary purpose is to reduce the number of dimensions of the chemical space. By assuming that a set of 1-D flamelets can describe the flame, the FGM method also assumes that chemical processes are faster than transport processes [69]. This assumption may fall short of being accurate when certain types of combustion systems where turbulent

diffusion processes are as fast as or faster than chemical processes. Such devices include RAMJET or SCRAMJET combustion chambers. However, FGM is suitable for relatively low-speed combustion often encountered in gas turbines or aero engines [70].

The FGM model uses detailed chemistry data only when constructing the manifold tables. The number of dimensions of the table can be modified according to the complexity of the simulation. Most basic FGM tables may only have two dimensions, and complex ones used in research today can have four or five dimensions. These dimensions include the fuel mixture fraction (MF), the progress variable (PV), the mixture fraction and the progress variable variances, and the heat loss ratio [71]. In the simulations, the FGM model solves the progress variable (PV) and the mixture fraction (MF) transport equations. PV indicates the completeness of the combustion process. A PV value of 0 means an unburned mixture and a PV value of 1 means an entirely burned mixture. Conversely, MF denotes the fraction of the fuel within the mixture. An MF value of 0 means a mixture of pure oxidizer. An MF value of 1 means pure fuel.

All the relevant state parameters are calculated beforehand and tabulated for FGM simulations. In the calculation of these tables, detailed chemical mechanisms are used. These mechanisms are used with 1-D or 0-D reactor solvers to create the tables.

FGM model can be used coupled with turbulence-chemistry interaction models to simulate more accurately the production of the PV parameter [72].

- Thickened Flame Model

TFM is a turbulence-chemistry interaction model that aims to model the turbulent flame front in grids coarser than the flame thickness. Since, for most combustor simulations, resolving the domain with numerical cells smaller than the flame thickness is not feasible because of large computation costs, the TFM model is used. It simulates the flames using a thickening factor F. The model uses the F

parameter to increase the reaction rate and decrease the transport coefficients by a factor [73]. TFM also assumes that chemical processes are much faster compared to transport processes, resulting in the flamelet assumption. The TFM model tabulates the laminar flame speed and laminar flame thickness of the relevant fuel-air mixture. During the simulations, the model uses these tables and numerical cell sizes of the mesh to compute the factor F. It is shown that the correlation choice for the thickening factor can affect the simulation results drastically [74].

CHAPTER 3

EXPERIMENTAL METHODOLOGY

3.1 Experimental Setup

This section details the experimental setup used in the thesis work. The experimental setup consists of the following parts:

- Experimental swirl burner
- Air supply system
- Fuel bottles
- In-line static gas mixer
- Piping
- Optical diagnostics systems
- Mass flow controllers

The sketch of the experimental setup is given in Figure 3.1.

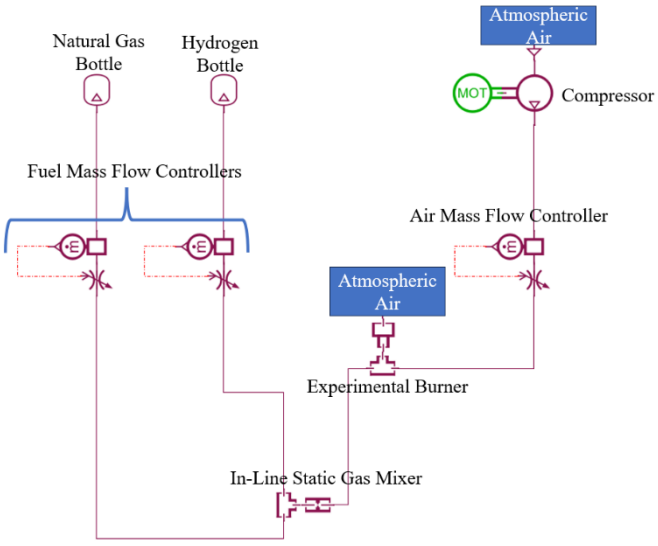

Figure 3.1. Sketch of the experimental setup

In the following sections, these parts, together with the experimental procedure, are detailed.

3.1.1 Swirl Burner Design

The swirl burner design used in the thesis work is inspired by the experimental swirl burner in the ICARE laboratory in Orléans, France [43]. The burner is a swirl-stabilized one with axial swirler blades situated inside an air duct, and the fuel is radially injected through a central fuel pipe into the swirling air flow. Taking inspiration from this design, the experimental swirl burner for this thesis was designed. The experimental swirl burner is shown in Figure 3.2.

Figure 3.2. A photo of the experimental swirl burner

The burner consists of an annular air duct where the swirling blades are situated. The duct is designed so that the axial position of the swirling blades can be adjusted by re-manufacturing small cylindrical metal pieces. For all the experiments, however,

the blades were situated with their tops at a constant distance from the burner exit. The swirling blades are designed to produce a swirl number of 1.4 with eight blades. The blade geometry was created using Eqs. 2.5 and 2.6. The blades were designed with a helical geometry. The helical blade geometry,1.4 geometric swirl number and α_0 of 60 degrees were determined using Eq. 2.3. The blades were manufactured using selective laser melting (SLM) and finished using electro-discharge machining (EDM). The geometry of the blades is shown in Figure 3.3 with a cad geometry.

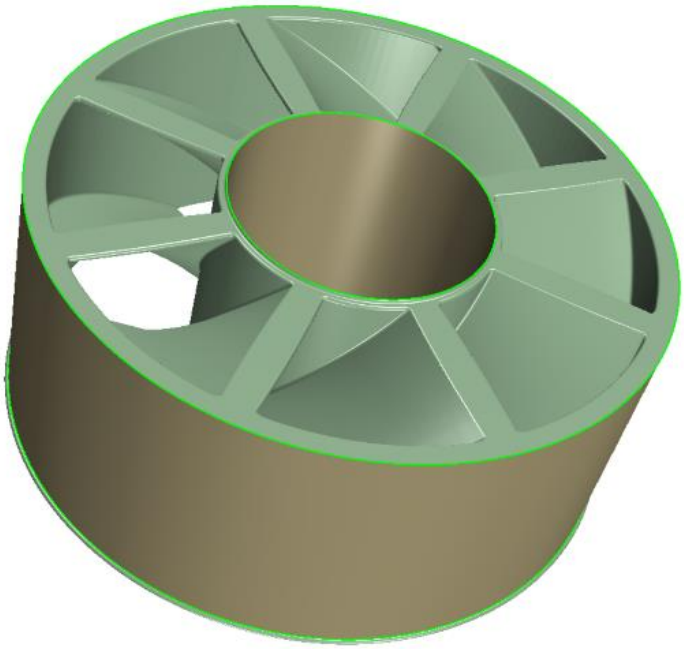

Figure 3.3. An illustration of the swirling blades

The outer air duct walls and most of the inner fuel duct were made of stainless steel using conventional manufacturing methods. At the tip of the central fuel pipe, eight radial holes were drilled to inject the fuel into the swirling air flow. These holes were drilled straight in the radial direction. The tip of the central fuel pipe, where the injection holes are drilled, was manufactured from brass as this part of the burner was predicted to become the hottest relative to other metal parts. The central fuel pipe outlet is illustrated with the outer air duct wall in Figure 3.4.

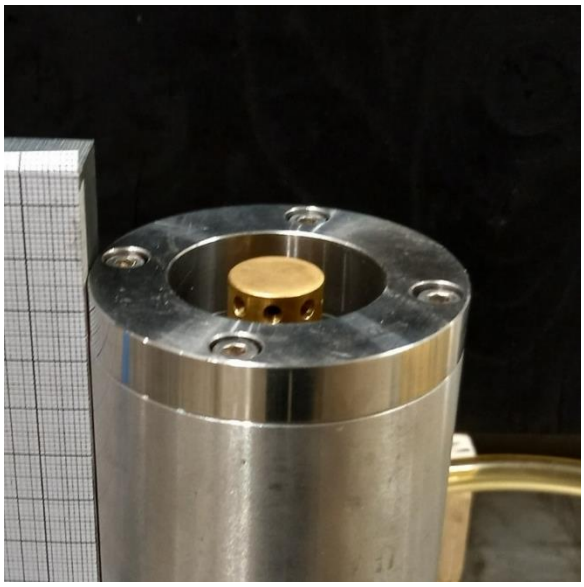

Figure 3.4. A photo of the experimental burner exit

Finally, four air inlets and one fuel inlet were opened at the bottom of the swirl burner. The air inlets were opened in the annular wall in a radial direction to achieve a homogenous velocity profile before the swirling blades. The air and fuel inlets are illustrated in Figure 3.5, along with the rest of the design with a 3-D sketch section.

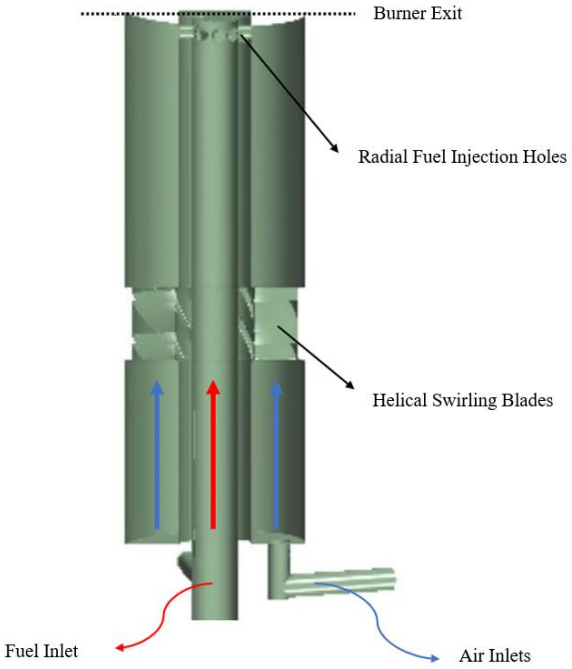

Figure 3.5. Cross section of a 3-D drawing of the experimental swirl burner

3.1.2 Fuel and Air Supply Systems

The experiments were conducted at the Combustion Laboratory of TÜBİTAK-SAGE in Ankara. During the experiments, the air was provided by an air compressor outside the laboratory. Similarly, fuel bottles outside the laboratory fed natural gas and hydrogen into the system. To denote the volumetric hydrogen percent in the fuel, H2VOL% abbreviation will be used in the rest of the thesis. Both air and fuel pipes were connected to mass flow controllers. The targeted mass flow values were provided to the mass flow controllers via a computer connected to the controllers with cables. After mass flow controllers, the air duct was split into four pipes and fed into the swirl burner air inlets. Fuel streams had to be mixed with each other first. Natural gas and hydrogen lines were connected to the in-line static gas mixer. The gas mixer consisted of a 1-inch pipe filled with glass beads. This part ensured the homogeneity of the fuel mixture. The mass flow controller and fuel mixing systems are illustrated in Figures 3.6 and 3.7.

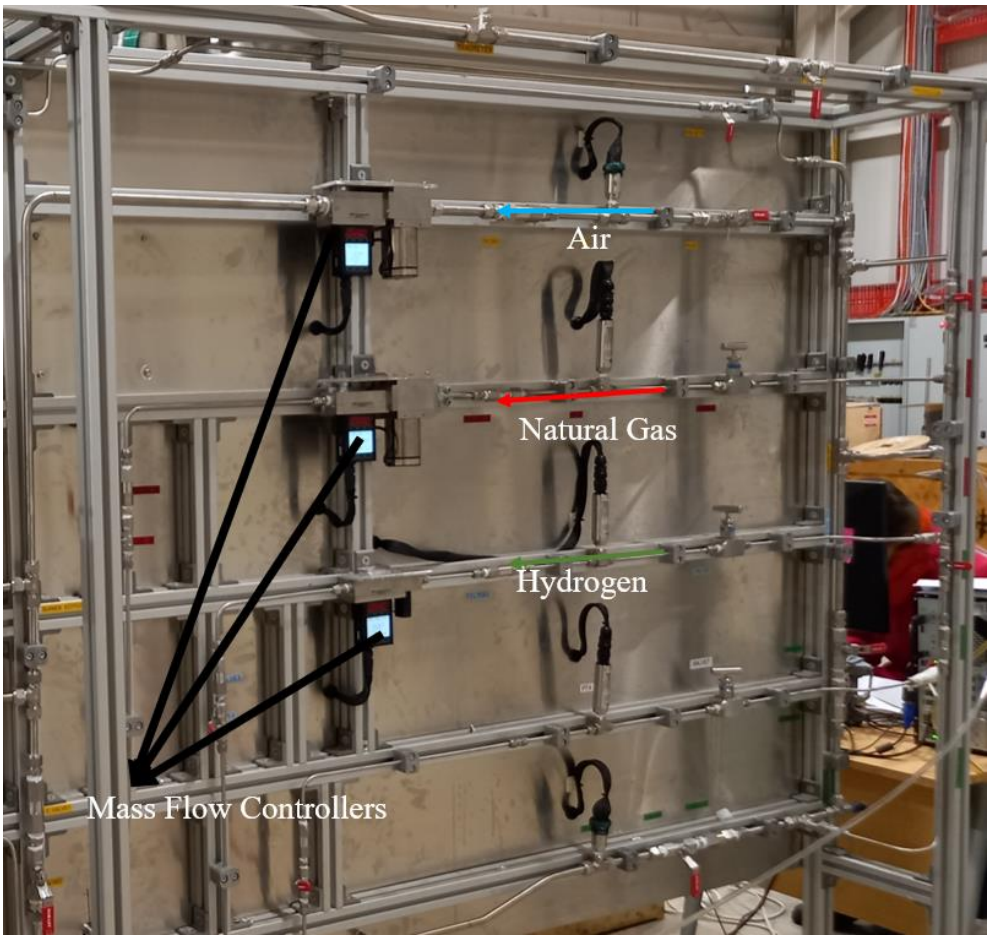

Figure 3.6. Mass flow controllers used in the experiments

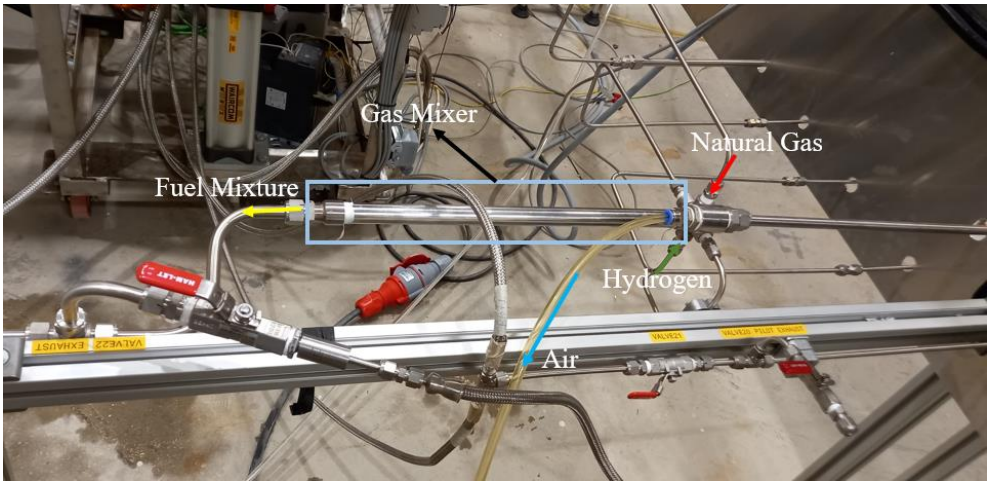

Figure 3.7. Static gas mixer used in the experiments

3.1.3 Chemiluminescence Optical System

For the chemiluminescence experiments, the optical set-up and a HiSense Zyla model camera, both available at TÜBİTAK-SAGE, were used. An image intensifier and a filter for detecting OH* signals were used with the camera. During the image collection, a black background was used to improve flame images. In Figure 3.8, the camera setup is shown oriented toward the experimental burner. The flame chemiluminescence imaging method is described above in section 2.5.2

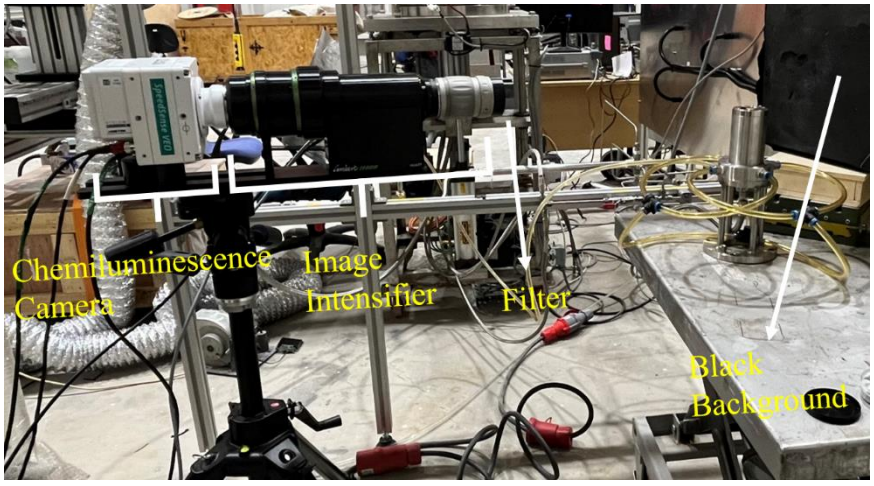

Figure 3.8. Chemiluminescence optical setup

3.1.4 Experimental Procedure

The procedure followed for chemiluminescence experiments is described in this section.

Experimental procedure for chemiluminescence imaging experiments:

1. The chemiluminescence camera and burner position are fixed, camera is turned on and a picture of the burner is taken with a millimeter paper held against it for calibration purposes, using the chemiluminescence camera. This picture is shown in Figure 3.9.

2. Pressures at the inlet side of the mass flow controllers are checked if enough gas pressure exists to supply the burner.
3. The relevant filter is attached to the intensifier.
4. The air and fuel flow rates are slowly increased to the necessary experimental values for the experimental protocol. The experiment starts with only NG and air at 0.8 equivalence ratio.
5. The burner is ignited with a lighter.
6. 1000 images are collected with a 250 μs exposure time, within 1 second interval using the chemiluminescence camera.
7. The hydrogen mass flow rate is increased, and the NG mass flow rate is decreased to keep the volumetric flow rate of the fuel constant.
8. Steps 6 and 7 are repeated until the flame stabilization mode change is observed. After increasing the H2VOL% from 60 to 70, the flame becomes attached to the burner.
9. After the stabilization mode changes, the hydrogen and NG flow rates are immediately set to zero.
10. The air and fuel supply are turned off and the system is purged using nitrogen.

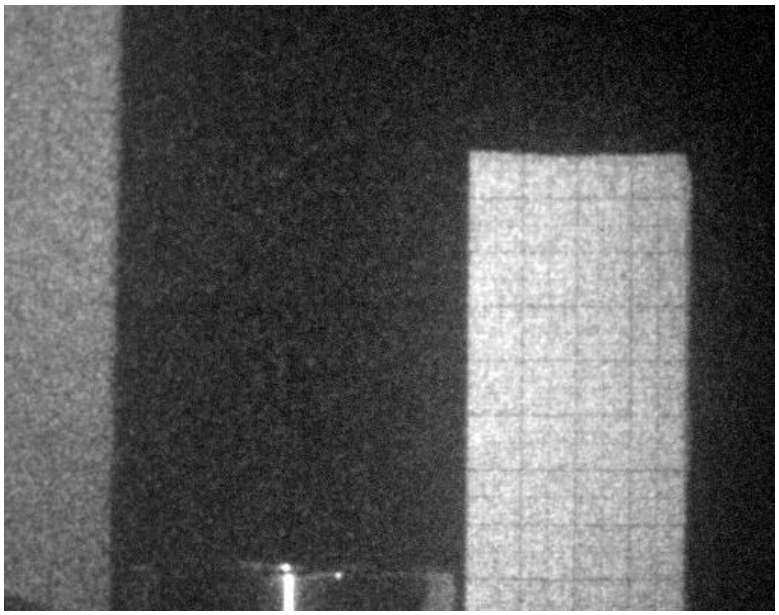

Figure 3.9. Calibration image of the burner taken with the chemiluminescence camera

Throughout the chemiluminescence experiments, the total fuel volumetric flow rate was kept constant by fixing the total SLPM value. In Table 3.1, the air, NG, and hydrogen flow rates used in the experiments are given. The experiments were conducted at 7℃ and atmospheric pressure.

Table 3.1 The air, NG, and hydrogen flow rates used in the experiments (SLPM).

H2VOL% [%]	*Air*	*NG*	*Hydrogen*
0	259.1	21.8	0
2	259.1	21.4	0.4
5	259.1	20.8	1
10	259.1	19.7	2.2
15	259.1	18.6	3.7
20	259.1	17.5	4.4
30	259.1	15.3	6.6
40	259.1	13.1	8.7
50	259.1	11	11
60	259.1	8.7	13.1
70	259.1	6.6	15.3

As seen from the Table 3.1, 11 fuel mixtures were analyzed using chemiluminescence imaging. However, during the 70 H2VOL% experiments, before any images could be collected, the flame changed its stabilization mode and became attached to the central fuel pipe of the burner. Since the burner was not designed to operate with an attached flame, no images were taken for the 70 H2VOL% conditions , and the burner was turned off. In all the fuel mixture conditions, the total fuel flow rate was fixed at 21.8 SLPM, and the air flow was fixed at 259.1 SLPM.

As the total fuel volume rate is kept constant and since a hydrogen molecule needs fewer oxygen molecules to be completely oxidized than a methane molecule, the global equivalence ratio is reduced with increasing H2VOL%. Additionally, since

hydrogen has a lower LHV value per volume when compared to methane, LHV is also reduced when hydrogen is added to the fuel mixture. These effects are shown in Figure 3.10

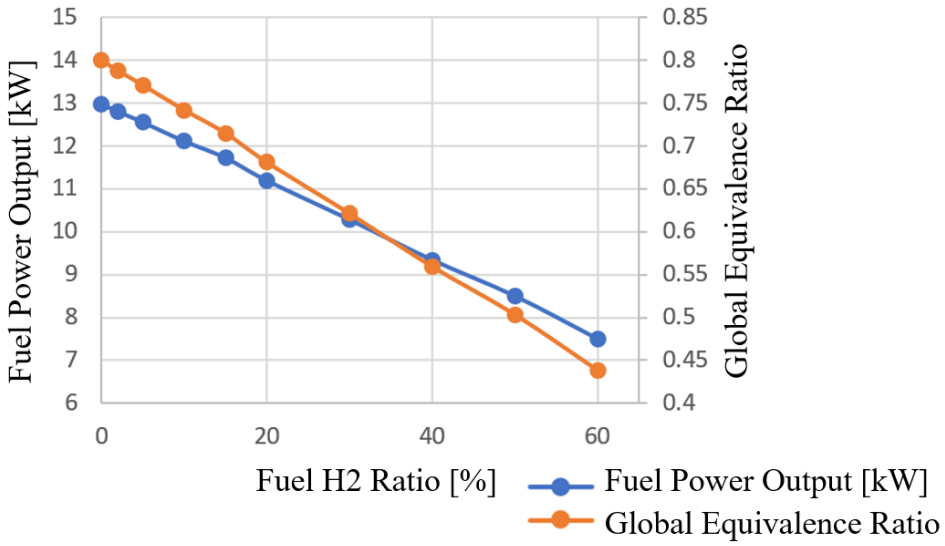

Figure 3.10. Fuel power output (calculated using LHV) and global equivalence ratio plotted against H2VOL%

As seen from Figure 3.10 as the hydrogen is added to the fuel mixture, the power output of the fuel goes down from 14 kW to 6.8 kW. Also, as hydrogen is added to the fuel mixture, the global equivalence ratio goes down from 0.8 to 0.44.

3.2 Determination of Flame Dimensions and Stability Limits from the Experiments

The geometric flame characterization such as dimensions and positions, determination methods are described is detailed.

3.2.1 Image Processing

The images collected from the chemiluminescence measurements are processed using a series of MATLAB scripts. In this section, the steps used for image processing are detailed.

3.2.1.1 Averaging of Chemiluminescence Images

Ten thousand images were captured using the OH* filter for ten fuel mixture conditions (1000 images per flame condition). The captured images were in grayscale and bitmap format. An example of these images is shown in Figure 3.11 with one of the images captured for the flame with 0 H2VOL%. The captured images were 640x400 pixels in size and encoded in 12 bits. The exposure time was 250 μs.

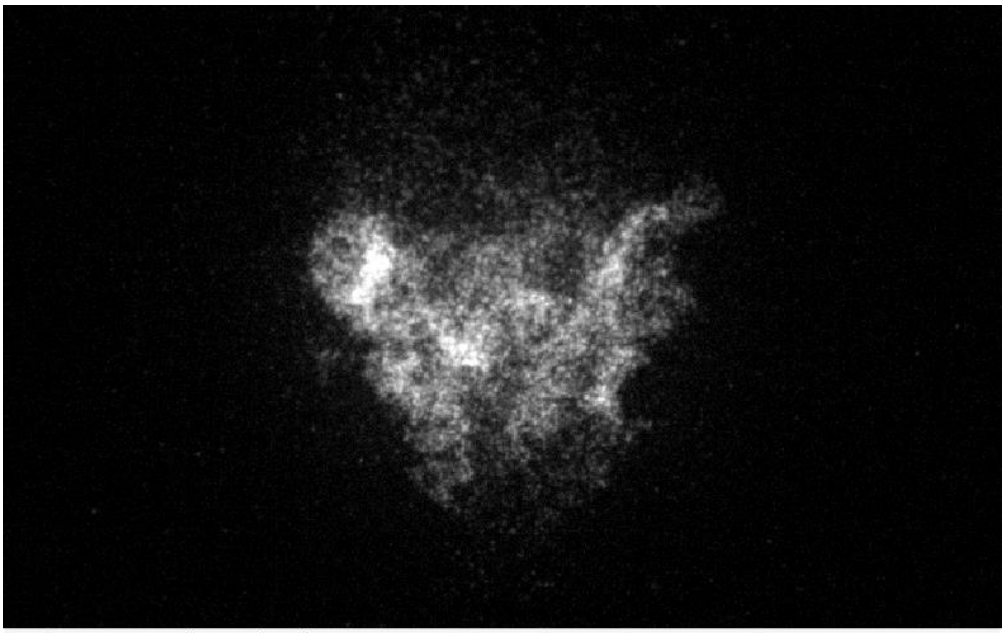

Figure 3.11. A chemiluminescence image captured with an OH* filter for the flame with 0 H2VOL%

These 1000 images were then averaged using a MATLAB script. The resulting image is the mean value of the flame front in a 1-second time interval. The MATLAB script used for averaging a series of images is given in Appendix A. The average image for the 0 H2VOL% condition is given in Figure 3.12.

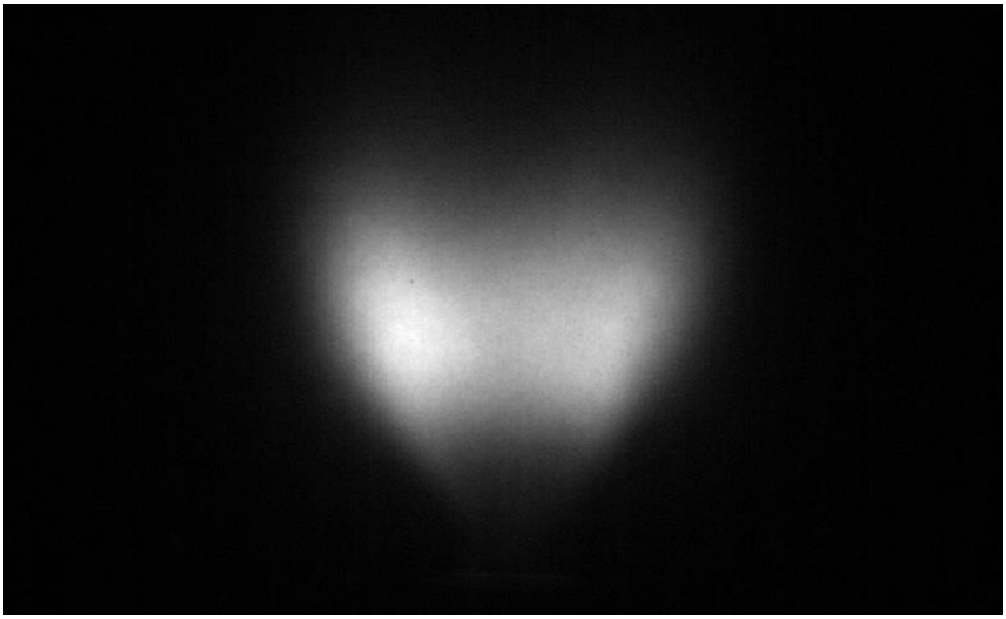

Figure 3.12. Average image of 1000 OH* filtered chemiluminescence instantaneous images for the flame with no hydrogen addition

3.2.1.2 Determination of Flame Dimensions

The average flame images are superimposed onto the calibration image of the burner shown in Figure 3.9. The superimposed image of the calibration picture and the mean chemiluminescence image for the flame with no hydrogen addition is given in Figure 3.13.

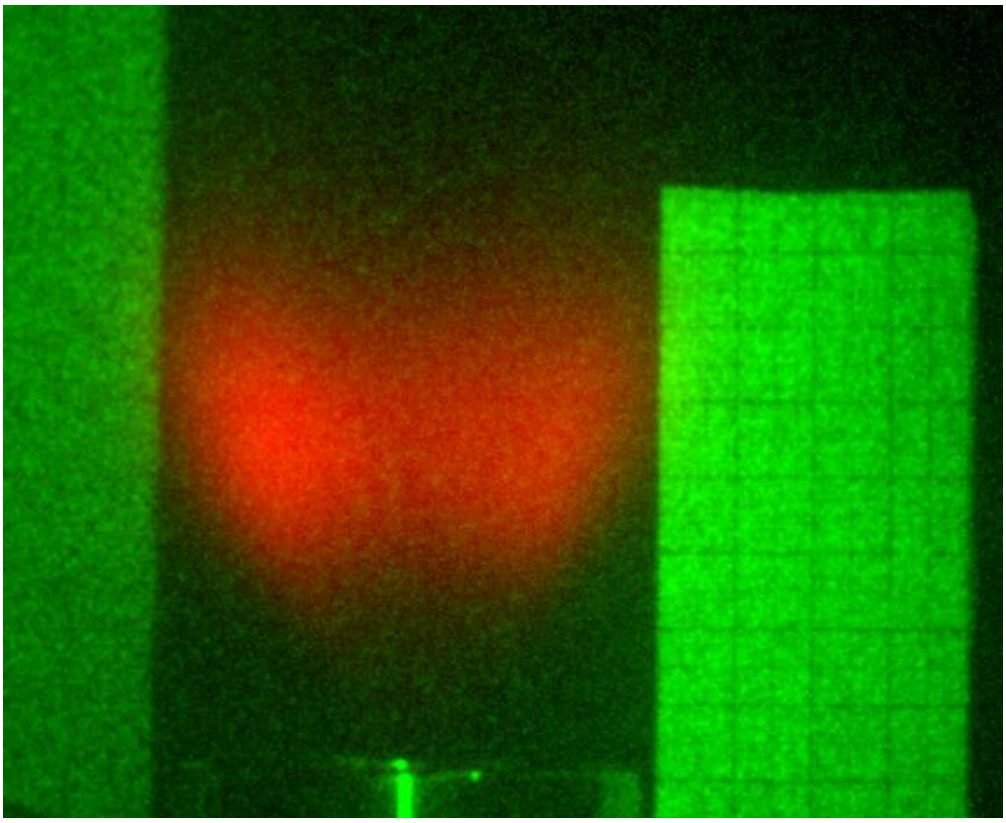

Figure 3.13. Superimposed image of the calibration picture and the mean chemiluminescence image for the flame with no hydrogen addition

The superimposing of two images is done by creating an RGB image, assigning the grayscale image of the calibration photograph to the green matrix of the RGB image, and assigning the average flame image to the red matrix of the RGB image. The MATLAB script used for superimposing two images is given in Appendix B. After gathering the superimposed image, another MATLAB script marks the borders of the mean flame region. This MATLAB script works by locating the pixels where the red intensity is within 0.8% of 40% of the maximum red intensity within the image. The pixel number corresponding to one cm length is given within the same script. This script is given in Appendix C. Then, the uppermost, lowermost, leftmost, and rightmost points of the average flame region borders are determined. Using the coordinates of these points, the flame's width, height, and lift-off height are determined. The final image created for no hydrogen addition is given in Figure 3.14.

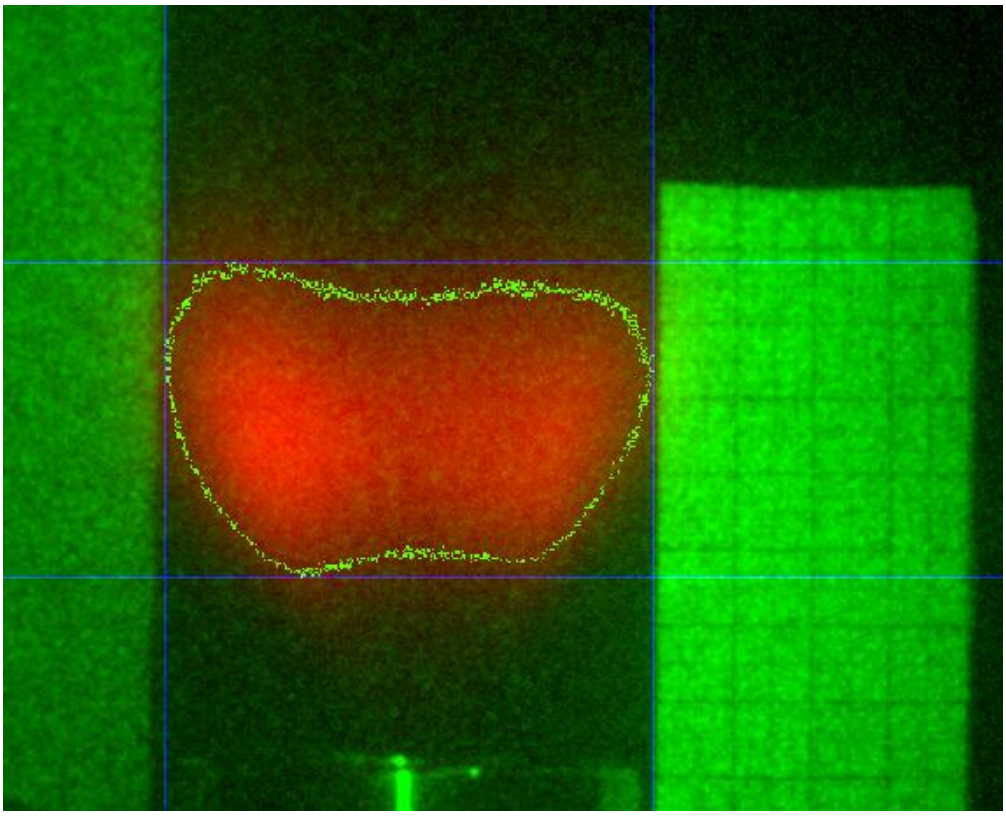

Figure 3.14. Flame region border marked mean flame image for no hydrogen addition

CHAPTER 4

NUMERICAL METHODOLOGY

4.1 Numerical Setup and Domain

In this section, the details of the numerical setup, such as the software and the schemes used, are given, alongside the details of the numerical domain, such as the boundary conditions, and numerical mesh details. Turbulence, combustion, and turbulence chemistry interaction models are detailed in separate sub-sections.

4.1.1 Governing Equations and Numerical Schemes

During the LES simulations, filtered versions of the flow variables are solved. In the equations below, filtered continuity, Navier-Stokes, Energy and Species Transport equations are given. $\bar{.}$ operator denotes the Reynolds filtering operation and the $\tilde{.}$ operator denotes the Favre-filtering operator. The equations are given in tensor form.

- Continuity equation:

$$\frac{\partial \bar{\rho}}{\partial t} + \frac{\partial}{\partial x_i}(\bar{\rho}\tilde{u}_i) = 0 \tag{4.1}$$

- Momentum Equation:

$$\frac{\partial}{\partial t}(\bar{\rho}\tilde{u}_i) + \frac{\partial}{\partial x_j}\left(\bar{\rho}\tilde{u}_i\tilde{u}_j\right) = -\frac{\partial \bar{p}}{\partial x_i} + \frac{\partial}{\partial x_i}\left[\bar{\tau}_{ij} - \bar{\rho}\left(\widetilde{u_i u_j} - \tilde{u}_i\tilde{u}_j\right)\right] + \bar{\rho}g_i \tag{4.2}$$

Where $\bar{\tau}_{ij}$ is the filtered version of the viscous stress tensor τ_{ij}, defined in Eq. 4.3

$$\tau_{ij} = \mu\left(\frac{\partial u_i}{\partial x_j} + \frac{\partial u_i}{\partial x_i}\right) - \frac{2}{3}\mu\frac{\partial u_k}{\partial x_k}\delta_{ij}$$

4.3

- Enthalpy, MF, PV Transport

The FGM tables used in the simulation involve four dimensions which are Favre-filtered PV ($\widetilde{\Upsilon}$), Favre-filtered enthalpy ($\tilde{h}$), Favre-Filtered MF ($\tilde{Z}$), and Favre-filtered MF variance ($\widetilde{Z''}$). Favre-filtered PV variance was not included in the FGM tables since in the literature it is accepted to be not influential in combustion. Additionally, three of these scalars ($\widetilde{\Upsilon}$, $\tilde{h}$ and $\tilde{Z}$) obey to the transport equation given in Eq. 4.4

$$\frac{\partial}{\partial t}\left(\bar{\rho}\widetilde{\Phi}\right) + \frac{\partial}{\partial x_i}\left(\bar{\rho}\tilde{u}_i\widetilde{\Phi}\right) = \frac{\partial}{\partial x_i}\left(\bar{\rho}\widetilde{D}\left(\frac{\partial \Phi}{\partial x_i}\right)\right) + \frac{\partial}{\partial x_i}\bar{\rho}\left(\widetilde{\Phi\tilde{u}_i} - \widetilde{\Phi}\widetilde{u_\iota}\right) + \bar{\rho}\widetilde{\dot{\omega}}_\Phi$$

4.4

Where Φ denotes both MF and PV and h. D denotes diffusivity; it is defined as $\widetilde{D} = \frac{\tilde{\lambda}}{\tilde{c}_p}$, where λ is the mixture conductivity, c_p is the mixture specific heat at constant pressure. For MF and enthalpy transport equations, the term $\bar{\dot{\omega}}_\Phi$ is equal to 0 as without phase change, there is no mass production and the atomic elements are conserved during combustion, and the total enthalpy does not change during combustion as radiation is not modeled. Additionally, Lewis numbers for both enthalpy, PV and MF are assumed to be unity. On the other hand, the source term for the PV is a non-zero variable and is modelled by the TFM. Finally, the Favre-filtered MF variance is modelled using an algebraic model given by Eq. 4.5.

$$\widetilde{Z''} = c_v\Delta^2\left(\left|\nabla\widetilde{\Upsilon}\right|\right)^2$$

4.5

Where the parameter c_v is a model constant.

In the standard FGM model the source term for PV transport equation is calculated using a PDF table. However, since TFM was used to complement the modelling of the PV source term, it was calculated as shown in Eq. 4.6.

$$\bar{\dot{\omega}}_{\mathrm{Y,TFM}} = \frac{E}{F}\bar{\dot{\omega}}_{\mathrm{Y,l}}$$

4.6

Where $\bar{\dot{\omega}}_{\mathrm{Y,TFM}}$ is the mean PV source term modelled by TFM and used in the simulation, $\bar{\dot{\omega}}_{\mathrm{Y,l}}$ is the mean source term of the progress variable provided by the PDF table, E is the efficiency function and F is the thickening factor. The thickening factor F is calculated by the equation given in Eq. 4.7.

$$F = 1 + (F_{max}^{loc} - 1)\Omega$$

4.7

Where Ω is the reaction zone sensor and F_{max}^{loc} is the maximum flame thickening factor at each local numerical cell. F_{max}^{loc} and Ω parameters are defined in Eqs. 4.8 and 4.9 [75].

$$F_{max}^{loc} = \min\left(F_{max}, \mathrm{N}\frac{\Delta}{\delta_L}\right)$$

4.8

Where N is the number of points in the flame front (set to 8 for the simulations), F_{max} is the global maximum flame thickening factor (set to 20), and δ is the laminar flame thickness. The laminar flame thickness value was calculated using the Sutherland law for thermal diffusivity.

$$\Omega = \tanh\left(\beta\frac{\dot{c}}{\dot{c}_{max}}\right)$$

4.9

Where β is a model constant, $\dot{c}$ is the normalized reaction progress rate and $\dot{c}_{max}$ is the maximum normalized progress rate over all the numerical cells. This model for

calculating reaction zone sensor is called the progress variable reaction rate model. Finally, the efficiency function E was modeled using the turbulent flame speed (TFS) model, according to the equation given in Eq. 4.10.

$$E = \alpha \frac{S_t^{\Delta}}{S_L}$$

4.10

Where S_t^{Δ} is the turbulent flame speed at the turbulent length scale of the grid size Δ, S_L^0 is the un-stretched laminar flame speed of the mixture and α is a user constant. Zimont model was used to calculate the term S_t^{Δ} [76].

Unresolved Reynolds stresses $\left(\widetilde{u_i u_j} - \tilde{u}_i \tilde{u}_j\right)$ are modelled by the SGS model in addition to the Unresolved MF, PV, and enthalpy fluxes.

- WALE SGS Model [77]:

Unresolved Reynolds stresses are modelled by the WALE SGS model. In the WALE SGS model, the unresolved stresses are modelled using the generic eddy-viscosity form, which is given in Eq. 4.11.

$$R_{ij} = \bar{\rho}\left(\widetilde{u_i u_j} - \tilde{u}_i \tilde{u}_j\right) = -2\mu_{sgs}\tilde{S^D}_{ij} + \frac{2}{3}\bar{\rho}k\delta_{ij}$$

4.11

Where μ_{sgs} is the SGS viscosity and k is the SGS kinetic energy. The SGS viscosity μ_{sgs} must be modelled by the WALE model as defined in Eq. 4.12

$$\mu_{sgs} = C_m \Delta^2 \overline{OP}(x_i, t)$$

4.12

Where Δ is the cut-off length scale and is modelled as:

$$\Delta = V^{\frac{1}{3}}$$

4.13

In the WALE model, the operator $\overline{OP}$ is constructed to consider both rotation and strain of the velocity field. Additionally, this model improves the Smagorinsky model by insuring that μ_{sgs} goes to 0 as the flow gets near to a wall. This is more physically accurate compared to the Smagorinsky model. Finally, the ideal gas model was used to model the density.

The following numerical schemes were used in the CFD simulations.

- Segregated Flow Solver:

The segregated flow solver sequentially solves the conservation equations of mass and momentum. It handles the non-linear governing equations by iteratively solving them one by one for the solution variables like u, v, w, and p [78]. The PISO pressure-velocity coupling algorithm was used in the simulations along with the segregated solver. The segregated solver uses the PISO algorithm to obtain a velocity field solution that fulfills the mass conservation condition [79].

- Segregated Fluid Enthalpy Solver:

Segregated fluid enthalpy solver solves the total energy equation where chemical thermal enthalpy is the solved variable. The temperature is then computed from the enthalpy using the equation of state [78].

4.1.2 Geometry and Boundary Conditions

Since the design and manufacturing of the experimental burner were done in-house, the geometry details were fully available for use in numerical simulations. Swirling blades, air duct, and central fuel pipe geometry were fully modeled in the numerical geometry. Since the burner was open to the atmosphere, the numerical burner geometry was enclosed in a large cylinder and the cylinder walls were assigned the pressure outlet boundary condition. By doing this, the air flow is free to enter from the side walls and bottom of the cylinder, mimicking the stagnant air in the laboratory. The same CAD files used in manufacturing the swirler blades using SLM

were used to model the swirler blades, making the modeled swirler shape as similar as possible to the manufactured one. The four air inlets were not added to the geometry to reduce complexity and ease the meshing process. The rest of the dimensions and features were kept similar to the experimental combustor. The numerical geometry is detailed in Figure 4.1.

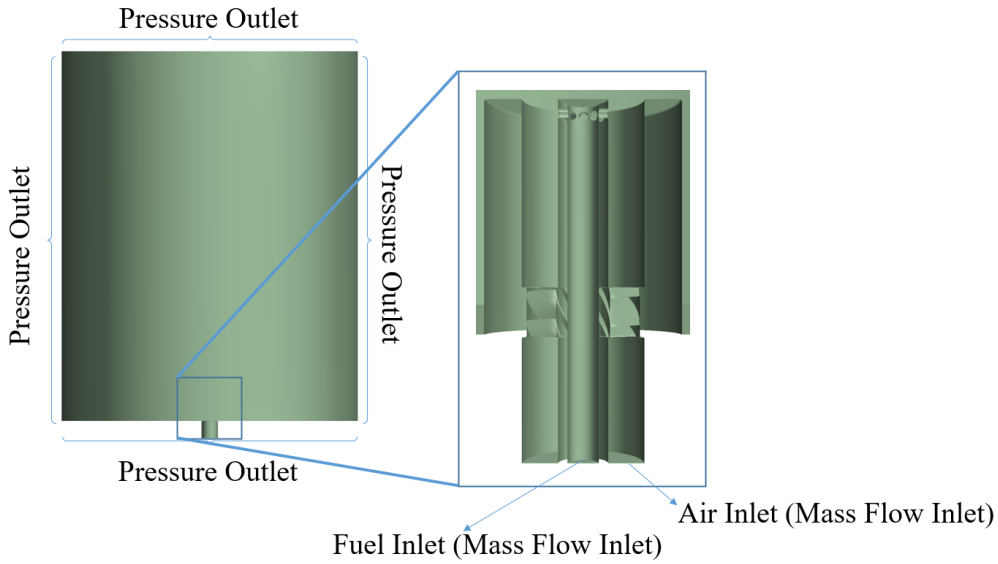

Figure 4.1. Numerical burner geometry

As seen in Figure 4.1, mass flow inlet conditions were assigned for the air and fuel inlet surfaces. The different mass flow rates for the different fuel conditions are given in Table 4.1.

Table 4.1 Mass Flow Rates (MFR) of NG, hydrogen, and air, used in numerical simulations for different fuel mixtures.

Fuel Condition [H2VOL%]	*Air MFR [kg/s]*	*NG MFR [kg/s]*	*Hydrogen MFR [kg/s]*
0	$5.58 * 10^{-3}$	$2.87 * 10^{-4}$	0
30	$5.58 * 10^{-3}$	$2 * 10^{-4}$	$9.7 * 10^{-6}$
60	$5.58 * 10^{-3}$	$1.1 * 10^{-4}$	$1.9 * 10^{-5}$
70	$5.58 * 10^{-3}$	$8.6 * 10^{-5}$	$2.3 * 10^{-5}$

The mass flow rates were calculated using a smath sheet. This sheet is given in Appendix D. Finally, the composition of the natural gas used in the experiments was modeled to achieve high accuracy in combustion simulations. In his thesis work, Berk Kıymaz analyzed the composition of the natural gas used in the experiments for both this and his thesis [80]. The resulting composition data of the natural gas is given in Table 4.2.

Table 4.2 Composition of the NG used in the experiments [80].

Species Name	*Molar Fraction (%)*
CH_4	88.75
C_2H_4	9.65
C_3H_6	1.60

The resulting mass fractions within the fuel were again calculated using the smath sheet given in Appendix D. After the simulations were conducted, the volumetric flow rates of the fuel in the numerical simulations were checked and validated to be correct. Only the fluid part of the domain was modeled for 0 and 30 H2VOL%. However, since the wall temperature profile was a significant factor in the flame attachment phenomenon, 60 and 70 H2VOL% simulations were performed with solid domains included. The temperature fields of these solid domains were modeled using the conjugate heat transfer (CHT) model. This was done to reduce the overall computational cost of the thesis work. The numerical domains used in simulations not involving CHT and involving CHT are given in Figure 4.2.

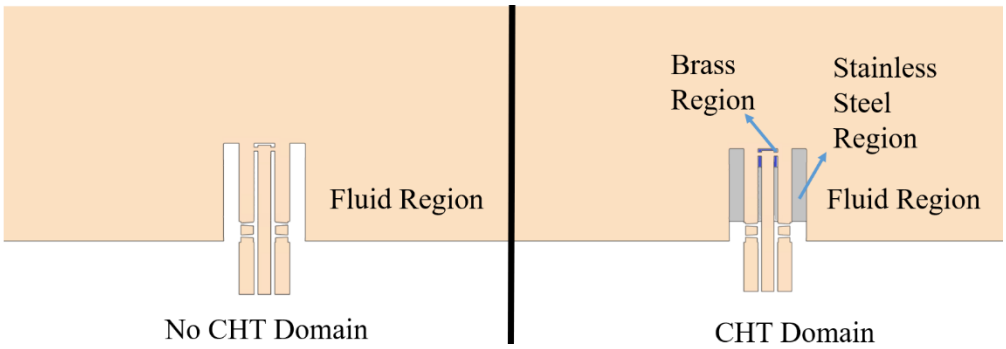

Figure 4.2. CHT and no CHT domains illustrated

4.1.3 Numerical Setup and Procedure

The 22.06 version of StarCCM+ software was used for meshing and CFD simulations. The simulations were conducted on the high-powered computer (HPC) belonging to TRMOTOR Power Systems A.Ş. This HPC system hosts around 4000 cores; a single fuel condition run for the thesis was executed using mostly around 1000 cores. The HPC system works with the OpenSUSE Linux Operating system. Three different continua were created to simulate stainless steel, brass, and fluid volumes. The models used in the fluid continuum are listed in Table 4.3.

Table 4.3 Models used in the fluid continuum.

Model Name
Large Eddy Simulation
WALE Subgrid Model
Flamelet Generated Manifold
Thickened Flame Model
Ideal Gas

As seen in Table 4.3, the ideal gas model is selected for state equation modeling. Additionally, gravity is turned on for the simulation and turbulent and reacting flow options are selected. For reaction models, the flamelet option and FGM model are selected. LES and wall adapting large eddy (WALE) models are selected for turbulence modeling. Finally, to model the turbulence-chemistry interactions, TFM was selected. The reasoning behind these model selections is given in the following sections.

The models used in the solid continua are given in Table 4.4.

Table 4.4 Models used in the solid continua.

Model Names
Constant Density
Implicit Unsteady
Segregated Solid Energy

These models were chosen to simulate the solid walls temperatures using a constant specific heat value. During the experiments, the metal parts of the burner took minutes to reach their steady-state temperature. Since the physical time durations of the simulations were always lower than a second, a work round was needed to make the metal parts reach steady state temperature. The specific heat values of the metal parts were lowered to around a hundredth of their physical values to achieve this requirement. The metal conductivities were kept at measured values for brass and stainless steel [81]. By doing this, the time needed for the metal parts to reach steady-state temperature was drastically reduced, but the steady-state temperature profile was not altered. This method is mentioned in the literature as accurate for steady-state temperature predictions but is said to be not accurate for temperature fluctuations occurring in the metal parts [82].

Furthermore, the flow-over time value was used to determine the physical time limit for the simulations. The average mean gas velocity at the burner exit was determined

to calculate the flow-over time. Then the relevant distance from the burner exit was divided by the average mean velocity value. With this method, the flow-over time was determined to be $2.795 * 10^{-2}$ s. Accordingly, all simulations were run for at least three flow-over times to stabilize and another three flow-over times to get the mean values. A time step of $10^{-5}\ s$ was selected.

Finally, the following procedure was carried out to obtain the numerical results for different fuel mixture conditions.

1. Simulations are conducted for more than three flow-over times with no hydrogen addition to reach a stabilized cold flow and homogeneous dispersion of the fuel in the recirculation zone.
2. Then the mixture is ignited and computed further to obtain a stabilized flame.
3. After flame stabilization, the computations are further conducted to collect the average values.
4. After the average values are collected, the fuel composition is changed to the next one with more H2VOL%.
5. Again, the computations are conducted further for flame stabilization.
6. The computations are continued to gather new average values.
7. Steps 4, 5 and 6 are repeated for the new fuel condition.
8. If the new fuel condition results in the flame becoming attached to the burner, the process of stability change is observed, and the simulation is ended.

0, 30, 60, and 70 H2VOL% were simulated numerically following the procedure described.

4.1.4 Meshing System

The numerical domain was meshed using StarCCM+ 22.06 software. The resulting mesh consisted of ~34 million polyhedral numerical cells. The polyhedral auto-mesher was used to conduct the meshing of the domain. The main parameters used for the polyhedral mesh system are given in Table 4.5.

Table 4.5 Parameters used in polyhedral meshing.

Parameter Name	*Parameter Value*
Minimum Surface Size	0.05 mm
Surface Growth Rate	1.3
Volume Growth Rate	1.05

Several "bodies of influence" were used to obtain the required mesh size distribution. The parameters used for the numerical cells within these bodies of influence are given in Table 4.5. These bodies of influence were placed at the swirler region, where the flame was expected to stabilize, the region where fuel is injected into the air duct, and the part of the air duct downstream of the swirler blades. These bodies of influence are illustrated in Figure 4.3.

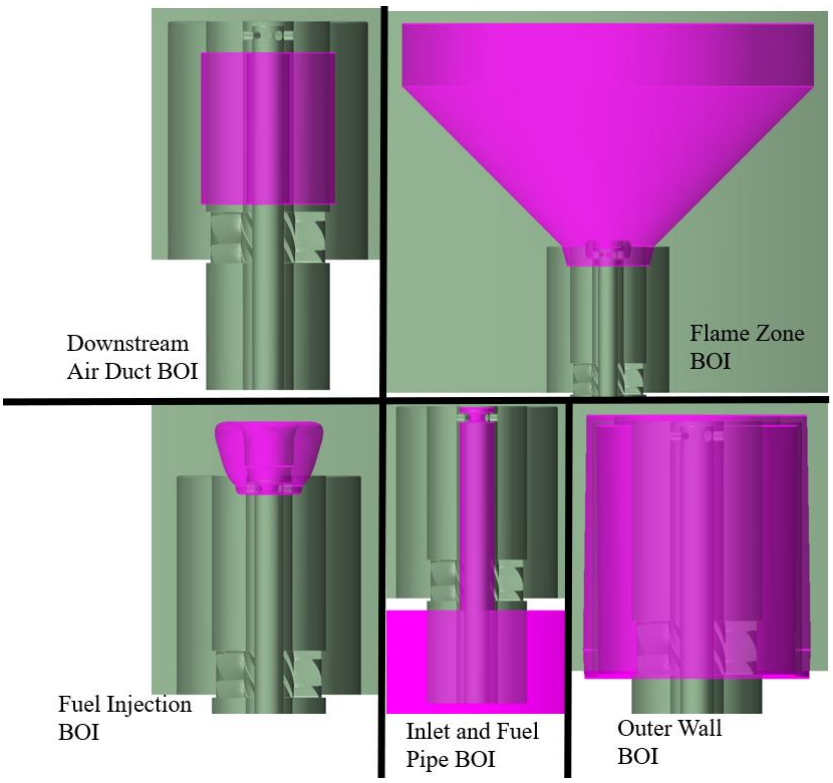

Figure 4.3. Bodies of influence used in meshing the numerical domain

The smallest numerical cells have been placed inside the swirler and the fuel injection region since the smallest turbulent eddies are expected to be inside the swirler region. To predict the attachment of the flame and mixing of fuel and air flows, the numerical cell size inside the fuel injection region is essential. The air duct region lying downstream of the swirler, and the flame region is also very important to accurately predict the flame stability, position, and dimensions and to model the effect of eddies originating from the swirler and advecting downstream to the flame. Finally, a surface sizing was used at the outlet section to prevent numerical instability stemming from backflow. The resulting mesh is shown in Figures 4.4 and 4.5.

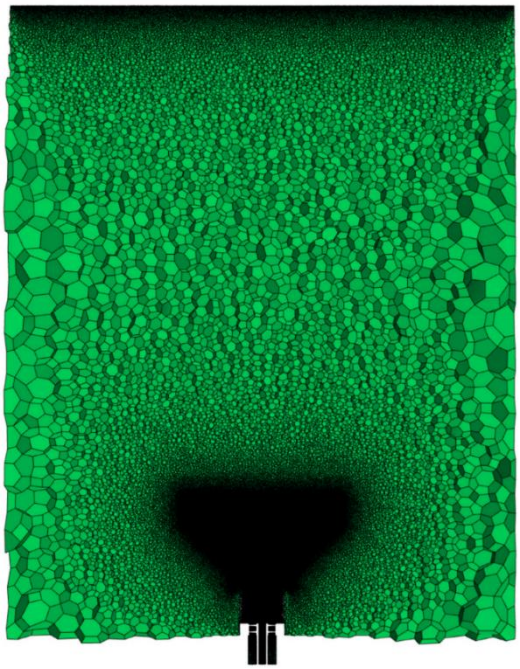

Figure 4.4. Axial slice of the numerical mesh used in the CFD simulations

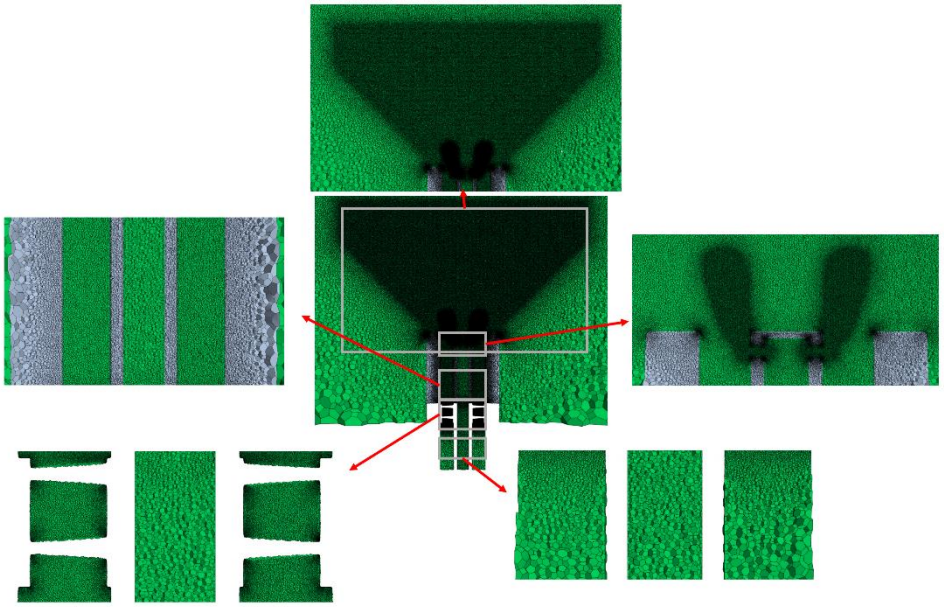

Figure 4.5. The axial slice of the numerical mesh used in the CFD simulations zoomed into relevant regions

In Figure 4.5, the meshes lying in the fluid region were colored green, and the meshes lying in the solid region were colored grey. Solid region meshes were only used in the computations of 60 and 70 H2VOL%.

A non-reactive simulation was conducted over three flow-over times to validate the resulting mesh. The results were analyzed to confirm that in most of the domain relevant to the flame, more than 80% of the turbulent kinetic energy was resolved [83]. The turbulence resolution ratio contour of the domain is illustrated in Figure 4.6. Additionally, the numerical cells with a turbulence resolution ratio lower than 80% are illustrated in Figure 4.7.

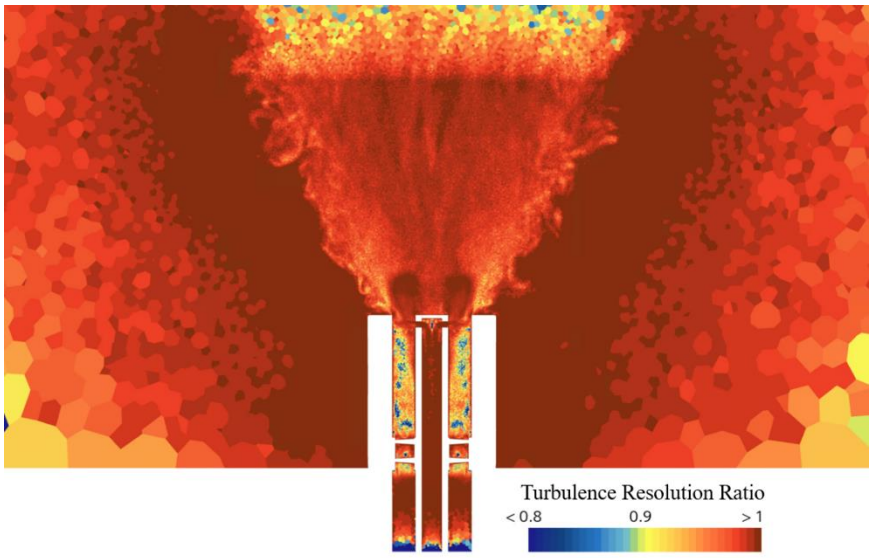

Figure 4.6. Turbulence resolution ratio contours on an axial slice

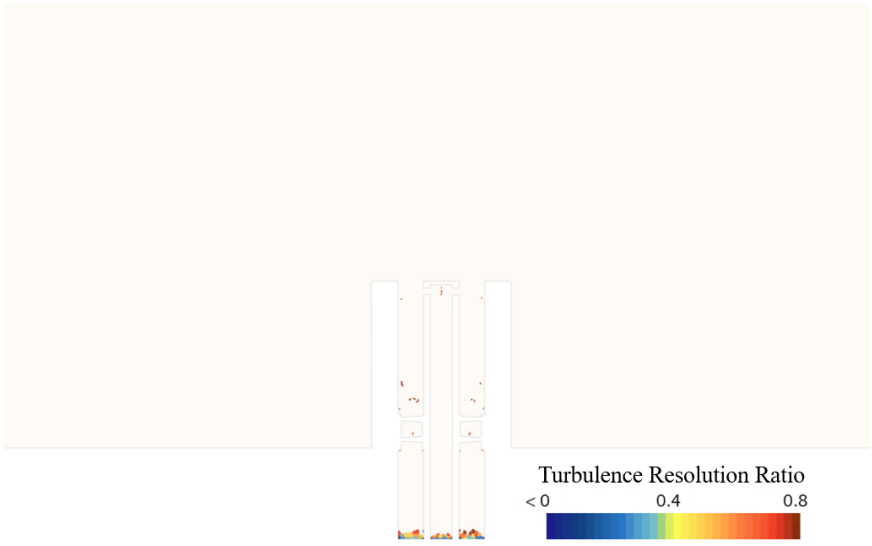

Figure 4.7. Numerical cells with lower than 80% of turbulence resolution illustrated on an axial slice

Finally, the convective courant number was evaluated for the time step of 1e-5 and was confirmed to be lower than 5 in most of the numerical domain. The convective Courant number field is illustrated in Figure 4.8.

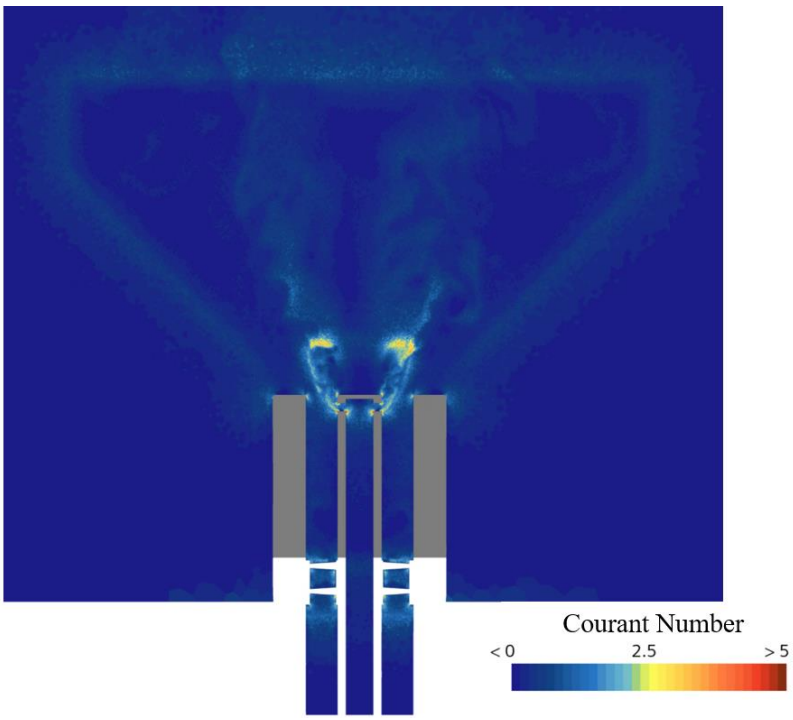

Figure 4.8. Convective Courant number field on an axial slice

4.2 Turbulence Modelling

In the simulations, the LES approach was used for turbulence modeling. This was done for two reasons. One is the shortcomings of RANS simulations in high-curvature flows such as swirled flows. The other reason is that the phenomenon of flame stabilization mode-change from a lifted-off flame to an attached one is inherently unstable, so simulating the phenomenon with a RANS model was considered unfeasible.

4.3 Combustion Modelling

FGM for combustion modeling is chosen to keep the computational costs low while simulating the effects of chemistry as accurately as possible. Computational costs were already high since LES was chosen for the turbulence model, and around 34 million numerical cells were used for the simulations. Adding a finite rate chemistry combustion model was unfeasible for an already such expensive simulation. Moreover, since the FGM model was shown to be accurate for very similar burners with similar fuel conditions [72, 84], it was chosen as the combustion model. GRI3.0 mechanism was used to generate the FGM tables.

4.4 Turbulence-Combustion Interaction Modelling

Early numerical simulations conducted for the thesis work using only the FGM model for turbulence-chemistry interaction showed that it could not reproduce the phenomenon of flame attachment to the burner. A more complex turbulence chemistry interaction model was utilized to overcome this situation. This model was TFM. However, for TFM to work, the model needed the laminar flame speed values for the possible mixture fractions in the domain. Thus, the FGM tabulation reactor model was switched from a 0-D reactor to a 1-D freely propagating reactor. When using this type of reactor, the resulting tables included the laminar flame speed for the possible mixture fraction, heat loss, mixture fraction variance, and progress variable pairs. This laminar flame speed table was fed to the TFM to model the turbulence-flame interaction. This resulted in the simulations being able to predict a stabilization mode change from lifted-off flames to an attached one.

4.5 Post Processing

The “chemical heat release rate (CHRR)” variable was used to assess the flame front. This variable corresponds to the heat release rate happening due to chemical

reactions and has the dimensions of $\frac{J}{m^3 * s}$. The time mean of the CHRR variable was collected throughout the numerical simulations. Additionally, to observe the flames' dynamics, CHRR data was volumetrically rendered, and two images were taken of the volume render of CHRR data every 10^{-3} seconds from a top-down direction and a radial direction. Another user variable was created for the dynamic behavior images to make the flame more visible. This variable was formatted to be unity everywhere in the domain where the CHRR value was higher than 40% of the maximum of the mean CHRR field and 0 everywhere else. A threshold volume of the resulting mean CHRR field was created, including numerical cells with a higher CHRR value than 40% of the maximum value of the mean CHRR field. The lower, upper, rightmost, and leftmost points were then used to gauge the flame position and dimensions. These mean and instantaneous CHRR field volumetric renders are shown in the figures in the following sections. Additionally, the plane section contours of the CHRR variable field were used to analyze the flame further. By using the line-of-sight images of volumetric renderings of numerical results, it is possible to compare them with the line-of-sight results collected from the experiments. Thus no inverse Abell transform was applied to the images.

CHAPTER 5

RESULTS AND DISCUSSION

5.1 Experimental Results

In this section, the results of the experiments conducted for this thesis are presented. The results include the effects of hydrogen addition on the stabilization modes and on the dimensions and positions of the flame. These results are illustrated using pictures taken with conventional cameras and images collected using chemiluminescence cameras.

5.1.1 Effect of Hydrogen on Flame Stabilization Modes

Throughout the experiments, the flame stabilized on the experimental burner mostly showed a lifted-off nature. In Figure 5.1, the flame with no hydrogen addition is shown. It is observed that the stabilized flame is a lifted-off one. However, as the hydrogen addition to the fuel mixture was increased, the flame started to get closer and closer to the burner exit. As the H2VOL% is increased, some parts of the flame propagate downstream towards the fuel injector holes. These effects are shown in Figure 5.2, where the flame with 60 H2VOL% is pictured. After switching to 70 H2VOL%, the flame reaches the fuel injector holes and attaches to the burner central fuel pipe walls. This change happens rapidly. This type of attached flame occurring at 70 H2VOL% is shown in Figure 5.3.

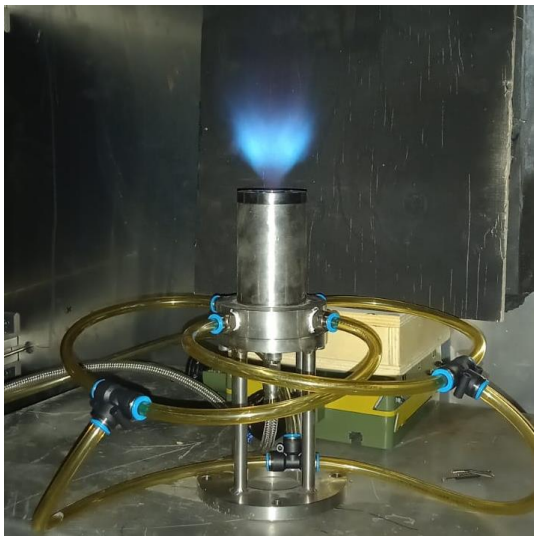

Figure 5.1. A picture of the lifted-off flame for no hydrogen addition

Figure 5.2. A picture of the lifted-off flame at 60 H2VOL%

Figure 5.3. A picture of the attached flame at 70 H2VOL%

Furthermore, it is worth noting that for all the lifted flame cases for 0 to 60 H2VOL%, the global structure and color of the flame indicate a good mixing of fuel and air. This is deducted from the blue color and low luminosity of the flame. In contrast, the attached flame at 70 H2VOL% condition displays a blue color close to the attachment region, but brighter color zones downstream indicate some strong changes in the mixing intensity and the flame structure. Finally, in Figure 5.4, the images of flames for 0 to 60 H2VOL% are shown.

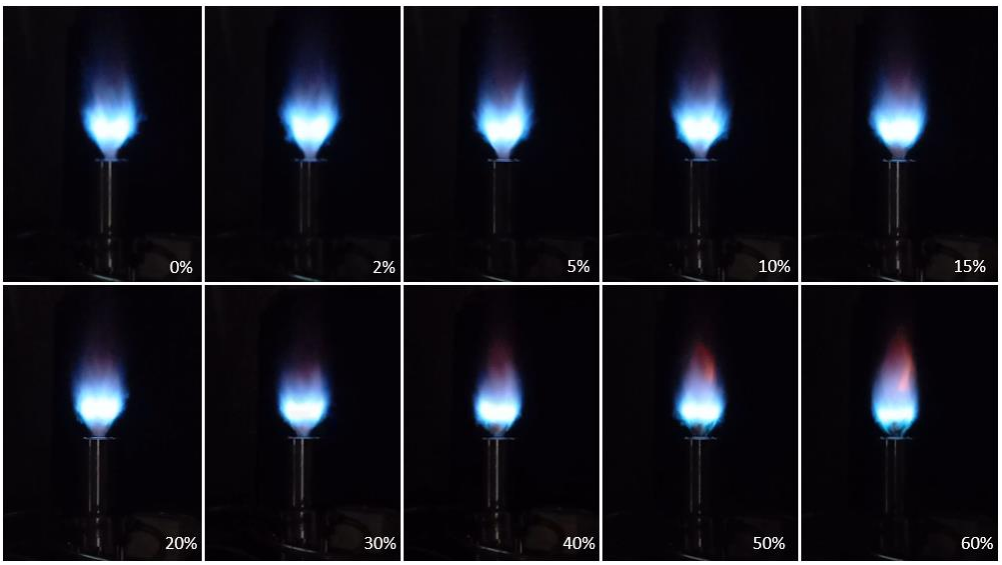

Figure 5.4. Images of flames for 0 to 60 H2VOL%

5.1.2 Effect of Hydrogen Addition on the Flame Position and Dimensions

The effect of hydrogen addition on the flame position and dimensions is analyzed using three parameters. These are flame lift-off height, flame width, and flame length. These parameters are determined for ten fuel conditions between 0 and 60 H2VOL%, using the determination methods shown in section 3.2. These results are plotted in Figure 5.5.

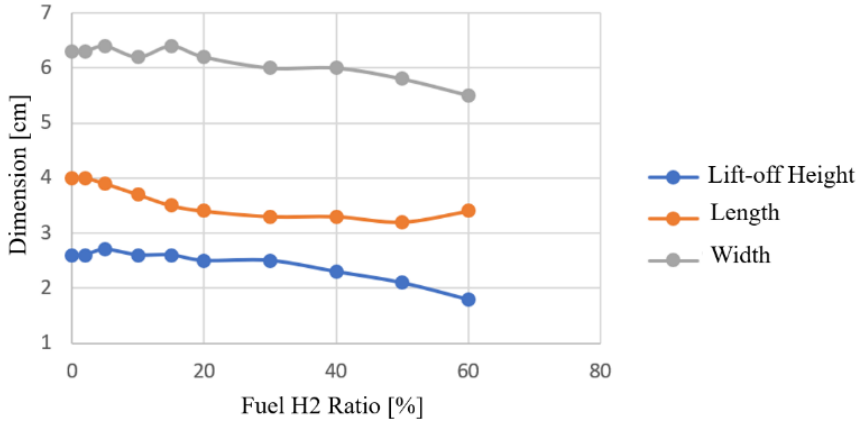

Figure 5.5. Flame dimensional and positional parameters plotted against the H2VOL%

As seen in Figure 5.5, different flame parameters respond differently to the addition of hydrogen to the fuel mixture. While the lift-off height and width of the flame are not affected drastically by the hydrogen addition up to 40 H2VOL% , the length of the flame is mainly affected up to 20 H2VOL%. After which, the flame length is not substantially affected. However, all flame dimensions are getting smaller between pure NG and 60 H2VOL%. This effect can be attributed to increasing flame speeds. When hydrogen is added to the fuel and the flame speed is increased, the same amount of fuel flow can be burned within less distance (and time) compared to the pure NG flame. Additionally, decreasing the global equivalence ratio can contribute to this effect. This shrinking and lowering effect is illustrated in Figure 5.6, where mean chemiluminescence images of flames with 0 and 60 H2VOL% cases are compared side-by-side.

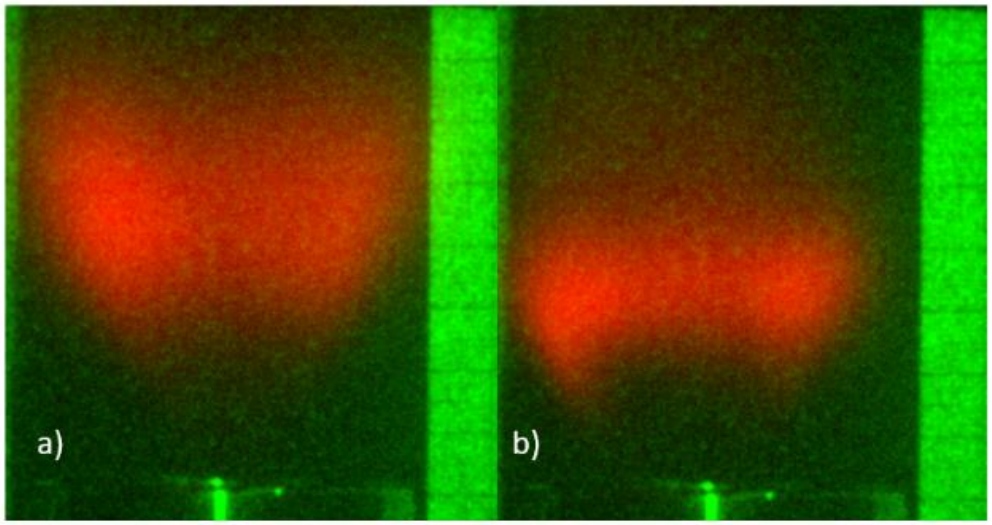

Figure 5.6. Experimental average chemiluminescence OH* concentration images (a) no hydrogen addition (b) for 60 H2VOL%

To demonstrate the gradual nature of these changes for all ten fuel condition cases, experimental results are illustrated using average chemiluminescence images in Figure 5.7,

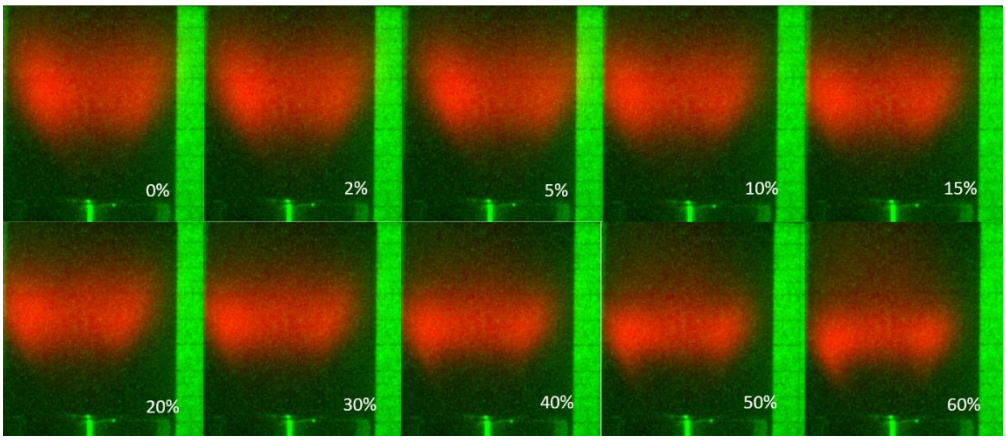

Figure 5.7. Experimental mean chemiluminescence OH* concentration images for 10 fuel conditions from 0 to 60 H2VOL%

As seen in Figure 5.7, the addition of hydrogen gradually shrinks the flame. However, the effect of hydrogen on the flame lift-off height becomes more substantial after the 40 H2VOL%. After this limit, the flame starts to approach the fuel injectors with some individual flame protrusions and at 70 H2VOL%, the flame fully envelopes the fuel injection section as in Figure 5.3.

5.2 Numerical Results

In this section, the results of the numerical simulations of the experimental burner stabilized flames are presented. Numerical simulations were conducted for a total of four fuel conditions. These conditions are 0, 30, 60, and 70 H2VOL%. These numerical results are presented in the following sections. Similar to the experimental results, these sections include the effects of hydrogen addition on flame stability, position, and dimensions. Another section is added to analyze the effects of hydrogen addition on the characteristics of fuel jets and swirling air flow interactions. Additional sections analyze the wall temperature and flow within the swirler and the air duct. Finally, using the numerical simulations, the dynamics of the flame stabilization mode change is analyzed.

5.2.1 Swirl Number, Swirler Air Flow and Annular Duct Air Flow

The swirler blades used in the experiments and numerical simulations were designed to produce a 1.4 swirl number flow. However, the correlation used in determining the swirler blade dimensions is only a prediction that uses some of the dimensions of the swirler blades. The mean velocity field results of the non-reactive LES simulations were therefore used to determine the actual swirl number of the flow downstream of the swirler blades. Since the swirl number is defined as the ratio of the tangential momentum to the axial momentum, the tangential velocity field had to be calculated first. To achieve this, a vector field pointing in the right-handed tangential direction with unity magnitude was defined. This field is illustrated on a radial section of the air duct in Figure 5.8.

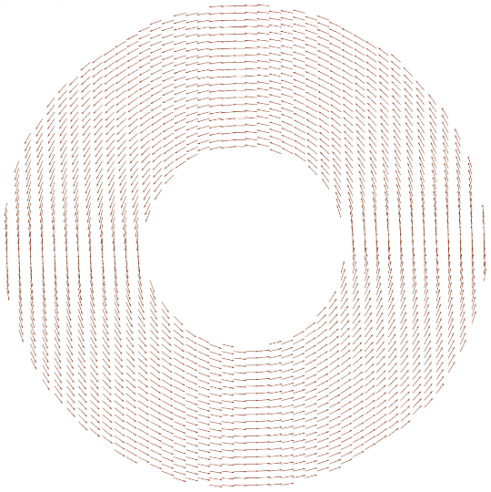

Figure 5.8. The tangential vector field used to determine tangential velocity field illustrated on a radial section of the air duct.

After the definition of the tangential vector field, the tangential velocity field was created by taking the dot product of the tangential vector field and the mean velocity vector field. The resulting scalar field was multiplied by the density to obtain the tangential momentum field. The resulting scalar tangential momentum field is illustrated in Figure 5.10, using four sections of the air duct at different distances from the swirler blades. The positions of these sections are illustrated in Figure 5.9.

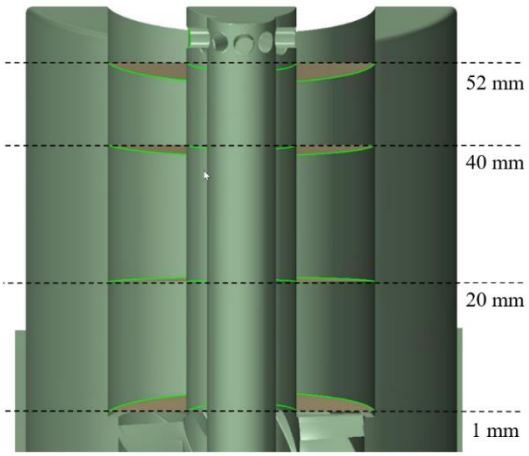

Figure 5.9. Air duct section planes illustrated with their distances to the top of the swirler blades

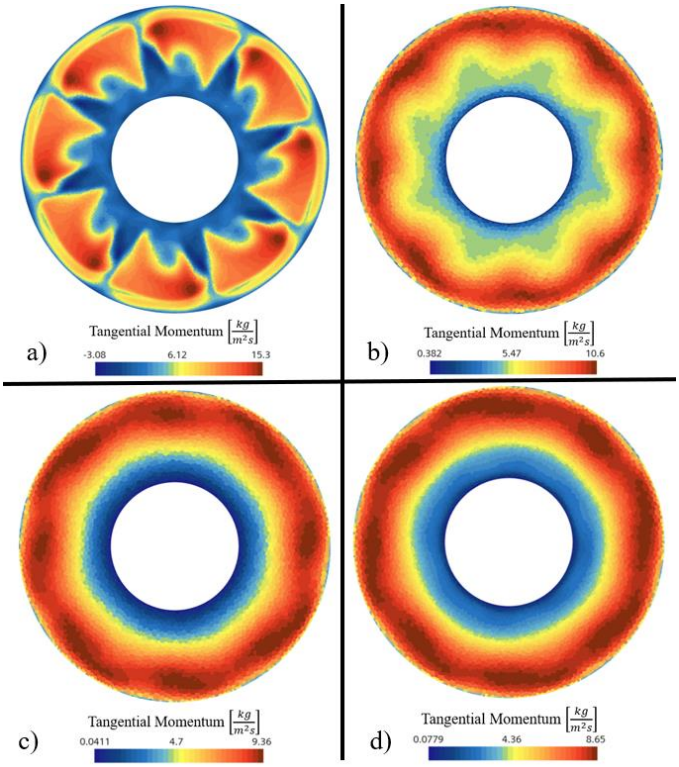

Figure 5.10. Mean tangential momentum contours on a radial section (a) 1 mm (b) 20 mm (c) 40 mm (d) 52 mm downstream from the top of the swirler blades

As observed from Figure 5.10, the tangential velocity field starts with high gradients at 1 mm away from the swirler blades but diffuses out as flow travels downstream in the air duct. The same trend can also be seen in the axial momentum field. The axial momentum field was defined using the y-direction component of the mean velocity vector field and the density field. The axial velocity field is illustrated in Figure 5.11 using the same four sections on the air duct, illustrated in Figure 5.9.

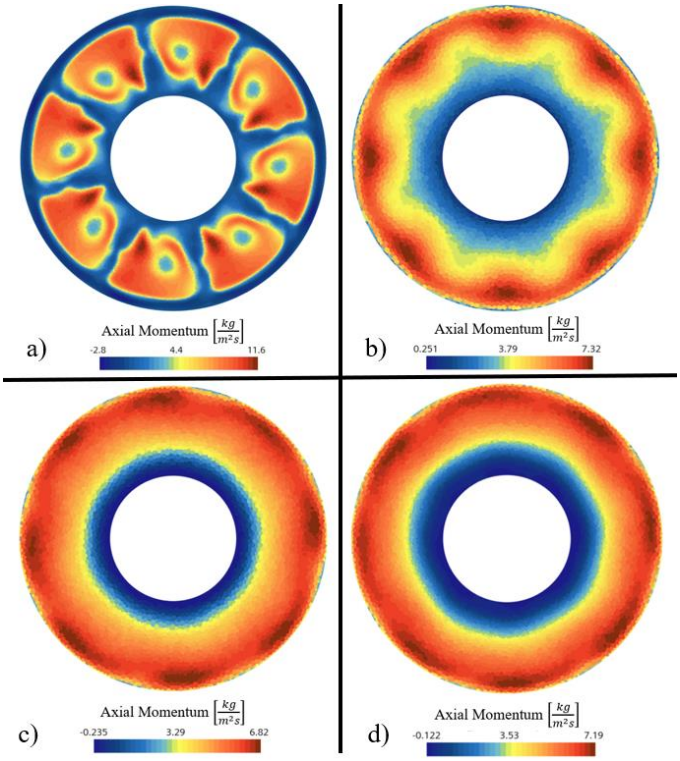

Figure 5.11. Axial momentum contours on a radial section (a) 1 mm (b) 20 mm (c) (40 mm (d) 52 mm downstream from the top of the swirler blades

As seen in Figure 5.11 like the tangential flow field, the axial flow starts with a high gradient section and disperses out as the flow travels downstream in the air duct. Additionally, looking at both tangential and axial flow fields, it is observed that close to the outer wall, a higher velocity flow field exists. This is expected since, in rotating flows, high-velocity fluid elements migrate towards the outer walls where higher centrifugal forces exist.

Using the axial and tangential momentum fields, the swirl number in the four radial sections of the air duct was then determined. Firstly, the surface integrals of tangential and axial momentum were calculated. Then the tangential momentum surface integrals were divided by the axial momentum surface integrals for every radial section since the swirl number definition is tangential momentum divided by the axial momentum. The results are plotted in Figure 5.12.

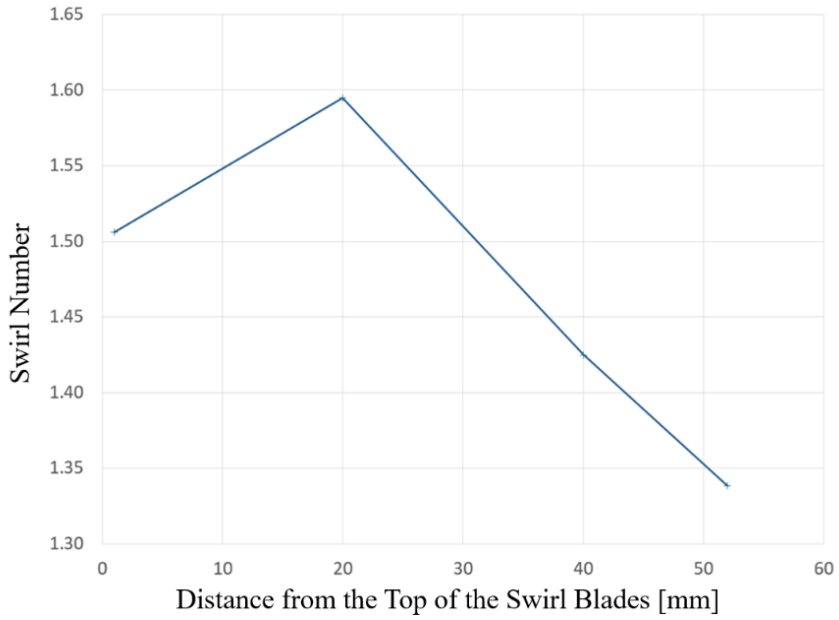

Figure 5.12. Swirl number vs distance from the swirler blades plot

The plot in Figure 5.12 shows that the numerically determined swirl number is around the 1.4 value calculated using Eq. 2.5. When the flow reaches the fuel injector height, the swirl number drops to 1.35. The initial increase of the swirl number is most likely due to left-handed tangential velocities present inside the wake regions of the swirler blades.

Finally, the velocity field inside the swirler was analyzed. To visualize the flow within the swirler, a cylindrical section in the axial direction and several radial sections spanning the volume between two swirler blades were used. These sections are illustrated in Figure 5.13. The velocity magnitude contours on the sections illustrated in Figure 5.13, are given in Figures 5.14 and 5.15.

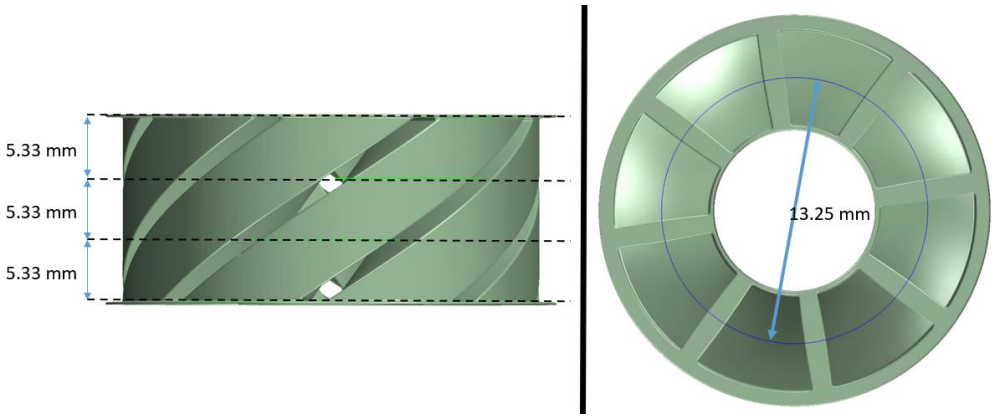

Figure 5.13. Sections used to visualize swirler air flow

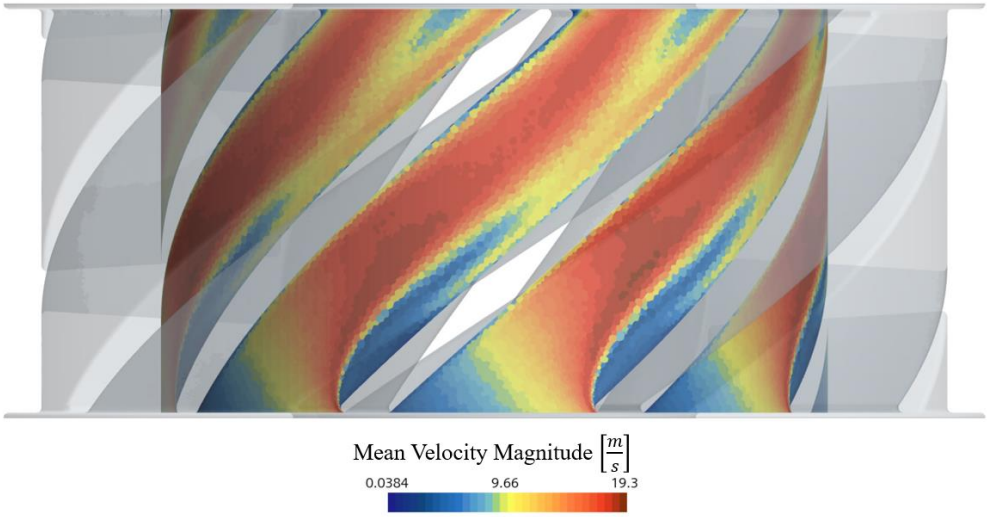

Figure 5.14. Mean velocity magnitude contours on the cylindrical swirler section

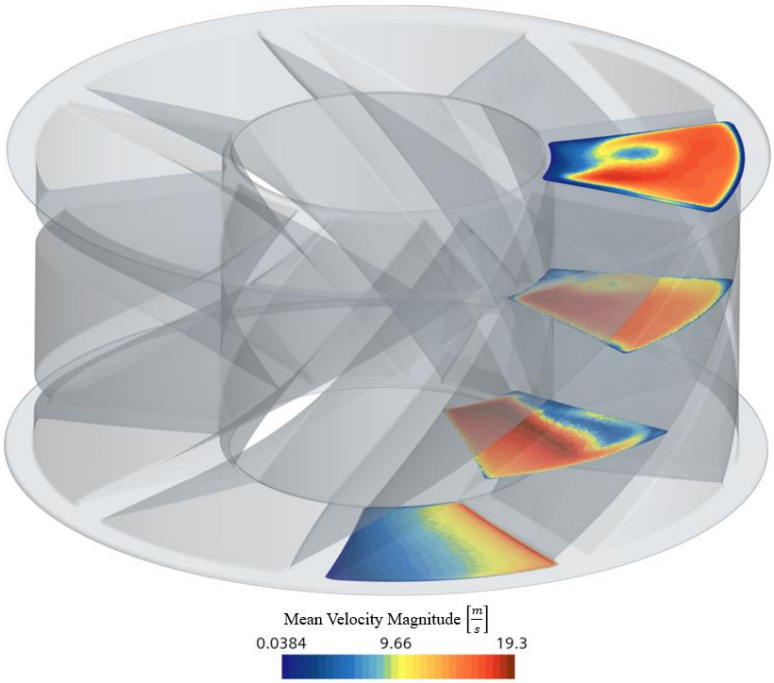

Figure 5.15. Mean velocity magnitude contours on the radial swirler sections

As seen from Figures 5.14 and 5.15, when the flow first encounters the swirling blades, a low-velocity wake region emerges on the low-pressure blade. This low-velocity region gets a circular shape as the flow progresses downstream. This might be due to a vortex near the low-pressure wall. The existence of this vortex is further supported by the total turbulence energy and mean vorticity contours. For the vorticity contours, the time mean of the vorticity field was calculated over five time steps. These contours are illustrated in Figures 5.16 and 5.17. In Figure 5.17, to visualize the vorticity away from the walls, the numerical cells that are less than 0.5 mm away from a wall are not visualized.

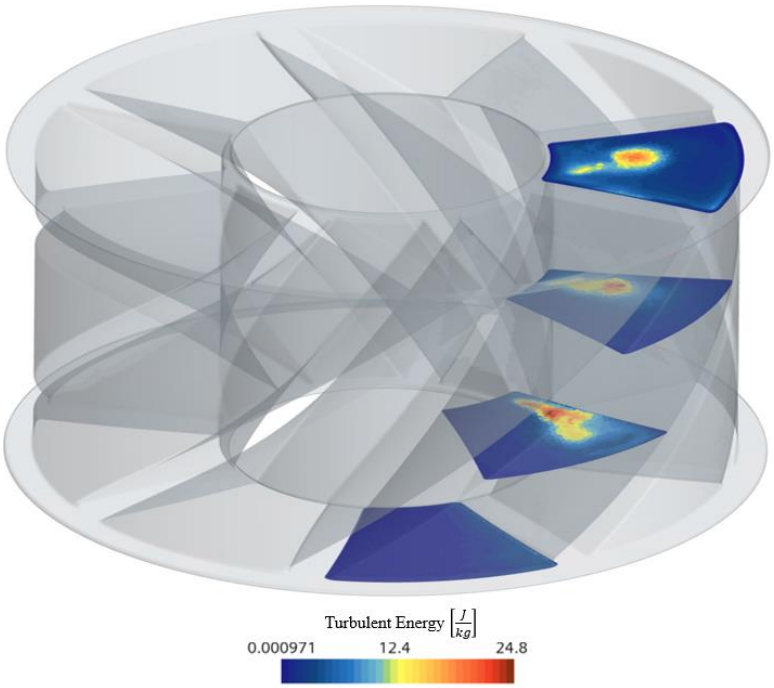

Figure 5.16. Total turbulent energy contours on radial swirler sections

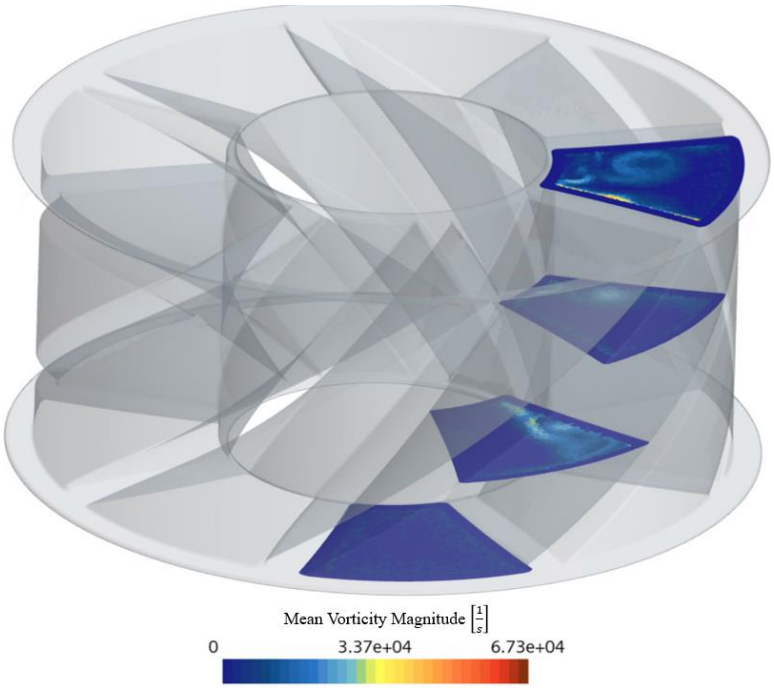

Figure 5.17. Vorticity magnitude contours on radial swirler sections

5.2.2 CRZ Shape

As mentioned in section 2.2.4, the expected CRZ was a single zone where the recirculation region created by vortex breakdown and the wake region of center body are combined. The shape of the CRZ is illustrated in Figure 5.18 where the y-velocity contour is clipped where the value goes above 0. The illustrated result was taken from no hydrogen addition case simulations.

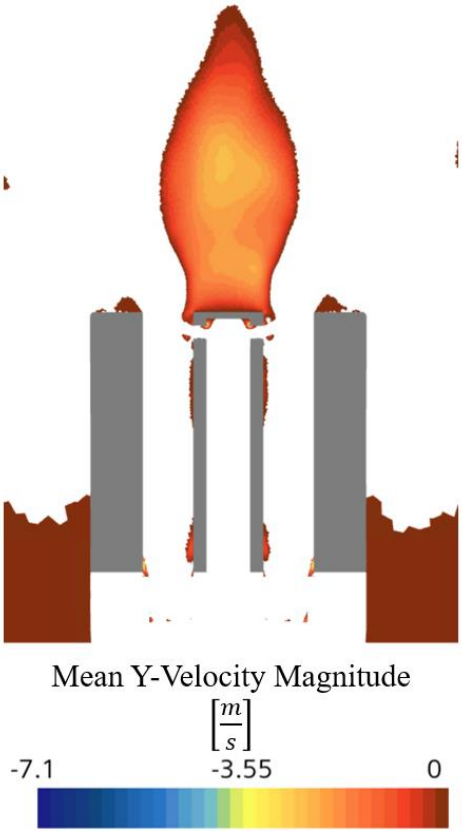

Figure 5.18. Axial section y-velocity contours with values above 0 clipped

Furthermore, the toroidal vortex is visualized in the vector plot given in Figure 5.19.

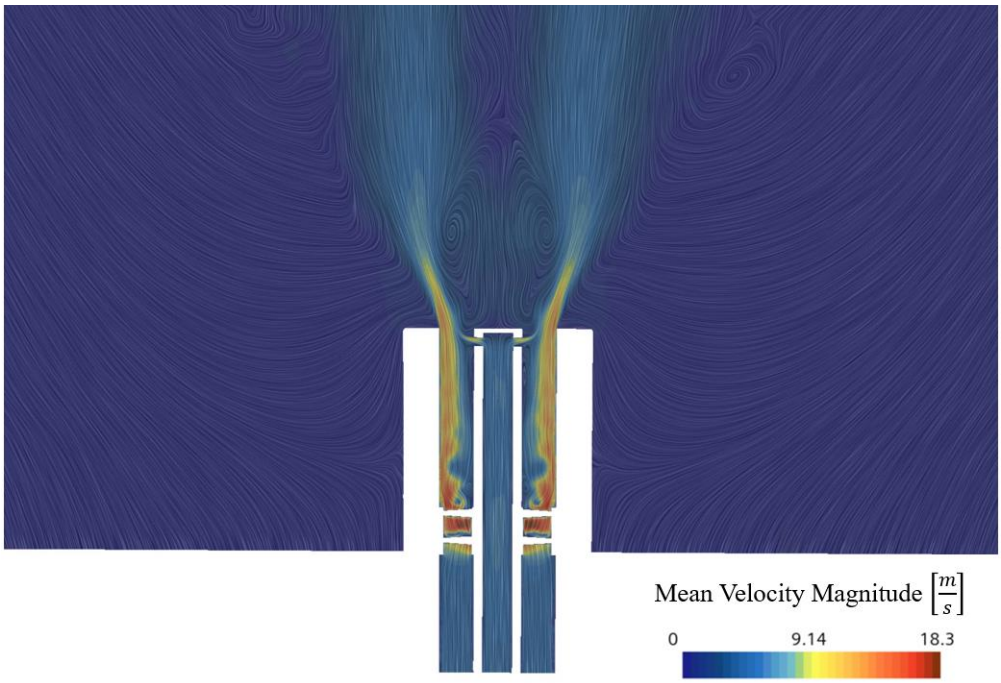

Figure 5.19. Axial section velocity vector plot

Finally, the flame position and the mean velocity magnitude contours for no hydrogen addition case were analyzed. To visualize the data, a velocity magnitude contour was created on an axial section, and numerical cells with average chemical heat release rate (CHRR) values higher than 40% of the maximum value were colored orange. The resulting contours are shown in Figure 5.20.

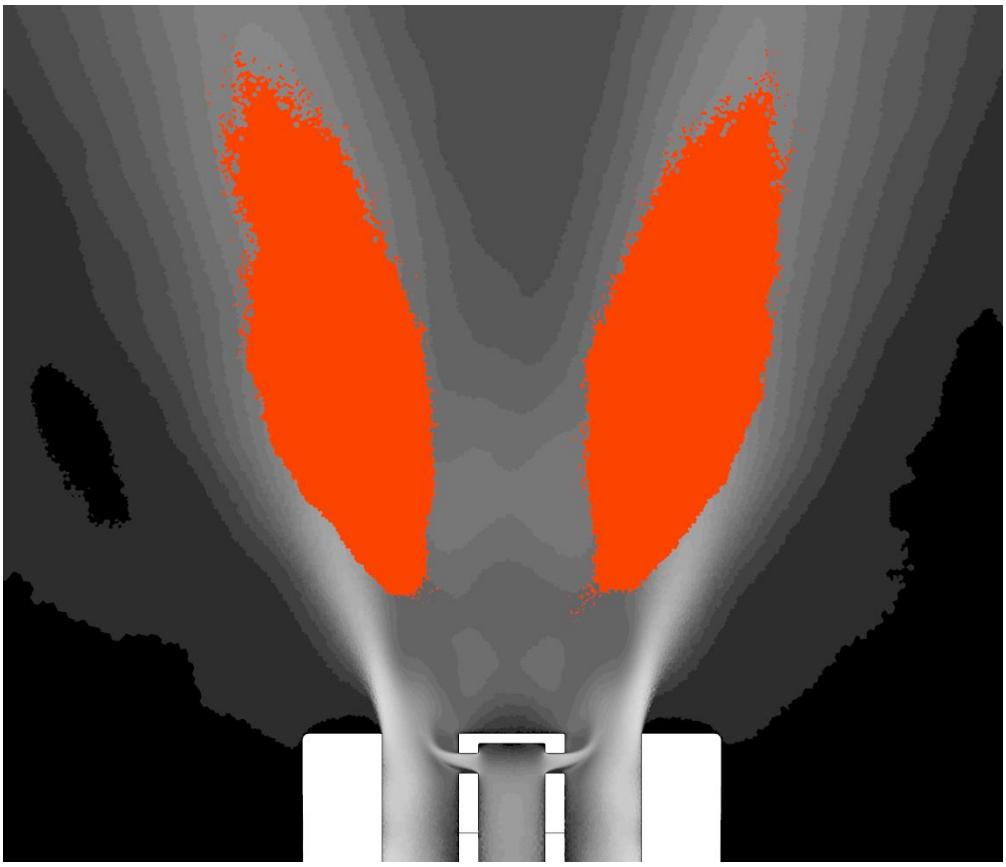

Figure 5.20. Axial section velocity magnitude contours for numerical cells having average CHRR values higher than 40% of the maximum mean CHRR value are colored orange.

As we can observe from Figure 5.20, the flame resides in the inner shear layer (ISL), where the swirling jets meet the CRZ.

5.2.3 Wall Temperature Results

After the 30 H2VOL% computations were finalized, the fuel condition was switched to 60 H2VOL%. Before starting the computations for this mixture condition, the solid regions were added to the numerical simulation domain, and the conjugate heat transfer (CHT) model was turned on. The wall temperature was initialized at 300K, and the simulation was conducted until the wall temperature was stabilized. The

resulting wall temperature plot at the end of the 60 H2VOL% case computations is shown in Figure 5.21.

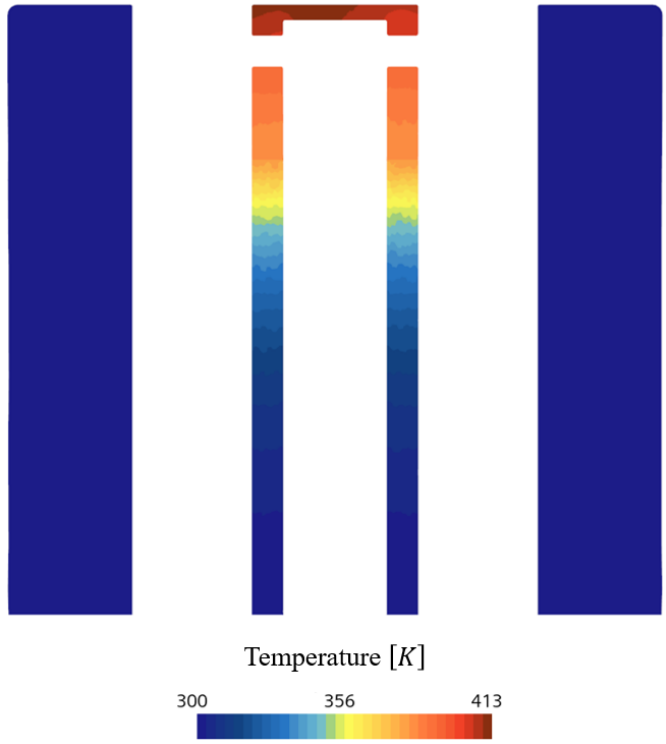

Figure 5.21. Axial section wall temperature contours at the end of 60 H2VOL% case computations

As observed from Figure 5.21, the maximum wall temperature goes up to 413 K, and the hottest part of the burner walls is the brass top part of the central fuel pipe. This was expected since the resulting flame for 60 H2VOL% case is still lifted off, and the hottest gases near the walls were the hot exhaust gases carried upstream by the CRZ. This can be seen in Figure 5.22, where the temperature field of the 60 H2VOL% case computations are illustrated using an axial mean temperature contour.

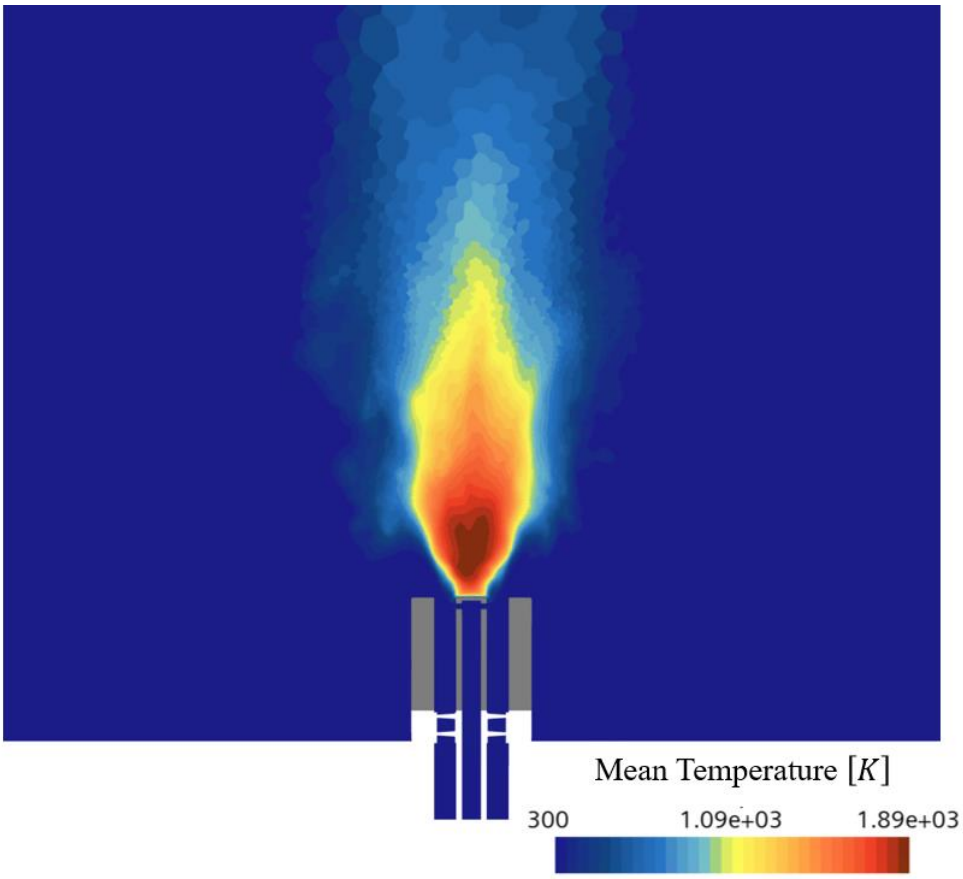

Figure 5.22. Axial mean temperature contours for 60 H2VOL% computations

Additionally, the wall contacting fuel flow was also heated since the wall temperatures are elevated. A temperature contour was created to analyze the heating of the fuel flow. Only the numerical cells with the fuel mixture fraction higher than 0.95 and progress variable lower than 0.05 were used to gather only the fuel temperature before mixing or burning. Then, using these numerical cells, a fuel temperature contour was created. This contour is shown in Figure 5.23.

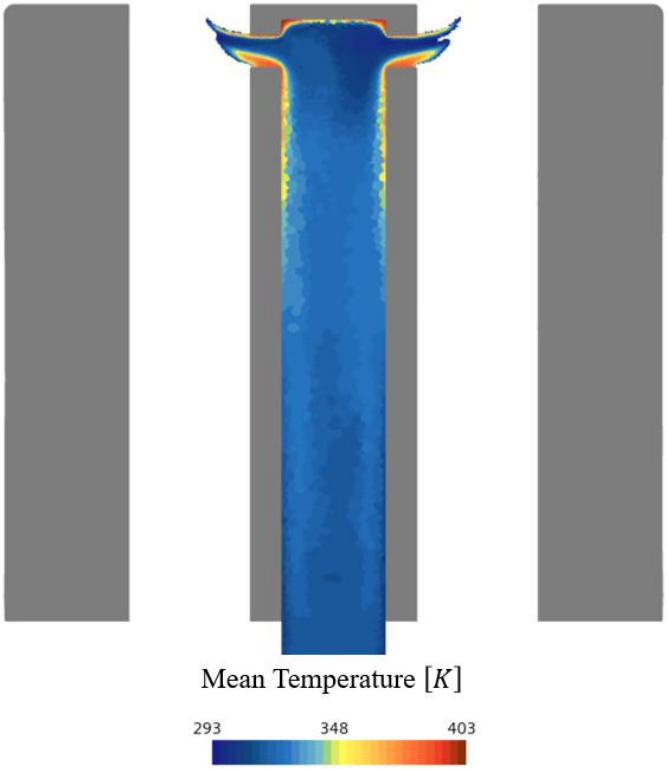

Figure 5.23. Axial section fuel temperature contour

As observed from Figure 5.23, the fuel flow is heated up to 403K by the wall heat flux. The average mean fluid temperature over the exit surface of one of the fuel injector holes was determined to be 359 K. which means the fuel flow was heated to an average temperature of 359 K from its initial temperature of 293 K.

After the fuel condition was switched to 70 H2VOL% and the flame was attached to the central fuel pipe, the wall temperature rose rapidly. Until the flame attachment was completed, the maximum wall temperature rose to 457 K. This is illustrated in Figure 5.24.

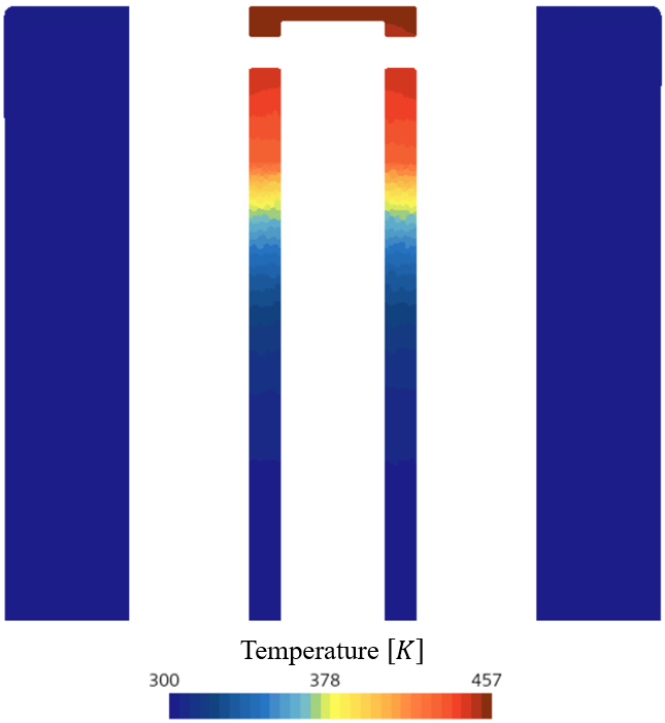

Figure 5.24. Axial section walls temperature contours for 70 H2VOL% case computations after the flame attachment

The heating of the wall is due to hot burnt gases flowing directly against the side walls of the central fuel pipe. This is because the flame becomes attached to the wall under the fuel injectors. This effect is illustrated in the instantaneous temperature contour for the 70 H2VOL% computations, after the flame attachment in Figure 5.25.

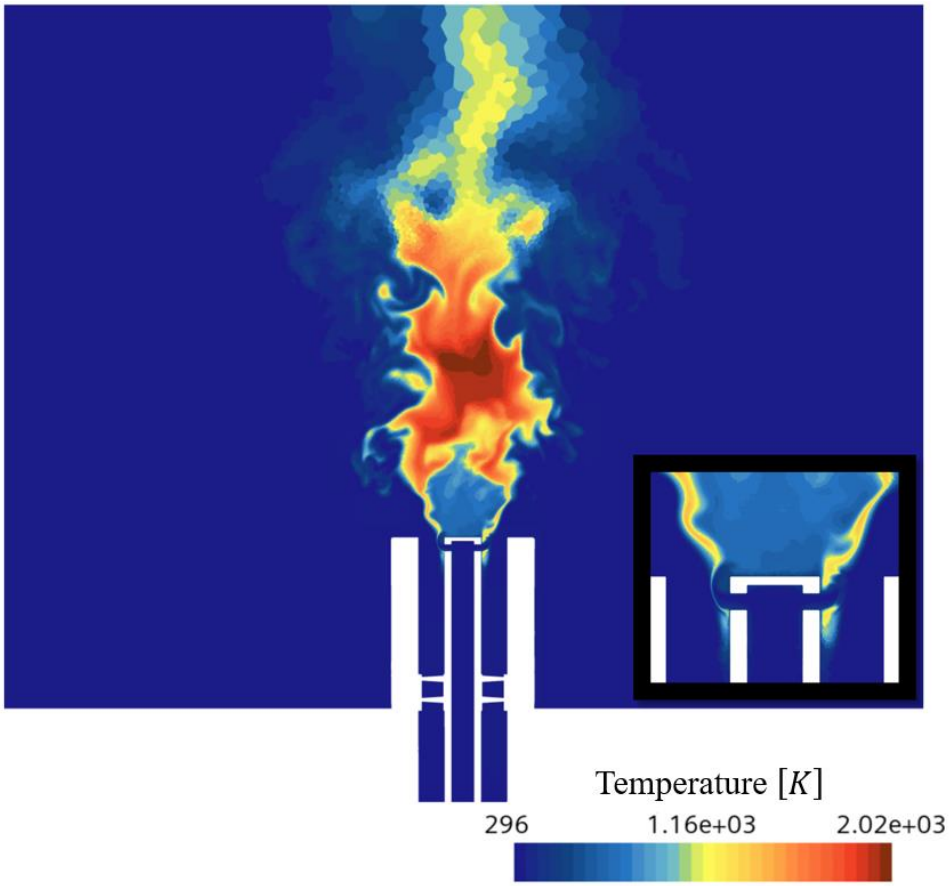

Figure 5.25. Axial section instantaneous temperature contours for 70 H2VOL% case computations after flame attachment, with the fuel injector zone zoomed in

5.2.4 Effect of Hydrogen Addition on the Flame Stability Limits

Similarly, to the experimental procedure, numerical simulations were conducted for different fuel conditions by incrementally increasing the H2VOL%. A single simulation file was created with no hydrogen. After gathering average values for that fuel condition, the following fuel condition was initiated from the last time step of the previous fuel condition. From the experiments, it was observed that flame attachment occurs after increasing the H2VOL% from 60 to 70. After the 60 H2VOL% case computations ended, the H2VOL% to 70. Like the experiments, this resulted in the flame getting attached to the central fuel pipe. To illustrate this effect, the mean chemical heat release rates (CHRR) volume renderings for 0, 30, 60, and

70 H2VOL% computations are presented in Figures 5.26 and 5.27. The average CHRR field was collected after the flame stabilization mode transition was completed and the flame stabilized attached to the burner.

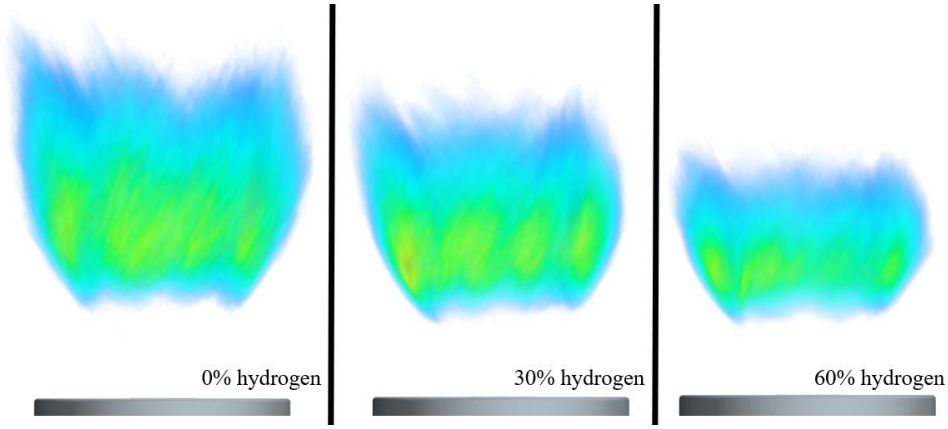

Figure 5.26. Mean volume renderings of CHRR fields for 0, 30 and 60 H2VOL% cases

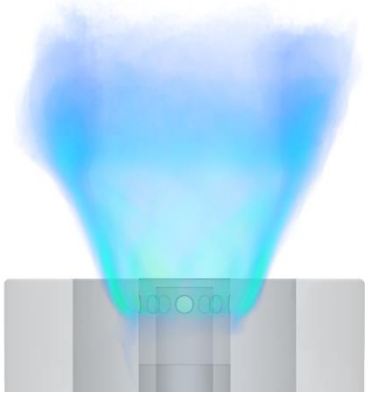

Figure 5.27. Mean volume renderings of the CHRR field for 70 H2VOL% case

As observed clearly in Figure 5.26, for flames with 0, 30, and 60 H2VOL% the resulting flame is lifted, like in the experiments. However, after the H2VOL% increases to 70, the flame attaches to the burner. This can be observed in Figure 5.27. This indicates that the numerical setup we developed simulates accurately the flame stabilization mode change phenomenon. Furthermore, this also means that this numerical setup can be used to design burners to avoid flame attachment. The dynamics of how this flame attachment occurs is detailed in the following sections.

5.2.5 Effect of Hydrogen Addition on the Flame Position and Dimensions

Like the analysis of the experimental results, flame length, width, and lift-off height parameters were determined from the numerical results. How this was done was detailed in section 4.5. Since these parameters are only relevant for the lifted-off flames, they were collected only for 0, 30, and 60 H2VOL% cases. The results are presented in Figure 5.28.

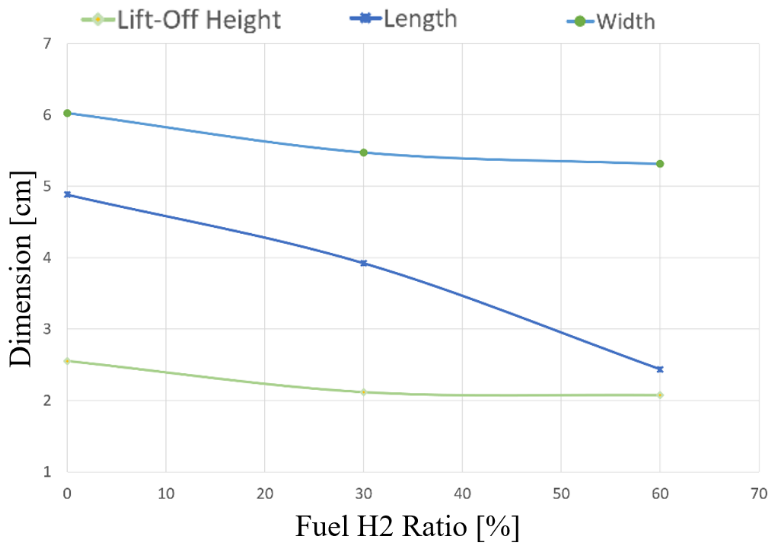

Figure 5.28. Numerical flame positional and dimensional parameters plotted against the H2VOL%

As observed in Figure 5.28, the general trend of flame lowering to the burner and shrinking was captured in the numerical simulations.

5.2.6 Effect of Hydrogen addition on Fuel Jets and Mixing

Since hydrogen has a much lower density than natural gas, as the H2VOL% increases, the mixture's density decreases. Since the total volumetric flow rate of the fuel mixture is kept constant in our study, the momentum of the radial fuel jets decreases. The total momentum of a single fuel jet measured at the exit of the injection hole for different fuel conditions is plotted in Figure 5.29.

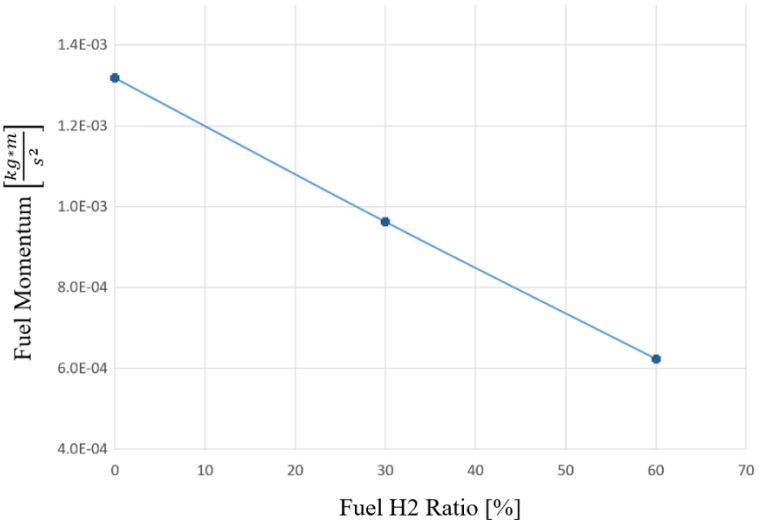

Figure 5.29. Momentum of a single radial fuel jet for different fuel mixtures

The result is a better mixing of the fuel and the swirling air before the mixture leaves the burner exit section. The mixing of the fuel and air at the burner exit plane was measured using the maximum mean mixture fraction (MF) values at the burner exit plane. This value is chosen since high MF would indicate the fuel jet reaching the burner exit without dispersing. The maximum mean mixture fraction values at the burner exit for different fuel conditions are given in Figure 5.30. This figure shows that with increasing H2VOL%, the fuel mixes better and quicker with the swirling air (as the maximum mixture fraction at the burner exit decreases with the hydrogen addition rate). This behavior increases the potential for the ignition of the mixture close to the fuel injection ports, triggering the flame attachment to the burner and explaining the flame stabilization mode change for fuel mixtures with H2VOL% higher than 60.

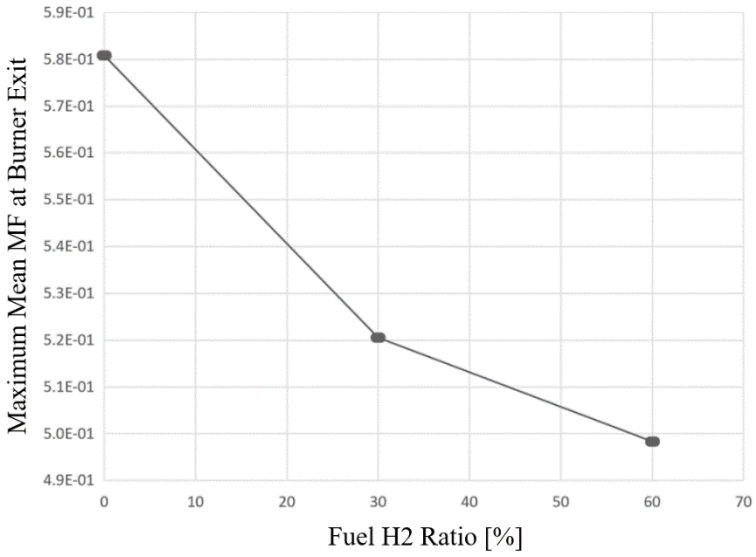

Figure 5.30. Maximum mean MF values at the burner exit for different fuel mixture conditions

5.2.7 Dynamics of Flame Stabilization Mode Change

During the numerical simulations, the flame stabilization mode change started to happen after the fuel condition was changed from 60 to 70 H2VOL%. The process of stabilization mode change included the following steps.

1. After the fuel condition changed, lower parts of the flame were able to propagate downstream and reach the fuel jets injection region.
2. A part of the flame was able to ignite the fuel-air mixing surface present at the lower side of the fuel jet.
3. The resulting flame under one of the fuel jets was then able to ignite the under sides of all the fuel jets in a circular motion in a right-handed direction.
4. This results in the attachment of the flame to the fuel ports replacing the lifted-off flame stabilization mode.

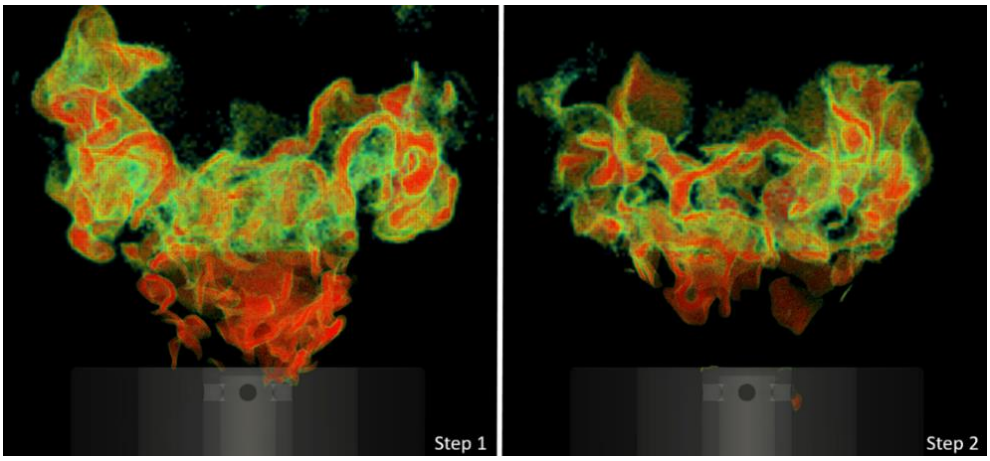

Figure 5.31. The first two steps of the stabilization mode change process as seen from a radial direction

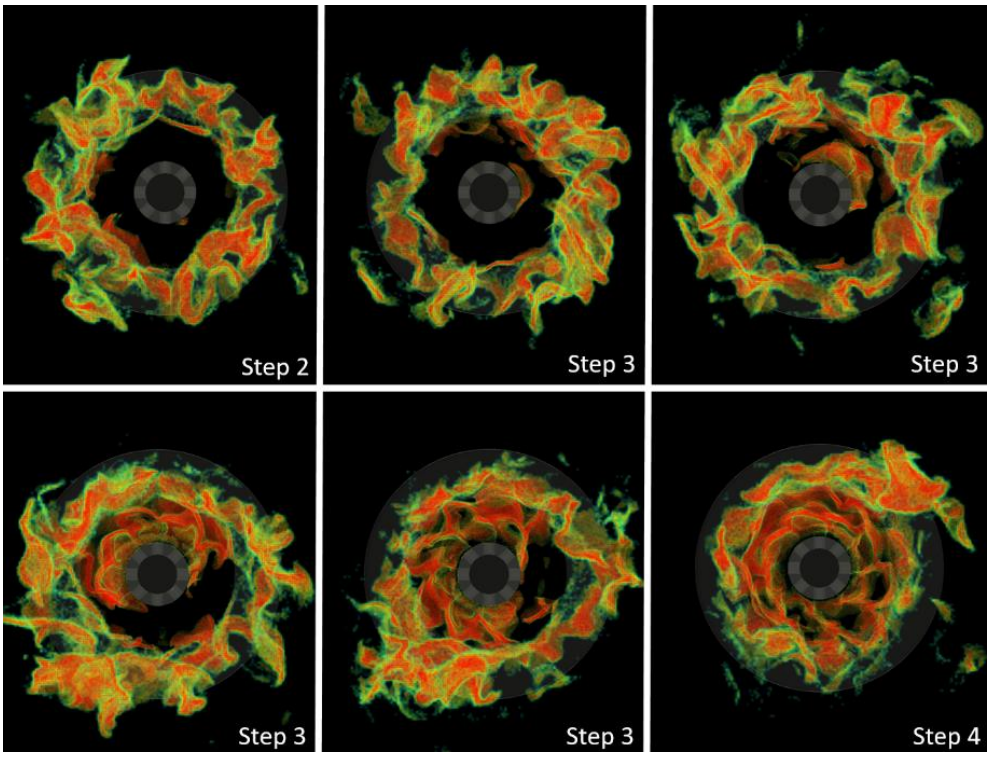

Figure 5.32. The last three steps of the stabilization mode change seen from a top-down direction

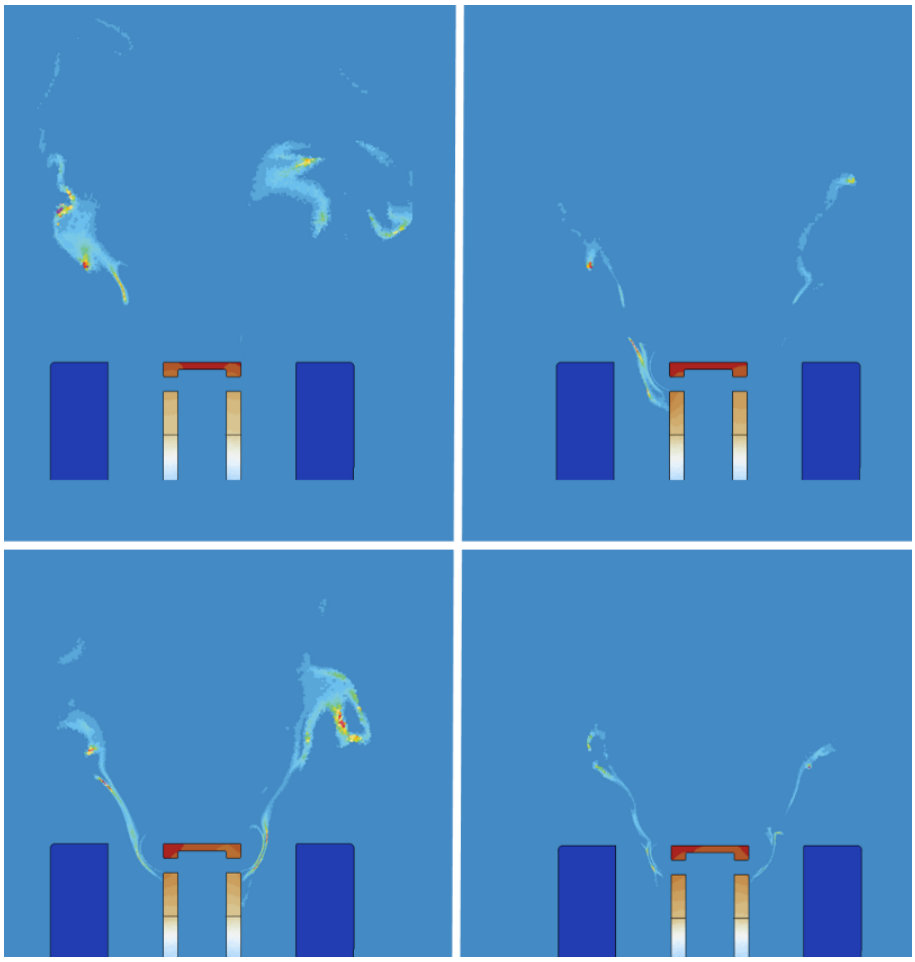

Figure 5.33. Stabilization mode change process illustrated in a planar section view using the CHRR field contours

These steps are illustrated using volume renderings of instantaneous CHRR fields in Figures 5.31 and 5.32. Additionally, the stabilization mode change process is illustrated in a planar section view using the CHRR field contours in Figure 5.33. As seen in Figure 5.32, the right-handed circular motion of the initial flamelet (or flame element) around the injection section is fundamental for the stabilization mode change phenomenon. The direction of this flame element motion corresponds to the direction of the swirl within the annular air jet. As discussed in section 5.4.3, this knowledge can be used to design better burners that avoid this stabilization mode change phenomenon by hindering the spreading motion of the initial flame element attached to injection port.

5.3 Comparison of Experimental and Numerical Results

As mentioned in previous sections, the flame stabilization mode change occurred while changing the fuel condition from 60 to 70 H2VOL%, for both experiments and numerical simulations. This constitutes the first indication showing that numerical computations and experiments agree well.

The dimensional and positional flame parameters are the second indicator for comparing the experimental and numerical results. In Figure 5.34, the flame lift-off height, flame width, and length values are plotted for both numerical and experimental results.

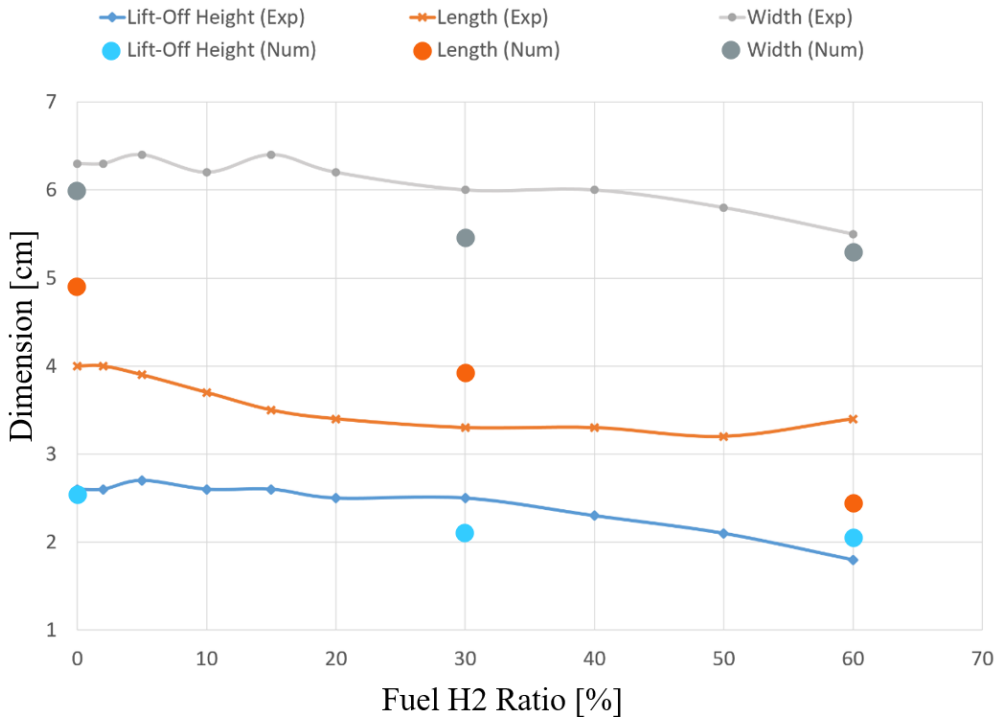

Figure 5.34. Flame lift-off height, width and length values plotted against the H2VOL% for numerical and experimental results

The comparison of these results is discussed further in section 5.4.1.

5.4 Discussion of the Results

In this section, the numerical and experimental results are discussed. The discussion includes the comparison of experimental and numerical results, explanations for the effects of H2VOL%, and possible design choices for extending the lifted-off flame stabilization limits.

5.4.1 Numerical and Experimental Results

As described in section 5.3, the experimental and numerical results generally agree well. As observed in Figure 5.34, the global flame shrinking and lowering effects of H2VOL% are captured both in the experiments and computations. Comparing the parameters separately, it is observed that the agreements between lift-off height and width are better compared to the agreement between flame length results. In the numerical results, the flame length is predicted to be longer than experimental results for 0 and 30 H2VOL% and lower for the 60 H2VOL% case. This effect is also observed in the numerical CHRR volumetric renderings and the experimental chemiluminescence images.

5.4.2 Explanations for the Effects of Hydrogen Addition

The effects of H2VOL% on the flame parameters can be explained by the higher flame propagation speed of hydrogen. Since the laminar flame speed of hydrogen is drastically higher than the corresponding NG flame speed, when hydrogen is added to the fuel mixture, the flame propagation speed of the mixture above the burner exit and around the fuel jets equally increases. This effect explains the geometrical shrinking of the flame region. Since the hydrogenated mixture can burn much faster than the NG flame, the combustion process can be terminated within a much smaller volume. Additionally, this effect explains why the flames with high H2VOL%

progress upstream in the swirling jet, reaching the radial fuel jets. This is a phenomenon similar to flame flashback.

Similarly, the increase of the laminar flame speed can also explain the effect of decreasing the lift-off height of the flame. Higher swirling jet velocities are needed to stabilize the flame since the hydrogenated mixtures have a higher flame propagation rate. Since after exiting the air duct, the swirling jet's momentum dissipates to the surrounding fluid, maximum swirling jet velocities are found closer to the duct exit. Thus, to be stabilized the flame must get closer and closer to the high-velocity field near the burner exit as hydrogen is added to the fuel mixture.

Another possible reason for the shrinking of the flame is the decreasing global equivalence ratio and fuel power output of the flame. As shown in Figure 3.10, when hydrogen is added to the fuel mixture, the global equivalence ratio and the fuel power output of the flame diminish. The associated decrease of the heat release and of the volume expansion due to density reduction could cause the flame region volume to decrease.

Finally, as seen in Figure 5.30, adding hydrogen to the fuel mixture results in a better-mixed fuel and air mixture at the burner exit plane. This might result in a better pathway for the flame to propagate and, in turn, might be contributing to both the lowering of the flame and the stabilization mode transition.

5.4.3 Possible Design Choices for Extending Lifted-Off Flame Stabilization Limits

The analysis of the effects of hydrogen addition and of the dynamics of flame stabilization mode change indicates several possible design choices for a burner that will stabilize a lifted flame for higher hydrogen addition rates (and eventually for 100% hydrogen). The possible design choices are as follows.

- Lower Swirl Number Blades

As remarked by Merlo et al. in their study on swirled flames [40], higher swirl numbers tend to decrease the lift-off height of swirl-stabilized flames. Since in section 5.2.5, it is determined that the flame getting lower toward the burner makes the flame more prone to burner attachment, keeping the flame lift-off height high can help avoiding flame attachment. However, lowering the swirl number might lower the effectiveness of the partial pre-mixing of fuel and air in the burner. This represents a trade-off between stability and low emissions.

- Smaller Radial Fuel Injection Holes

As detailed in section 5.2.7, when the flame is attached to the burner, it stabilizes on the interface surface between the swirled air jet and radial fuel jets. By decreasing the fuel injection hole diameters, the fuel jet velocity can be increased while the fuel jet size is decreased. This would provide two advantages; one is that the interface between the swirling air jet and the fuel jets can be decreased, decreasing the area for the flame to stabilize. The second advantage is that since the fuel jets would be faster, the velocity gradients between the fuel jets and the air jet would be larger and exert higher stretch rates to the flame. This may lead to extinguishing any flame that reaches the underside of the radial fuel jets and prevent flame attachement to the burner. This effect can also be achieved by increasing the volumetric flow rate of the fuel.

- Fuel Injection Holes Inclined Against the Swirl Direction

As detailed in section 5.2.7 as the stabilization mode change happens, first, a flame elememt is stabilized under one of the fuel injection ports. This flamelet then ignites the fuel jets' undersides in a circular motion. Since this circular motion is necessary to complete flame attachment, the fuel injection holes can be inlined against the swirl direction. This concept is illustrated in Figure 5.35.

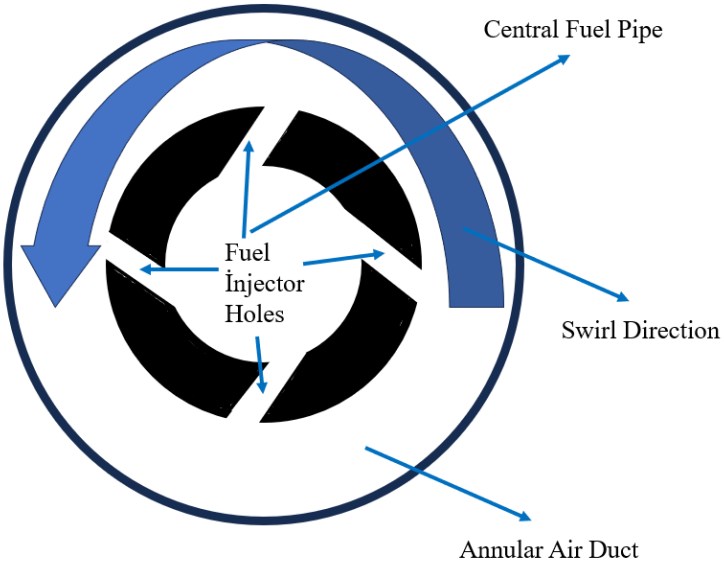

Figure 5.35. Illustration of fuel injection holes inclined against the swirl direction

The direction of the fuel jet exiting these inclined fuel injection holes can then hinder the circular motion of the flame element needed to complete the attachment of the flame to the burner.

CHAPTER 6

CONCLUSIONS AND FUTURE WORK

6.1 Conclusions

In this study, swirl-stabilized partially premixed turbulent natural gas-air, and natural gas-hydrogen-air flames with different H2VOL% were investigated experimentally and numerically. The experiments were performed under room conditions open to the atmosphere. An experimental burner was designed and manufactured. The experimental burner consisted of an axial swirler with a geometric swirl number of 1.4 and eight radial fuel injection holes. Eleven fuel conditions were investigated experimentally, ranging from pure NG to 70 H2VOL%. The measurements were performed using chemiluminescence imaging of OH* radical species. Using the chemiluminescence imaging technique, one thousand images were collected within one second for ten fuel mixture conditions. No chemiluminescence images were collected for the 70 H2VOL% condition. For this condition , the flame transitioned to a different stabilization mode and became attached to the burner's central fuel pipe external wall.

10 000 images were then collected for the ten fuel conditions. The images collected were processed using MATLAB scripts. ten mean OH* chemiluminescence images were created using a MATLAB script that takes the average of an image series. These images were then superimposed on a scaling picture of the burner. The superimposed pictures were analyzed using another MATLAB script to gather the flame lift-off distance, width, and height parameters.

Additionally, numerical simulations were performed using the experimental burner geometry and some of the fuel and air conditions used in the experiments. Numerical simulations were performed for 0, 30, 60, and 70 H2VOL%. These numerical simulations were conducted using the StarCCM+ software 22.06 version. In the

simulations, turbulence was modeled using the LES approach, combustion was modeled using the FGM model, and turbulence-chemistry interaction was modeled using the thickened flame model. The results of the numerical simulations were analyzed using average chemical heat release rate (CHRR) fields gathered for 0, 30, and 60 H2VOL%. From the average CHRR fields, flame lift-off distance, width, and height parameters were calculated. For the 70 H2VOL% case, the flame became attached to the burner in the numerical simulations, similarly to the experiments.

The experimental results showed that adding hydrogen to the fuel mixture caused the flame to lower and become closer to the burner. It also caused the flame width and length to decrease, shrinking the flame. Additionally, the resulting flame was lifted off for H2VOL% lower than 70. But, increasing the H2VOL% from 60 to 70 caused the flame to become attached to the burner walls. The numerical simulation results were compared to the experiments. It was observed that the flame shrinking and lowering effect of hydrogen addition to the fuel was also observed in the numerical simulations.

Furthermore, numerical simulations also predicted the stability change occurring when the H2VOL%was increased from 60 to 70. This shows the potential of LES simulations coupled with the TFM model for predicting the characteristics of partially premixed swirl-stabilized turbulent flames. Using these analysis methods, new burner geometries can be designed for operating with higher hydrogen ratios in the fuel mixtures. Several design ideas for this goal were presented in the thesis.

6.2 Future Work

During this thesis work, an experimental setup was designed, manufactured, and operated to investigate swirl-stabilized partially premixed NG-hydrogen-air turbulent flames. Additionally, a numerical setup was created to predict the characteristics of such flames. The suggested future work are as follows:

- A high-pressure chamber should be built to enclose the swirl burner, so the effect of high pressure can be assessed on these flames. Since a high-pressure environment would better simulate the combustion chamber of a gas turbine, the effects of high pressures on the flame dimension, position, and stability characteristics are important and should be determined.
- As described in section 5.4.3, new burner parts should be designed and produced for the experimental combustor with new experimental design features to analyze the effect on the flame stabilization limits, position, and dimensions. A simple design experiment can involve new geometries for the screw-on fuel injector part. Additionally, since the experimental burner was designed with easy modifications in mind, the height and geometry of the swirler blades can be changed by manufacturing new sleeve parts and manufacturing new blades.
- New burner geometries should be explored before manufacturing using the developed numerical setup to reduce experimental time and cost. Additionally, the numerical burner geometry can be parametrized, and an optimization study can be performed using an optimization code.

REFERENCES

[1] N. Tanaka and others, “World energy outlook 2010,” *International Energy Agency. Paris: IEA*, 2010.

[2] D. Gielen, E. Taibi, R. Miranda, and others, “Hydrogen: A renewable energy perspective,” *Abu Dhabi: International Renewable Energy Agency*, 2019.

[3] B. Yilmaz, S. Özdogan, and I. Gökalp, “Influence of Hydrogen Addition on Lean Premixed Methane-Air Flame Statistics,” in *Engineering Systems Design and Analysis*, 2010, pp. 281–287.

[4] F. Halter, C. Chauveau, and I. Gökalp, “Characterization of the effects of hydrogen addition in premixed methane/air flames,” *Int J Hydrogen Energy*, vol. 32, no. 13, pp. 2585–2592, 2007.

[5] C. Cohé, F. Halter, C. Chauveau, I. Gökalp, and Ö. L. Gülder, “Fractal characterisation of high-pressure and hydrogen-enriched CH4–air turbulent premixed flames,” *Proceedings of the Combustion Institute*, vol. 31, no. 1, pp. 1345–1352, 2007.

[6] F. Halter, C. Chauveau, N. Djebaïli-Chaumeix, and I. Gökalp, “Characterization of the effects of pressure and hydrogen concentration on laminar burning velocities of methane–hydrogen–air mixtures,” *Proceedings of the Combustion Institute*, vol. 30, no. 1, pp. 201–208, 2005.

[7] N. Bouvet, C. Chauveau, I. Gökalp, S.-Y. Lee, and R. J. Santoro, “Characterization of syngas laminar flames using the Bunsen burner configuration,” *Int J Hydrogen Energy*, vol. 36, no. 1, pp. 992–1005, 2011.

[8] N. Bouvet, C. Chauveau, I. Gökalp, and F. Halter, “Experimental studies of the fundamental flame speeds of syngas (H2/CO)/air mixtures,” *Proceedings of the Combustion Institute*, vol. 33, no. 1, pp. 913–920, 2011.

[9] P. Palies, “Stabilization and Dynamic of Premixed Swirling Flames: Prevaporized, Stratified, Partially, and Fully Premixed Regimes,” 2020.

[10] K. K. Kuo and R. Acharya, *Fundamentals of turbulent and multiphase combustion*. John Wiley & Sons, 2012.

[11] C. K. Law and C. J. Sung, “Structure, aerodynamics, and geometry of premixed flamelets,” *Prog Energy Combust Sci*, vol. 26, no. 4–6, pp. 459–505, 2000.

[12] T. Poinsot and D. Veynante, *Theoretical and numerical combustion*. RT Edwards, Inc., 2005.

[13] C. Dong, Q. Zhou, X. Zhang, Q. Zhao, T. Xu, and S. Hui, “Experimental study on the laminar flame speed of hydrogen/natural gas/air mixtures,” *Frontiers of Chemical Engineering in China*, vol. 4, pp. 417–422, 2010.

[14] B. MOO LEE and H. DONG SHIN, “Differential diffusion effects in H2/N2 turbulent nonpremixed flames,” *Combustion science and technology*, vol. 62, no. 4–6, pp. 311–330, 1988.

[15] N. Peters, “Turbulent combustion,” *Meas Sci Technol*, vol. 12, no. 11, p. 2022, 2001.

[16] T. B. Kıymaz *et al.*, “Numerical investigations on flashback dynamics of premixed methane-hydrogen-air laminar flames,” *Int J Hydrogen Energy*, vol. 47, no. 59, pp. 25022–25033, 2022.

[17] T. Boushaki, “Introductory chapter: swirling flows and flames,” *Swirling Flows and Flames*, 2019.

[18] E. M. Greitzer, C. S. Tan, and M. B. Graf, “Internal flow: concepts and applications,” 2007.

[19] A. N. Kolmogorov, “The local structure of turbulence in incompressible viscous fluid for very large Reynolds numbers,” *Proc R Soc Lond A Math Phys Sci*, vol. 434, no. 1890, pp. 9–13, 1991.

[20] P. A. Davidson, *Turbulence: an introduction for scientists and engineers*. Oxford university press, 2015.

[21] D. R. Radenković, J. M. Burazer, and ore M. Novković, “Anisotropy analysis of turbulent swirl flow,” *FME Transactions*, vol. 42, no. 1, pp. 19–25, 2014.

[22] B. Y. Belal, G. Li, Z. Zhang, H. M. El-Batsh, H. A. Moneib, and A. M. A. Attia, “The effect of swirl burner design configuration on combustion and emission characteristics of lean pre-vaporized premixed flames,” *Energy*, vol. 228, p. 120622, 2021.

[23] J. O’Connor and T. Lieuwen, “Recirculation zone dynamics of a transversely excited swirl flow and flame,” *Physics of fluids*, vol. 24, no. 7, pp. 2893–2900, 2012.

[24] L. Gramer, “Kelvin–Helmholtz instabilities/GFD-II,” *National Oceanic and Atmospheric Association Report*, 2007.

[25] I. Yılmaz, “Effect of swirl number on combustion characteristics in a natural gas diffusion flame,” *J Energy Resour Technol*, vol. 135, no. 4, 2013.

[26] F. Lückoff, M. Sieber, C. O. Paschereit, and K. Oberleithner, “Phase-opposition control of the precessing vortex core in turbulent swirl flames for investigation of mixing and flame stability,” *J Eng Gas Turbine Power*, vol. 141, no. 11, p. 111008, 2019.

[27] S. Terhaar, K. Oberleithner, and C. O. Paschereit, “Key parameters governing the precessing vortex core in reacting flows: An experimental and analytical study,” *Proceedings of the Combustion Institute*, vol. 35, no. 3, pp. 3347–3354, 2015.

[28] K. Oberleithner, S. Terhaar, L. Rukes, and C. Oliver Paschereit, “Why nonuniform density suppresses the precessing vortex core,” *J Eng Gas Turbine Power*, vol. 135, no. 12, 2013.

[29] Q. An, W. Y. Kwong, B. D. Geraedts, and A. M. Steinberg, “Coupled dynamics of lift-off and precessing vortex core formation in swirl flames,” *Combust Flame*, vol. 168, pp. 228–239, 2016.

[30] A. Tyliszczak, D. E. Cavaliere, and E. Mastorakos, “LES/CMC of blow-off in a liquid fueled swirl burner,” *Flow Turbul Combust*, vol. 92, pp. 237–267, 2014.

[31] N. Swaminathan, G. Xu, A. P. Dowling, and R. Balachandran, “Heat release rate correlation and combustion noise in premixed flames,” *J Fluid Mech*, vol. 681, pp. 80–115, 2011.

[32] K. S. Hasan, W. A. Abd Al-wahid, and H. H. S. Khwayyir, “Flashback and combustion stability in swirl burners,” in *IOP Conference Series: Materials Science and Engineering*, 2020, p. 22045.

[33] J. Fritz, M. Kröner, and T. Sattelmayer, “Flashback in a swirl burner with cylindrical premixing zone,” *J. Eng. Gas Turbines Power*, vol. 126, no. 2, pp. 276–283, 2004.

[34] B. Lewis and G. Von Elbe, *Combustion, flames and explosions of gases*. Elsevier, 2012.

[35] T. Sattelmayer, “Influence of the combustor aerodynamics on combustion instabilities from equivalence ratio fluctuations,” *J. Eng. Gas Turbines Power*, vol. 125, no. 1, pp. 11–19, 2003.

[36] C. Guin, “Characterisation of autoignition and flashback in premixed injection systems,” in *RTO Meeting proceedings*, 1999.

[37] I. Gökalp, “On the correlation of turbulent burning velocities,” *Combustion Science and Technology*, vol. 23, no. 3–4, pp. 137–142, 1980.

[38] G. W. Koroll, R. K. Kumar, and E. M. Bowles, “Burning velocities of hydrogen-air mixtures,” *Combust Flame*, vol. 94, no. 3, pp. 330–340, 1993.

[39] R. G. Abdel-Gayed, D. Bradley, and F.-K. Lung, “Combustion regimes and the straining of turbulent premixed flames,” *Combust Flame*, vol. 76, no. 2, pp. 213–218, 1989.

[40] N. Merlo *et al.*, “Experimental study of oxygen enrichment effects on turbulent non-premixed swirling flames,” *Energy & fuels*, vol. 27, no. 10, pp. 6191–6197, 2013.

[41] A. Hayakawa, Y. Arakawa, R. Mimoto, K. D. K. A. Somarathne, T. Kudo, and H. Kobayashi, “Experimental investigation of stabilization and emission characteristics of ammonia/air premixed flames in a swirl combustor,” *Int J Hydrogen Energy*, vol. 42, no. 19, pp. 14010–14018, 2017.

[42] A. A. Khateeb, “Stability Limits and Exhaust Emissions from Ammonia Flames in a Swirl Combustor at Elevated Pressures,” 2020.

[43] T. Boushaki, N. Merlo, S. De Persis, C. Chauveau, and I. Gökalp, “Experimental investigation of CH4-air-O2 turbulent swirling flames by Stereo-PIV,” *Exp Therm Fluid Sci*, vol. 106, pp. 87–99, 2019.

[44] W. Jerzak and M. Kuźnia, “Experimental study of impact of swirl number as well as oxygen and carbon dioxide content in natural gas combustion air on flame flashback and blow-off,” *J Nat Gas Sci Eng*, vol. 29, pp. 46–54, 2016.

[45] H. Zaidaoui, T. Boushaki, J.-C. Sautet, and C. Chauveau, “Effects of exhaust gas on CH 4-air-O 2 turbulent swirling flames,” in *37th international symposium on combustion*, 2018.

[46] A. Vandel, J. P. C. Cano, S. de Persis, and G. Cabot, “Study of the influence of water vapour and carbon dioxide dilution on flame structure of swirled methane/oxygen-enriched air flames,” *Exp Therm Fluid Sci*, vol. 113, p. 110010, 2020.

[47] Z. Mansouri, M. Aouissi, and T. Boushaki, “Numerical computations of premixed propane flame in a swirl-stabilized burner: Effects of hydrogen enrichment, swirl number and equivalence ratio on flame characteristics,” *Int J Hydrogen Energy*, vol. 41, no. 22, pp. 9664–9678, 2016.

[48] Y. Huang and V. Yang, “Effect of swirl on combustion dynamics in a lean-premixed swirl-stabilized combustor,” *Proceedings of the combustion institute*, vol. 30, no. 2, pp. 1775–1782, 2005.

[49] T. Boushaki, N. Merlo, C. Chauveau, and I. Gökalp, “Study of pollutant emissions and dynamics of non-premixed turbulent oxygen enriched flames from a swirl burner,” *Proceedings of the Combustion Institute*, vol. 36, no. 3, pp. 3959–3968, 2017.

[50] G. Kychakoff *et al.*, “Visualization of turbulent flame fronts with planar laser-induced fluorescence,” *Science (1979)*, vol. 224, no. 4647, pp. 382–384, 1984.

[51] R. K. Hanson, J. M. Seitzman, and P. H. Paul, “Planar laser-fluorescence imaging of combustion gases,” *Applied Physics B*, vol. 50, pp. 441–454, 1990.

[52] M. Shimura, T. Ueda, G.-M. Choi, M. Tanahashi, and T. Miyauchi, “Simultaneous dual-plane CH PLIF, single-plane OH PLIF and dual-plane stereoscopic PIV measurements in methane-air turbulent premixed flames,” *Proceedings of the Combustion Institute*, vol. 33, no. 1, pp. 775–782, 2011.

[53] C. Schulz *et al.*, “Laser-induced incandescence: recent trends and current questions,” *Applied Physics B*, vol. 83, pp. 333–354, 2006.

[54] N. Jiang, P. S. Hsu, S. Roy, P. M. Danehy, and Z. Zhang, “100-kHz rate Rayleigh Imaging for Combustion and Flow Diagnostics,” in *AIAA Scitech 2019 Forum*, 2019, p. 1323.

[55] J. P. Singh and S. N. Thakur, *Laser-induced breakdown spectroscopy*. Elsevier, 2020.

[56] M. Lackner, "Tunable diode laser absorption spectroscopy (TDLAS) in the process industries–a review," *Reviews in Chemical Engineering*, vol. 23, no. 2, pp. 65–147, 2007.

[57] R. J. Adrian and J. Westerweel, *Particle image velocimetry*, no. 30. Cambridge university press, 2011.

[58] C. P. Wang, "Laser doppler velocimetry," *J Quant Spectrosc Radiat Transf*, vol. 40, no. 3, pp. 309–319, 1988.

[59] V. Nori and J. Seitzman, "Evaluation of chemiluminescence as a combustion diagnostic under varying operating conditions," in *46th AIAA Aerospace Sciences Meeting and Exhibit*, 2008, p. 953.

[60] L. He, Q. Guo, Y. Gong, F. Wang, and G. Yu, "Investigation of OH* chemiluminescence and heat release in laminar methane–oxygen co-flow diffusion flames," *Combust Flame*, vol. 201, pp. 12–22, 2019.

[61] T. Kathrotia, U. Riedel, and J. Warnatz, "A numerical study on the relation of OH*, CH*, and C2* chemiluminescence and heat release in premixed methane flames," in *Proceedings of the European combustion Meeting*, 2009.

[62] Y. Liu, J. Tan, H. Wang, and L. Lv, "Characterization of heat release rate by OH* and CH* chemiluminescence," *Acta Astronaut*, vol. 154, pp. 44–51, 2019.

[63] X. Li and L. Ma, "Capabilities and limitations of 3D flame measurements based on computed tomography of chemiluminescence," *Combust Flame*, vol. 162, no. 3, pp. 642–651, 2015.

[64] N. Lamoureux, N. Djebali-Chaumeix, and C.-E. Paillard, “Laminar flame velocity determination for H2–air–He–CO2 mixtures using the spherical bomb method,” *Exp Therm Fluid Sci*, vol. 27, no. 4, pp. 385–393, 2003.

[65] V. Cleary, P. Bowen, and H. Witlox, “Flashing liquid jets and two-phase droplet dispersion: I. Experiments for derivation of droplet atomisation correlations,” *J Hazard Mater*, vol. 142, no. 3, pp. 786–796, 2007.

[66] N. Chakraborty and N. Swaminathan, “Influence of the Damköhler number on turbulence-scalar interaction in premixed flames. I. Physical insight,” *Physics of Fluids*, vol. 19, no. 4, 2007.

[67] G. Damköhler, “The effect of turbulence on the flame velocity in gas mixtures,” *Zeitschrift fuer Elektrochemie und Angewandte Physikalische Chemiw*, vol. 46, no. NACA-TM-1112, 1947.

[68] Y. Gao and W. K. Chow, “A Brief Review on Combustion Modeling,” *International Journal on Architectural Science*, vol. 6, no. 2, pp. 38–69, 2005.

[69] J. A. van Oijen, *Flamelet-generated manifolds: development and application to premixed laminar flames*. Eindhoven University Press, 2002.

[70] T. Li, F. Kong, B. Xu, and X. Wang, “Turbulent combustion modeling using a flamelet generated manifold approach—a validation study in OpenFOAM,” *Appl Math Mech*, vol. 40, no. 8, pp. 1197–1210, 2019.

[71] F. Proch and A. M. Kempf, “Modeling heat loss effects in the large eddy simulation of a model gas turbine combustor with premixed flamelet generated manifolds,” *Proceedings of the combustion institute*, vol. 35, no. 3, pp. 3337–3345, 2015.

[72] L. Langone *et al.*, “Assessment of Thickened Flame Model Coupled With Flamelet Generated Manifold on a Low-Swirl Partially Premixed Gaseous

Lifted Flame," in *Turbo Expo: Power for Land, Sea, and Air*, 2022, p. V03BT04A007.

[73] B. Cuenot, F. Shum-Kivan, and S. Blanchard, "The thickened flame approach for non-premixed combustion: Principles and implications for turbulent combustion modeling," *Combust Flame*, vol. 239, p. 111702, 2022.

[74] S. Guo, J. Wang, X. Wei, S. Yu, M. Zhang, and Z. Huang, "Numerical simulation of premixed combustion using the modified dynamic thickened flame model coupled with multi-step reaction mechanism," *Fuel*, vol. 233, pp. 346–353, 2018.

[75] J.-P. Legier, T. Poinsot, and D. Veynante, "Dynamically thickened flame LES model for premixed and non-premixed turbulent combustion," in *Proceedings of the summer program*, 2000, pp. 157–168.

[76] V. Zimont, W. Polifke, M. Bettelini, and W. Weisenstein, *An efficient computational model for premixed turbulent combustion at high Reynolds numbers based on a turbulent flame speed closure*, vol. 78699. American Society of Mechanical Engineers, 1997.

[77] F. Nicoud and F. Ducros, "Subgrid-scale stress modelling based on the square of the velocity gradient tensor," *Flow Turbul Combust*, vol. 62, no. 3, pp. 183–200, 1999.

[78] P. Siemens, "Simcenter STAR-CCM+ user guide V22.06," *Siemens PLM*, 2022.

[79] R. I. Issa, "Solution of the implicitly discretised fluid flow equations by operator-splitting," *J Comput Phys*, vol. 62, no. 1, pp. 40–65, 1986.

[80] T. B. Kıymaz, "LAMINAR FLAME PROPAGATION STUDIES IN A SPHERICAL COMBUSTION CHAMBER; EXPERIMENTAL AND NUMERICAL APPROACHES," Middle East Technical University, 2023.

[81] R. F. Muldiani, K. Hadiningrum, and D. Pratama, “Experiments for determining the thermal conductivity of brass and 304 stainless steel with direct temperature measurement techniques using lorenz number as validation,” in *2nd International Seminar of Science and Applied Technology (ISSAT 2021)*, 2021, pp. 123–129.

[82] M. Karalus, D. Brandt, A. Brown, and V. Lister, “A multi-timescale approach for the prediction of temperatures in a gas turbine combustor liner,” in *Turbo Expo: Power for Land, Sea, and Air*, 2020, p. V07AT11A004.

[83] S. B. Pope, *Turbulent flows*. Cambridge university press, 2000.

[84] L. Langone, M. Amerighi, and A. Andreini, “Large eddy simulations of a low-swirl gaseous partially premixed lifted flame in presence of wall heat losses,” *Energies (Basel)*, vol. 15, no. 3, p. 788, 2022.

APPENDICES

A. MATLAB Script Used for Averaging a Series of Images

```
%get folder path from the user
image_folder_path = uigetdir("", "Please select the folder containing the
images to be averaged");

%check path
if ~isfolder(image_folder_path)
  errorMessage = sprintf('Error: The following folder does not
exist:\n%s', image_folder_path);
  uiwait(warndlg(errorMessage));
  return;
end

%get the file extension of the images from the user
image_file_extension = inputdlg("Please enter image file extension ",
"s");

%get individual data for the images in the folder
image_file_pattern = fullfile(image_folder_path, strcat("*.",
image_file_extension));
image_files = dir(image_file_pattern);
number_of_images_in_folder = length(image_files);

%check if there exist any images within the specified folder with the
given extension
if number_of_images_in_folder == 0
    errorMessage = sprintf("Error: There are no folder with extension '"
+ image_file_extension + "' in specified path");
    uiwait(warndlg(errorMessage));
    return;
end

%get crop coordinates
first_image_address = fullfile(image_folder_path, image_files(1).name);
first_image = imread(first_image_address);
figure
imshow(double(first_image)./max(max(double(first_image))))
[~,crop_corner_coordinates]=imcrop;
close all

%crop the first image and get matrix size of image
first_image_cropped = imcrop(first_image, crop_corner_coordinates);
cropped_image_size = size(first_image_cropped);
cropped_2d_image_size = [cropped_image_size(1), cropped_image_size(2)];

%initialize and populate the image array
```

```
image_array = zeros(cropped_2d_image_size(1), cropped_2d_image_size(2),
number_of_images_in_folder);
for i = 1:number_of_images_in_folder
    base_image_name = image_files(i).name;
    image_address = fullfile(image_folder_path, base_image_name);
    image_matrix_3d = imread(image_address);
    image_matrix_3d_cropped = imcrop(image_matrix_3d,
crop_corner_coordinates);
    image_matrix_2d_cropped = image_matrix_3d_cropped(:,:,1);
    image_array(:,:,i) = image_matrix_2d_cropped;
end

%take the average of the 3d image array down to 2d average image
average_image_2d = mean(image_array, 3);
average_image_2d = floor(average_image_2d);

%display the average image as a contour
image(average_image_2d)
```

B. MATLAB Script Used for Superimposing Two Images

```
[fname_first_image,pname_first_image] = uigetfile({'*'},'Pick the first
picture',
'C:\Users\Asus\Desktop\Projects\Swirler\experimental\bulk_outputs\2nd_exp
eriment_sage_h2','MultiSelect','off');
first_image_file = fullfile(pname_first_image, fname_first_image);

[fname_second_image,pname_second_image] = uigetfile({'*'},'Pick the
second picture',
'C:\Users\Asus\Desktop\Projects\Swirler\experimental\bulk_outputs\2nd_exp
eriment_sage_h2','MultiSelect','off');
second_image_file = fullfile(pname_second_image, fname_second_image);

first_image = imread(first_image_file);
second_image = imread(second_image_file);

%crop first image
figure
imshow(double(first_image)./max(max(double(first_image))))
[~,crop_corner_coordinates_first_image]=imcrop;
close all
first_image_cropped = imcrop(first_image,
crop_corner_coordinates_first_image);

%crop second image
figure
imshow(double(second_image)./max(max(double(second_image))))
[~,crop_corner_coordinates_second_image]=imcrop;
close all
second_image_cropped = imcrop(second_image,
crop_corner_coordinates_second_image);

second_image = second_image_cropped;
first_image = first_image_cropped;

second_image =rgb2gray(second_image);

second_image = imresize(second_image, size(first_image));

super_impose_image = zeros(length(first_image(:,1)),
length(first_image(1,:)), 3);
super_impose_image(:,:,1) = first_image;
super_impose_image(:,:,2) = second_image;
super_impose_image = floor(super_impose_image);
super_impose_image = 255*(super_impose_image -
min(super_impose_image(:))) ./ (max(super_impose_image(:)) -
min(super_impose_image(:)));
super_impose_image = cast(super_impose_image, "uint8");

first_image_address_array = split(first_image_file, "\");
```

```
first_image_name =
first_image_address_array(length(first_image_address_array));
first_image_name = cell2mat(first_image_name);
second_image_address_array = split(second_image_file, "\");
second_image_name =
second_image_address_array(length(second_image_address_array));
second_image_name = cell2mat(second_image_name);

imshow(super_impose_image)
title(second_image_name + " superimposed on " + first_image_name);
```

C. MATLAB Script Used to Determine Flame Dimensions and Position from Superimposed Chemiluminescence Images

```
one_cm_pixel = 44;
contour_ratio = 0.4;
contour_tolerance = 0.008;
height_substract_pixel = 21;

[fname_first_image,pname_first_image] = uigetfile({'*'},'Pick the contour
picture',
'G:\Projects\Swirler\experimental\bulk_outputs\2nd_experiment_sage_h2\',
'MultiSelect','off');
first_image_file = fullfile(pname_first_image, fname_first_image);
first_image = imread(first_image_file);
first_image_max_int = max(max(first_image(:,:,1)));
first_image_min_int = min(min(first_image(:,:,1)));
contour_image = zeros(size(first_image(:,:,1)));
leftmost_contour_point = length(first_image(:,1));
rightmost_contour_point = 0;
lowermost_contour_point = 0;
uppermost_contour_point = length(first_image(1,:));



for i = 1:length(first_image(:,1,1))
    for k = 1:length(first_image(1,:,1))
        if first_image(i,k,1) < ((contour_ratio +
contour_tolerance)*(first_image_max_int - first_image_min_int)) &&
first_image(i,k,1) > ((contour_ratio -
contour_tolerance)*(first_image_max_int - first_image_min_int))
            contour_image(i,k) = 255;
            if i < uppermost_contour_point
                uppermost_contour_point = i;
            end
            if i > lowermost_contour_point
                lowermost_contour_point = i;
            end
            if k < leftmost_contour_point
                leftmost_contour_point = k;
            end
            if k > rightmost_contour_point
                rightmost_contour_point = k;
            end
        end
    end
end
```

```
super_impose_image = zeros(length(first_image(:,1,1)),
length(first_image(1,:,1)), 3);
super_impose_image(:,:,1) = first_image(:,:,1);
super_impose_image(:,:,2) = cast(contour_image, "uint8") +
first_image(:,:,2);

super_impose_image(lowermost_contour_point,:,3) = 255;
super_impose_image(uppermost_contour_point,:,3) = 255;
super_impose_image(:,rightmost_contour_point,3) = 255;
super_impose_image(:,leftmost_contour_point,3) = 255;
super_impose_image = floor(super_impose_image);
super_impose_image = 255*(super_impose_image -
min(super_impose_image(:))) ./ (max(super_impose_image(:)) -
min(super_impose_image(:)));
super_impose_image = cast(super_impose_image, "uint8");
imshow(super_impose_image)

flame_liftoff_height_cm = (length(first_image(:,1)) -
lowermost_contour_point - height_substract_pixel)/one_cm_pixel
flame_length_cm = (lowermost_contour_point -
uppermost_contour_point)/one_cm_pixel
flame_width_cm = (rightmost_contour_point -
leftmost_contour_point)/one_cm_pixel
```

D. Calculation Sheet Used in Calculating the Mass Flow Rates of Fuel and Air for the Numerical Simulations.

$\rho_{air\_1atm\_7degC} := 1.259 \frac{kg}{m^3}$

$\rho_{ch4\_1atm\_7degC} := 0.69 \frac{kg}{m^3}$

$\rho_{c2h6\_1atm\_7degC} := 1.3 \frac{kg}{m^3}$

$\rho_{c3h8\_1atm\_7degC} := 1.933 \frac{kg}{m^3}$

$\rho_{h2\_1atm\_7degC} := 0.0865 \frac{kg}{m^3}$

$fuel\_slpm := 21.851$

$h2\_ratio := 0.7$

$ng\_ratio := 1 - h2\_ratio = 0.3$

$air\_slpm := 259.136$

$ch4\_molf := 0.8875$ $\quad ch4\_mw := 16.04\ g$

$c2h6\_molf := 0.0965$ $\quad c2h6\_mw := 30.07\ g$

$c3h8\_molf := 0.016$ $\quad c3h8\_mw := 44.097\ g$

$fuel\_temp := 7\ °C$

$fuel\_pres := 1\ atm$

$air\_temp := 7\ °C$

$air\_pres := 1\ atm$

$ch4\_molf + c2h6\_molf + c3h8\_molf = 1$

$$ch4\_mf\_in\_ng := \frac{ch4\_molf \cdot ch4\_mw}{ch4\_molf \cdot ch4\_mw + c2h6\_molf \cdot c2h6\_mw + c3h8\_molf \cdot c3h8\_mw} = 0.7978285$$

$$c2h6\_mf\_in\_ng := \frac{c2h6\_molf \cdot c2h6\_mw}{ch4\_molf \cdot ch4\_mw + c2h6\_molf \cdot c2h6\_mw + c3h8\_molf \cdot c3h8\_mw} = 0.16262884$$

$$c3h8\_mf\_in\_ng := \frac{c3h8\_molf \cdot c3h8\_mw}{ch4\_molf \cdot ch4\_mw + c2h6\_molf \cdot c2h6\_mw + c3h8\_molf \cdot c3h8\_mw} = 0.03954266$$

$$\rho_{ng\_1atm\_7degC} := \frac{1}{\frac{ch4\_mf\_in\_ng}{\rho_{ch4\_1atm\_7degC}} + \frac{c2h6\_mf\_in\_ng}{\rho_{c2h6\_1atm\_7degC}} + \frac{c3h8\_mf\_in\_ng}{\rho_{c3h8\_1atm\_7degC}}} = 0.76815008 \frac{kg}{m^3}$$

$ng\_slpm := fuel\_slpm \cdot ng\_ratio = 6.5553$

$h2\_slpm := fuel\_slpm \cdot h2\_ratio = 15.2957$

$$ng\_qdot := ng\_slpm \cdot \frac{fuel\_temp}{273.15\ K} \cdot \frac{14.696\ psi}{fuel\_pres} \frac{L}{min} = 6.72331575 \frac{L}{min}$$

$$h2\_qdot := h2\_slpm \cdot \frac{fuel\_temp}{273.15\ K} \cdot \frac{14.696\ psi}{fuel\_pres} \frac{L}{min} = 15.68773674 \frac{L}{min}$$

$$air\_qdot := air\_slpm \cdot \frac{air\_temp}{273.15\ K} \cdot \frac{14.696\ psi}{air\_pres} \frac{L}{min} = 265.77779039 \frac{L}{min}$$

$$ng\_mdot := ng\_qdot \cdot \rho_{ng\_1atm\_7degC} = 8.60752594 \cdot 10^{-5} \frac{kg}{s}$$

$$h2\_mdot := h2\_qdot \cdot \rho_{h2\_1atm\_7degC} = 2.26164871 \cdot 10^{-5}\ \frac{kg}{s}$$

$$air\_mdot := air\_qdot \cdot \rho_{air\_1atm\_7degC} = 0.0055769\ \frac{kg}{s}$$

$$air\_mdot = 0.0055769\ \frac{kg}{s}$$

$$ng\_mdot = 8.60752594 \cdot 10^{-5}\ \frac{kg}{s}$$

$$h2\_mdot = 2.26164871 \cdot 10^{-5}\ \frac{kg}{s}$$

$$total\_fuel\_mdot := ng\_mdot + h2\_mdot = 0.00010869\ \frac{kg}{s}$$

$$ng\_mf := \frac{ng\_mdot}{total\_fuel\_mdot} = 0.79192084$$

$$h2\_mf := \frac{h2\_mdot}{total\_fuel\_mdot} = 0.20807916$$

$$ch4\_mf := ng\_mf \cdot \frac{ch4\_molf \cdot ch4\_mw}{ch4\_molf \cdot ch4\_mw + c2h6\_molf \cdot c2h6\_mw + c3h8\_molf \cdot c3h8\_mw} = 0.63181702$$

$$c2h6\_mf := ng\_mf \cdot \frac{c2h6\_molf \cdot c2h6\_mw}{ch4\_molf \cdot ch4\_mw + c2h6\_molf \cdot c2h6\_mw + c3h8\_molf \cdot c3h8\_mw} = 0.12878917$$

$$c3h8\_mf := ng\_mf \cdot \frac{c3h8\_molf \cdot c3h8\_mw}{ch4\_molf \cdot ch4\_mw + c2h6\_molf \cdot c2h6\_mw + c3h8\_molf \cdot c3h8\_mw} = 0.03131465$$